Chemical Science

ROYAL SOCIETY OF CHEMISTRY

EDGE ARTICLE



Cite this: *Chem. Sci.*, 2021, **12**, 8178

All publication charges for this article have been paid for by the Royal Society of Chemistry

Received 17th February 2021
Accepted 29th April 2021

DOI: 10.1039/d1sc00957e

rsc.li/chemical-science

# The Ras dimer structure†

Till Rudack, ‡*[ab] Christian Teuber,‡[ab] Marvin Scherlo,[ab] Jörn Güldenhaupt,[ab] Jonas Schartner,[b] Mathias Lübben,[ab] Johann Klare,[c] Klaus Gerwert *[ab] and Carsten Kötting *[ab]

Oncogenic mutated Ras is a key player in cancer, but despite intense and expensive approaches its catalytic center seems undruggable. The Ras dimer interface is a possible alternative drug target. Dimerization at the membrane affects cell growth signal transduction. *In vivo* studies indicate that preventing dimerization of oncogenic mutated Ras inhibits uncontrolled cell growth. Conventional computational drug-screening approaches require a precise atomic dimer model as input to successfully access drug candidates. However, the proposed dimer structural models are controversial. Here, we provide a clear-cut experimentally validated N-Ras dimer structural model. We incorporated unnatural amino acids into Ras to enable the binding of labels at multiple positions *via* click chemistry. This labeling allowed the determination of multiple distances of the membrane-bound Ras-dimer measured by fluorescence and electron paramagnetic resonance spectroscopy. In combination with protein–protein docking and biomolecular simulations, we identified key residues for dimerization. Site-directed mutations of these residues prevent dimer formation in our experiments, proving our dimer model to be correct. The presented dimer structure enables computational drug-screening studies exploiting the Ras dimer interface as an alternative drug target.

## Introduction

Ras is a small G protein that acts as a molecular switch in the context of cell differentiation, proliferation, and growth. Ras is active in the guanosine triphosphate (GTP) bound state and transduces signals downstream to the cell nucleus. Furthermore, it catalyzes the hydrolysis from GTP to guanosine diphosphate (GDP) leading to an inactive state. This switch-off process is further accelerated by GTPase-activating proteins (GAPs).[1] If the catalysis function of Ras is impaired by mutations, tumors can develop due its constitutively active state. The reaction mechanisms of the GTP hydrolysis have been well characterized using experimental techniques such as X-ray structure analysis,[2,3] nuclear magnetic resonance spectroscopy,[4] Fourier transform infrared (FTIR) spectroscopy,[5] and theoretical methods.[6] Both the allosteric regulation of Ras and its signaling[7–10] as well as insights into catalysis of small GTPases have been previously reviewed.[1,10–13]

Currently, there is no drug against constitutively active Ras approved and Ras is traditionally referred to as undruggable. Recently, with advancing methods and new targeting concepts, progress has been made in identifying the drug attacking points of Ras [14,15] and Ras targeting drug development.[16] This progress has led to the first drug; however its effects are restricted to the G12C mutation[17,18] that is *e.g.* found in lung cancer.[19] In this case a covalent attachment to the C12 allows the interference with the otherwise hard to target catalytic center.

Because targeting the catalytic center is so difficult, many efforts are being made to study Ras in a larger context, including its processing, interaction partners, distribution, and organization at the plasma membrane.[10] Ras dimerization and its impact on Raf-1 activation were described first in the year 2000.[20] In 2013 the first *in vitro* structural model of a Ras dimer at a membrane was proposed based on attenuated total reflectance infrared spectroscopy measurements in combination with distances estimated by Förster resonance energy transfer (FRET) using fluorescently labeled nucleotides and biomolecular simulations.[21] This study initiated several follow up studies that showed dimerization *in vivo*[22–24] opening up a new strategy for cell growth signaling inhibition by disrupting the proposed dimerization interface. The enhanced dimerization was shown to activate downstream signaling[23] while the inhibition of the dimer formation by a small protein[22] led to signal interference. *In vitro* and *in vivo* the presence of K-Ras dimers was demonstrated by GFP based FRET measurements.[25] The same study showed that a dimer preventing mutation of oncogenic K-Ras

[a]*Biospectroscopy, Center for Protein Diagnostics (PRODI), Ruhr University Bochum, 44801 Bochum, Germany. E-mail: Till.Rudack@ruhr-uni-bochum.de; Klaus.Gerwert@ruhr-uni-bochum.de; Carsten.Koetting@ruhr-uni-bochum.de*

[b]*Department of Biophysics, Ruhr University Bochum, 44801 Bochum, Germany*

[c]*Department of Physics, Osnabrück University, 49074 Osnabrück, Germany*

† Electronic supplementary information (ESI) available. See DOI: 10.1039/d1sc00957e

‡ These authors contributed equally to this work.

(K-Ras$^{G12D/D154Q}$) inhibits tumor growth in mice.[25] Using quantitative photoactivated localization microscopy it was shown that K-Ras-GDP and K-Ras-GTP form dimers at a physiological expression level.[23] Dynamic light scattering experiments showed the K-Ras4B dimer formation with the bound nucleotide analogue GTPγS.[26] Very recently it was shown by a plethora of methods including small angle X-ray scattering (SAXS) and biomolecular simulations that K-Ras4B forms dimers in the presence of Raf-RBD that are crucial for cell signaling.[27] Nevertheless, there have been conflicting reports about Ras dimerization.[10,28]

Kovrigina *et al.* analyzed the time-domain fluorescence anisotropy and NMR chemical shift perturbations of the Ras G-domain without a lipid anchor and they conclude that the Ras G-domain alone does not form dimers in solution.[29] In addition, Groves and colleagues showed *in vitro* that full-length and fully processed K-Ras4B remains monomeric in supported lipid bilayer membranes under variable conditions.[30] It was shown that photosensitized oxidation, due to experimental conditions such as high laser intensities, may lead to Ras dimerization.[31] Furthermore, a high protein concentration might lead to artificial dimerization as well.

However, the majority of studies support the presence of membrane bound Ras dimers. Immune electron microscopy studies show that about 40% of the Ras proteins form nanoclusters with a radius of approximately 9 nm at the membrane.[32,33] In one case even a trimeric organization of K-Ras has been observed,[34] while the rest of the observed organizations showed dimerization independent of the isoform.[21,26,35,36] The Ras clusters act as isoform specific signaling platforms that recruit and activate effectors.[37–39] For targeted development of anti-cancer drugs that break dimers of malfunctioning Ras and thereby inhibit signaling, a detailed understanding of the exact dimer interaction network is desirable.[40]

Promising drug targets can be proposed based on atomic level information regarding dimer interactions. However, the exact molecular structure of Ras-dimers remains elusive. Fig. 1 illustrates the diversity of the reported[21,26,35,36] various different contradictory dimer structural models. We categorize these models into three main categories based on their dimer interaction sides. The models in category I undergo helix α4 and α5 dimerization, and the ones in category II undergo helix α3 and α4 dimerization, while the ones in category III undergo β-sheet dimerization. These categories are further subdivided with respect to their detailed dimer interactions in Fig. S1.† Structure **I.1** was derived from the crystal contacts within most Ras X-ray structures,[21] **I.2** (either N-Ras-GDP[21] or K-Ras4B-GTP[35]) was obtained by biomolecular simulations, and **I.3** (K-Ras4B-GDP) and **I.4** (K-Ras4B-GTP) were both derived from NMR data.[36] Structure **II.1** (K-Ras4B-GTP) was obtained by biomolecular simulations,[35] while **II.2** (K-Ras4B-GppNHp) and **III.1** (K-Ras4B-GTP-γ-S)[26] were generated by the protein interactions by the structural matching (PRISM) algorithm.[41] Details about the models are given in ESI Note 1.†

While various aforementioned experimental data indicate Ras dimerization, only a few studies provide insights into the structure of such dimers at the molecular level with atomic resolution. Two studies obtained NMR shifts for K-Ras4B dimers, one without the membrane[26] and one using nanodiscs to mimic the membrane attachment.[36] However, the structural models reported, namely models **I.3**, **I.4**, **II.2**, and **III.1**, vary over all three categories. In a previous study we measured a FRET distance of 46 ± 6 Å between the labeled (Mant/TNP) nucleotides.[21] The aim of this study was to identify Ras dimerization and its orientation attachment to the membrane. However, the distance between labeled nucleotides measured with FRET is not sufficient to unambiguously determine the correct orientation of the monomers within a dimer. Overall, while there are various different dimer structural models reported none of them are clear-cut experimentally validated. Therefore, additional experimental data are required to allow an unambiguous validation of the proposed dimer structural models.

In order to obtain dimer structural models, we first used different established docking algorithms to predict dimer structural models with satisfactory statistical accuracy. Next, we employed FRET and electron paramagnetic resonance (EPR) spectroscopy to provide several experimental distances to enable an unambiguous validation for the predicted models. For these methods, fluorophores or spin labels need to be

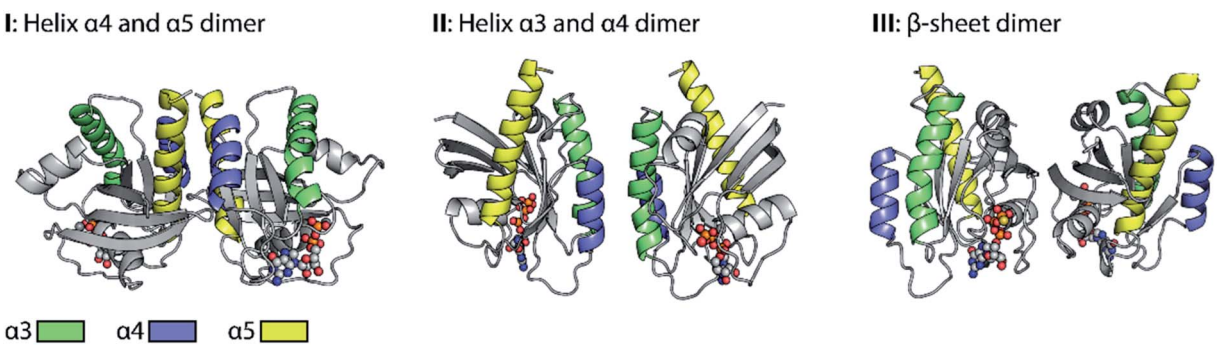


Fig. 1 Diversity of proposed Ras dimer structural models. To order the huge variety of the published dimer structural models we divided them into three substantially different main categories based on the relative orientation of the monomers. The key helices are represented by different colors (helix α3: green, helix α4: blue, helix α5: yellow) and the nucleotides are displayed in spherical shapes. The category I dimer interface is formed by contacts of helices α4 and α5, category II by helix α3 and α4 contacts, and category III by β-sheet contacts.

attached to various positions of the Ras surface to obtain sufficient distance variations for each structural model. To achieve membrane binding, a lipid anchor is attached to the Ras protein *via* maleimide chemistry at Cys181 limiting the chemical options to introduce labels. Therefore, to ensure flexible site specific labeling for the fluorophores and the EPR label we developed a strategy to incorporate unnatural amino acids into Ras. These amino acids were used as binding sites to which fluorophores or spin labels were attached *via* a second biorthogonal click reaction that does not cross-interfere with lipid coupling *via* the maleimide group. The identified dimer structural models that coincided with the available experimental FRET and EPR distances were further refined by biomolecular simulations to equilibrate the solvated membrane attached models. Based on these simulations we identified key dimer forming interaction residues. The effects of mutations of the computationally suggested interaction on dimerization were further checked experimentally by site-specific mutagenesis and FRET. A reliable characterization of the atomic details of Ras dimer interfaces is needed to guide the search for drug target sites for small molecules, which exert their anti-cancer effects by impairing Ras dimerization and constitutive signaling.

# Results

### Computational prediction of possible Ras dimer structural models

The literature shows that different workflows and docking algorithms provide numerous different Ras dimer models. We divide the seven published highly divers structural models into three main categories (I–III) based on their contact sides (Fig. 1). In order to obtain more potential dimer structures we used three different protein–protein docking web servers (PRISM,[41] ZDOCK[42] and Symmdock[43,44]). As input, we used six monomeric structural models of the Ras G-domain (residues 1 to 172) for H-Ras, K-Ras4B, and N-Ras with bound GTP and GDP. Table S1† summarizes the resulting 178 different dimer structural models reflecting nine different main interaction sides. While three of these interaction sides were already identified in the published models, six new possible interaction sides were detected by these algorithms (IV–IX). Details are given in ESI Note 2.†

### The experimental strategy to obtain different experimental distances

To reduce the number of possible dimer models and enable a clear-cut assignment of a unique structural dimer model, we developed a new strategy (Fig. 2) to obtain additional experimental distance information. The number of natural binding sites for labels to measure distances is limited and site specificity is difficult to achieve. Thus, the N-Ras lipid anchor containing a palmitoyl and a farnesyl group was attached to cysteine 181 of N-Ras *via* a maleimide group (see Fig. 2A and ESI Note 3†). The chemistry necessary to attach the anchor limits the chemical options to introduce labels for distance measurements. Individual labeling positions for FRET and EPR measurements were achieved by the incorporation of unnatural amino acids. The used strategy is described in Fig. S2,† and is based on previously reported protocols from Edward Lemke,[45] which describe the site specific incorporation of the unnatural amino acids *N*-propargyl-L-lysine (PrK) and the cyclooctyne-lysine (SCO) into N-Ras using the amber codon suppression strategy. The unnatural amino acids bind the fluorophores or spin labels without interfering with lipid anchor binding. We identified S106 and T124 as the best incorporation sites yielding sufficient amounts of protein with the incorporated unnatural amino acid (Fig. S2B†).

Next, the fluorophores and spin labels are bound to the unnatural amino acids *via* the copper(I) catalyzed alkyne–azide cycloaddition (CuAAC) as shown in Fig. 2B and ESI Note 3† or *via* the strain promoted alkyne–azide cycloaddition (SPAAC). One fraction of PrK labelled Ras was bound to Atto 532 azide (FRET donor) and another fraction was bound to Atto 655 azide (FRET acceptor). Similarly, the EPR spin label azido-proxyl was coupled to T124 of N-Ras *via* the unnatural amino acid SCO. Fig. 2C shows an exemplarily Ras dimer structural model with attached lipid anchor and the fluorophores Atto 655 and Atto 532 at position T124. Chemical drawings of the FRET labels are provided in Fig. S3.†

Then, we experimentally determined the FRET distances summarized in Fig. 2D. These distances are based on FRET efficiencies, which were derived from the fluorophore lifetimes measured with a time-correlated single photon counting (TCSPC) setup. The respective TCSPC histograms of all measured FRET distances and the experimental EPR data are presented in Fig. S4.† For these FRET measurements, we mixed the Ras protein to be investigated with 1-palmitoyl-2-oleoyl-*sn*-phosphatidylcholine (POPC) liposomes. The lifetime ($\tau$) for membrane-bound N-Ras (GDP) S106-Atto 532 was analyzed in the presence ($\tau$DA) and absence ($\tau$D) of the acceptor N-Ras (GDP) S106-Atto 655 (Fig. S4A†). The analog experiment was performed for membrane-bound N-Ras (GDP) T124-Atto 532 and the acceptor N-Ras (GDP) T124-Atto 655 (Fig. S4B†). Both resulting histograms show a reduced $\tau$DA compared to $\tau$D due to FRET. The $\tau$ reduction is significantly stronger in samples with N-Ras (GDP) S106-Atto 532 (from 1.87 ns to 1.28 ns) than in samples with N-Ras (GDP) T124-Atto 532 (from 2.66 ns to 2.53 ns). Due to the large distance between the fluorophores at the T124 position, we verified the T124–T124 distance independently with an EPR spectroscopic double electron–electron resonance (DEER) measurement method that is more accurate in this distance regime (Fig. S4C†). This experiment resulted in a time-dependent echo amplitude that has been described by a Gaussian fit in order to obtain the distance information. The distance between the nucleotides was previously determined by FRET (18) (Fig. S4D†). The experimental details of the distance determination process are summarized in the Methods section, ESI Note 4, and in Table S2.†

The obtained distances between two membrane-bound lipidated N-Ras monomers (Fig. 2D) are 43.3 $\pm$ 2.3 Å between the FRET fluorophores coupled to S106–S106, 72 $\pm$ 3.5 Å between the fluorophores coupled to T124–T124, 59.7 $\pm$ 2.5 Å between

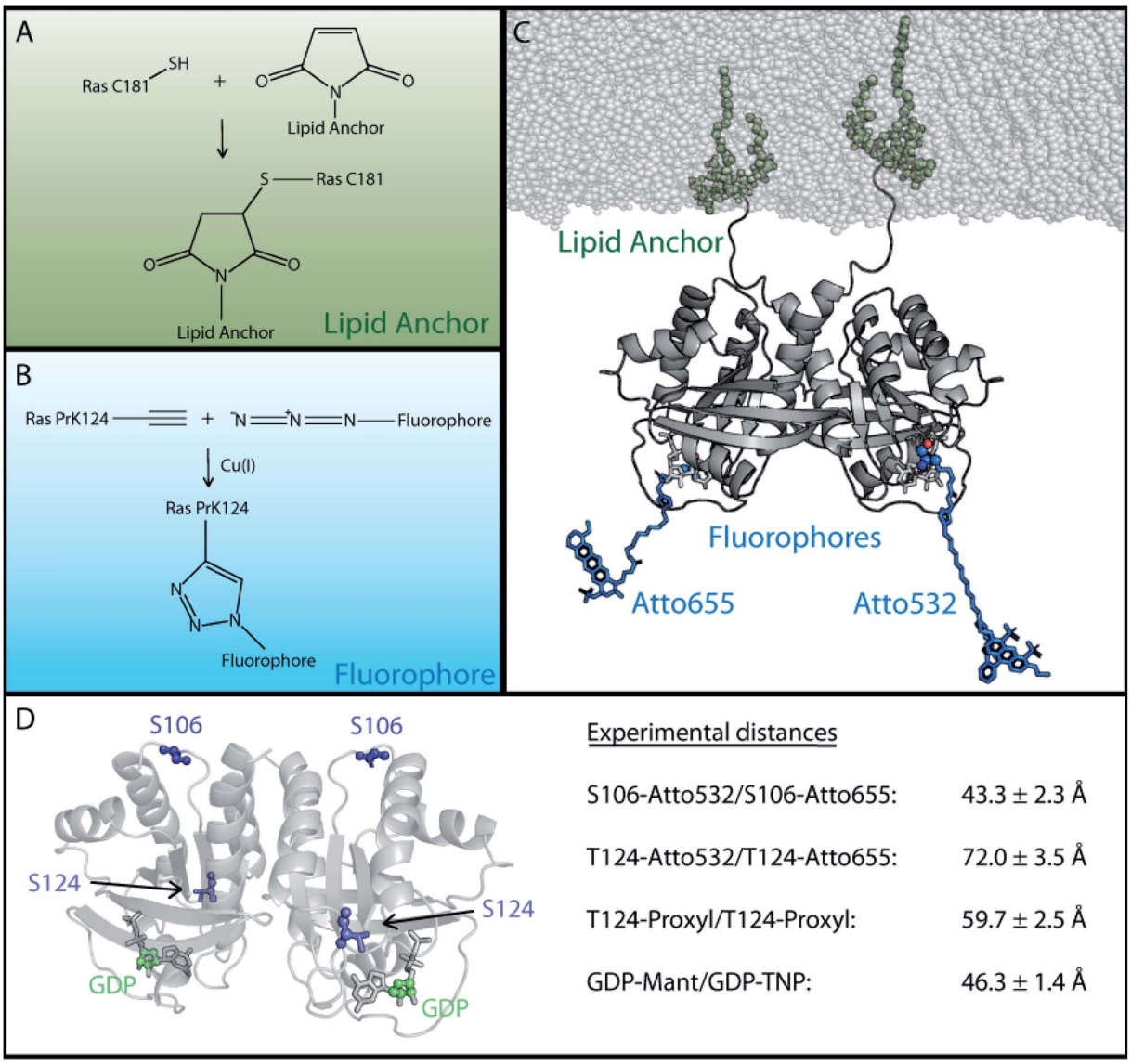


Fig. 2 Experimental strategy for the attachment of lipid anchor and fluorophores to enable FRET or EPR measurements of membrane bound Ras proteins. In order to perform FRET or EPR measurements on membrane-bound Ras, two site specific protein modifications were necessary; one to attach the lipid anchor to the protein and another for the fluorophore or spin label. (A) The lipid anchor is attached *via* a maleimide group to ensure membrane binding. (B) The fluorophore is coupled site specifically *via* copper(I) catalyzed alkyne–azide cycloaddition to the previously incorporated unnatural amino acid (Fig. S2†). (C) A Ras dimer structural model with attached lipid anchors and the fluorophore pair T124-Atto 655/T124-Atto 532. (D) An overview of the labeling sites and the experimentally obtained FRET and EPR distances between two membrane bound full-length N-Ras-GDP proteins. The previously reported GDP distance was used.[21]

the EPR proxyl labels at T124–T124, and 46.3 ± 1.4 Å between the fluorescent labeled nucleotides.[21] The distance between the EPR labels at T124 is shorter than the one between the FRET labels at the same position, as the EPR label is shorter than the FRET label (Fig. S5†). The corresponding Cα distance is the same for both methods. The three different labeling positions are well distributed over the Ras surface as shown in Fig. 2D, which ensures a significantly more precise validation of possible Ras dimer structural models than the previously available single distance of the labeled nucleotides.

The obtained distances for two N-Ras monomers including the lipid anchor solely in solution without membrane are 49.7 ± 0.8 Å between the FRET fluorophores coupled to S106–S106 and 77 ± 0.5 Å between the ones coupled to T124–T124. All distances are summarized in Table S2.†

### Comparison of experimental distances with calculated distances of the predicted dimer models

We utilized the four experimental distances for membrane-bound N-Ras-GDP to evaluate the 178 dimer conformations resulting from our protein–protein docking (Table S1†). The nine main conformations of the monomer orientation are further divided into 64 subcategories, representing slight variations in the dimer binding interface. Next, we calculated the

respective distance distributions for each of the 64 conformations within the subcategories and compared them with the experimentally obtained values. Details regarding the generation of rotamer ensembles and calculation of the respective distance distributions for all experimentally used labels and positions are shown in Fig. S5 and ESI Note 5.† We used the PyMOL plugin MTSSL Wizard to calculate the rotamer ensembles. The distributions are fitted by a Gaussian function to obtain a mean value and standard deviation for each labeling position of each dimer conformation (Table S3†). As a further control of the label ensembles created by the MTSSL Wizard, we performed biomolecular simulations to analyze the conformational space sampled by SCO-proxyl at T124 (Fig. S6†).

Fig. 3A–D represents the distance calculation for the seven published dimer models shown in Fig. S1.† Possible membrane interactions that potentially further restrict the conformational space of labels are excluded in the calculation. Also, protein label and label–label interactions are described by a simplified model. Employing more accurate models describing the label interactions will lead to a further restriction of the conformational space. Therefore, the bandwidths of the calculated curves reflect the outer limit of label flexibility for one single dimer. In contrast, the experimental bandwidth is the standard deviation of the average value of the protein ensembles (~60 million photons per measurement) of eight measurements for two different samples. Therefore, the experimental bandwidth is substantially narrower than the calculated one. However, only for dimer models **I.1** and **I.2** the calculated distance distributions overlap with all four experimental distances. Model **I.3** does not match the T124–T124 measurements, while model **I.4** does not match the ones for T124–T124 and nucleotide–nucleotide. Model **II.1** is in accordance with the nucleotide distance measurements and significantly out of the experimental region for the other three distances, while model **II.2** is only in accordance with the S106–S106 distance. Model **III.1** diverges significantly from the nucleotide–nucleotide distance. Besides models **I.1** and **I.2** only **I.5** to **I.9** are in accordance with all four values as revealed by the comparison of the 64 dimer conformations obtained through protein docking in Table S3,† while models **I.10** to **I.13** present only one value which deviates slightly from the four measurements. The rest of the obtained conformations displayed significantly different values compared to the experimental distances. Consistently, the category II and III models obtained for K-Ras4B do not match the distances for K-Ras4B-GTP (Table S4†) or K-Ras4B-GDP (Table S5†) that were derived from published NMR shifts.

Based on their agreement with the experimental data, we probed the stability and further refined the detailed dimer

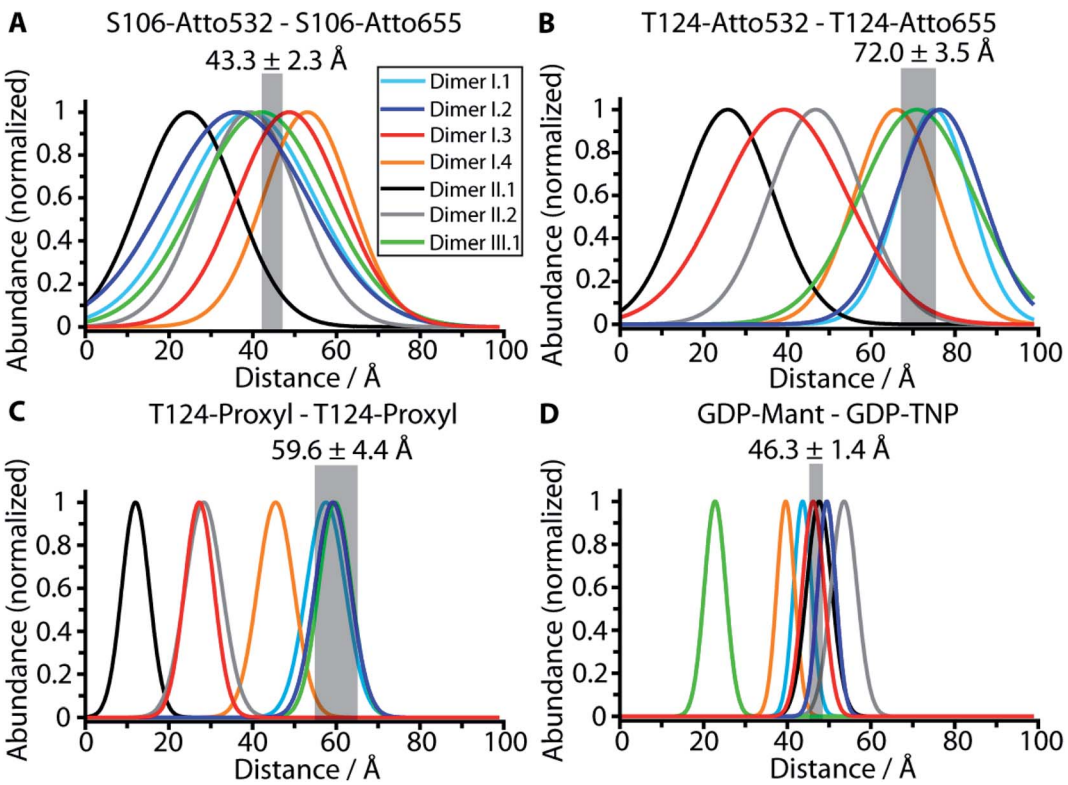


Fig. 3 Comparison of the experimental distances with the calculated distances for predicted dimer structural models. The experimental values obtained by FRET and EPR measurements (Fig. S4†) are shown as transparent grey bars. Only dimer structural models **I.1** and **I.2** are in line with all four measured distances as revealed by the comparison of the measured distances S106–S106 (A), T124–T124 (B), T124–T124 (EPR) (C) and nucleotide–nucleotide (D) (grey bars) with the calculated distance distributions based on the dimer structural models **I.1** (light blue), **I.2** (dark blue), **I.3** (cyan), **II.1** (black), **II.2** (grey) and **III.1** (green) as detailed in ESI Note 5.† The width of the calculated distribution reflects the steric maximal possible conformational space of the labels that provide the outer limit. If the experimental value is not within the calculated distribution in one of the four plots the structure is ruled out.

model interaction interface of the conformations of category I through MD simulations, with the exception of **I.2**, that was already obtained by refinement through MD simulations,[21] as well as **I.3** and **I.4** that were exclusively obtained for K-Ras4B whereas our experiments use N-Ras.

### MD simulations used to obtain one equilibrated representative dimer model

In total nine MD simulations of N-Ras-GDP initiated by the dimer models of conformation **I.1** and **I.5** to **I.12** were prepared, and were run for at least 550 ns. Simulations were setup, performed and analyzed as described in ESI Note 6.† Contact patterns were identified using the PyContact[46] and the Maximoby contact matrix algorithm. Simulation times and system properties are summarized in Table S6.† Equilibration of the systems was checked based on the root mean square displacement (RMSD) from the respective starting structure of each conformation and the time evolution of the contact pattern (Fig. S7†). The distances between the ensembles of labels attached to equilibrated representative structures were calculated and compared to the experimental values (Table S7†) analogous to the procedure for the predicted docking structures. Simulations **I.9** and **I.10** converge to an almost identical representative equilibrium dimer structural model (Fig. 4), that is in total accordance with the four experimental distances mentioned above. All seven other simulations converge to equilibrium structures with almost identical monomer orientation among each other but slightly different compared to the equilibrium structures observed for **I.9** and **I.10** (Fig. S8†). The monomers are slightly tilted against each other, leading to divergence from the experimental nucleotide–nucleotide distance. The structural models of the representative structures of simulations **I.9** and **I.10** are provided within the ESI.†

The time course analysis of the dimer interface interaction pattern of simulation trajectories **I.9** and **I.10** identified a stable central salt bridge between D154 and R161. This contact was the key dimer stabilizing salt bridge in five out of the seven simulations leading to the second equilibrium structure. The contact between E49 and H131 is the second most prevalent contact involved in the dimer interface formation either through a hydrogen bond or van-der-Waals interactions. However, this contact is fluctuating over time due to its exposed position at the edge of the dimer contact interface resulting in competing solvent interactions. Therefore, this contact is less stable than the D154/R161 contact, which is deeply buried in the center of the dimer interface (Fig. S8†). The distance plots (Fig. S9†) between D154 and R161 as well as E49 and H131 within simulation **I.9** further illustrates the fluctuating character of the E49/H131 interaction compared to the permanent D154/R161 contact. A detailed list of the relevant intra-protein contacts observed in the simulation trajectories is provided in Table S8.† Often protein bound water molecules or ions have a crucial structural or functional role.[47] However, our contact analyses shown in Fig. S13† indicate that there are no bridging water molecules or ions involved in the formation of the dimer interface.

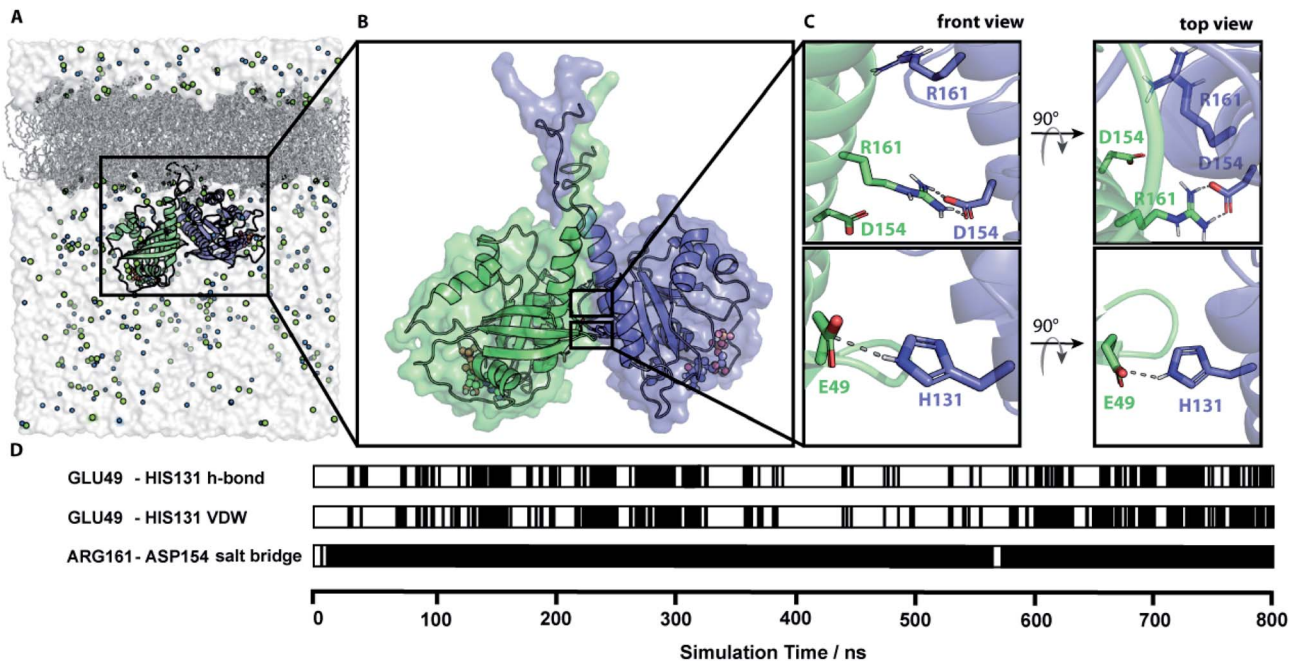


Fig. 4 Simulation of a membrane-bound N-Ras dimer. (A) The simulation system of a lipidated N-Ras dimer structural model attached to a POPC membrane inside a solvation box with a physiological salt (NaCl) concentration. (B) Representative protein structure of an 800 ns long MD simulation started with conformation **I.10** (representative structure in accordance with all four experimentally measured distances). (C) Key residues of the protein–protein interaction network identified by contact analysis of the simulation trajectory. (D) The time course of the key contacts within the simulation of conformation **I.10**. All contacts and the root mean square displacement (RMSD) are shown in Fig. S7.†

### Validation of the predicted dimer interface by FRET measurements of the E49Q D154N N-Ras variant

The MD simulations revealed that the most prominent dimer contact is the salt bridge between D154 and R161 and the second most prominent interaction is between E49 and H131. Based on our predicted contacts, we expected the E49Q and D154N mutations in Ras to prevent dimerization (Fig. 5A). To validate our predicted contact interface, we performed FRET measurements of the lipidated membrane-bound N-Ras E49Q D154N variant. As the FRET signal with fluorophores at residue 106 was the most prominent in wild type, we chose this label position for our variant. No FRET signal was observed (Fig. 5B) for the N-Ras E49Q D154N variant, indicating that the E49Q D154N is the variant that prevents dimer formation. This dimer preventing variant provides a clear-cut experimental proof for our suggested dimer model.

## Discussion

The organization of Ras at the plasma membrane is decisive for its function. There is experimental evidence that Ras dimerization is crucial for nanoclustering at the plasma membrane and signal transmission.[39] Our experiments with lipidated N-Ras WT attached to a POPC membrane (Fig. 2) provided further evidence for dimerization due to the evoked FRET-efficiencies or DEER signals (Table S2 and Fig. S4†). Our *in vitro* experimental setup using a POPC membrane does not perfectly match the *in vivo* conditions; however we are convinced that our found dimer interface is transferable to *in vivo* conditions. Dimerization of membrane-bound Ras was also shown for other completely different artificial membrane systems such as nanodiscs by NMR.[36] Even more importantly, an *in vivo* study showed that an impaired dimerization of oncogenic K-Ras abolishes tumor growth.[25] Dimerization at a membrane is indicated by the majority of experimental studies as previously described. The two most relevant studies for this matter indicate that K-Ras-GDP and K-Ras-GTP form dimers at a physiological expression level as revealed by quantitative photoactivated localization microscopy.[22,23] These studies observed a connection between the Ras dimerization and the activation of the Raf–MAPK signal pathway. Furthermore, attenuated total reflectance (ATR) infrared spectroscopy measurements in combination with biomolecular simulations have shown that N-Ras dimerizes on POPC membranes.[21] Some studies provide conflicting results that exclude dimerization, most of which were performed without a membrane in their experimental setup.[29] The only biophysical study indicating monomeric Ras, while including a membrane, measured the diffusion of Ras in a solid supported bilayer *in vitro*.[30] The authors of the study stated that Ras dimerization *in vivo* must

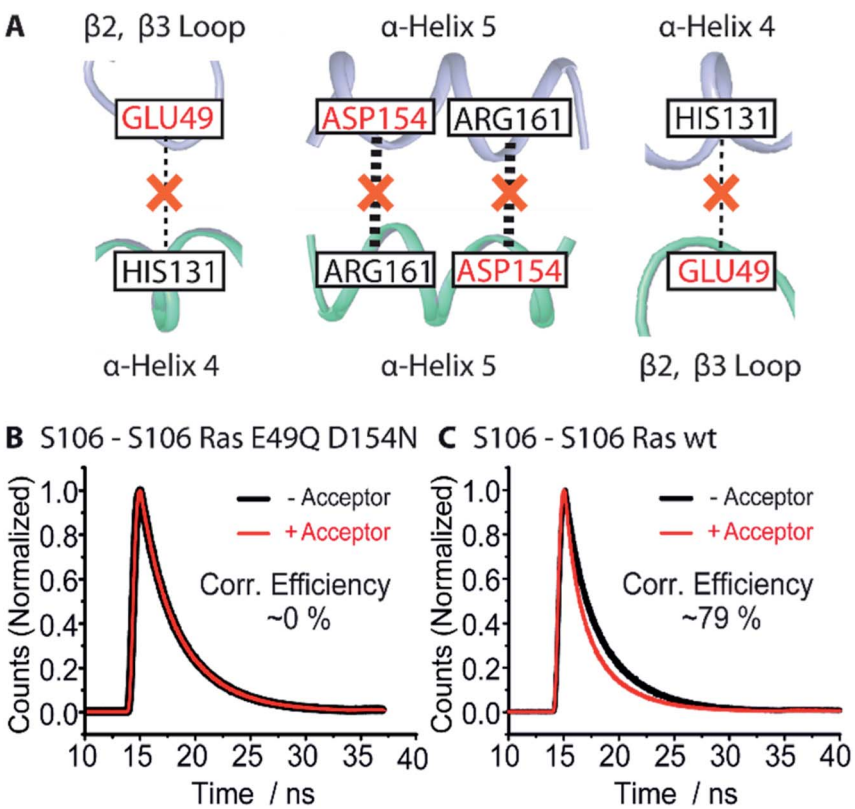


Fig. 5 Dimerization preventing the E49Q D154N N-Ras variant. (A) Schematic summary of the key dimer interactions (Table S6†) obtained from MD simulations (Table S7†) suggesting E49 and D154 as promising candidates for dimer preventing mutations. (B) FRET measurements of the lipidated membrane-bound N-Ras E49Q D154N variant confirm that mutations of E49 and D154 prevent the dimer formation as no observable FRET signals were detected compared to N-Ras WT (C). The computationally predicted N-Ras dimer interface is experimentally validated.

depend on more factors than the presence of the protein alone. Furthermore, they noted that the glass support of the bilayer may damp large membrane undulations influencing the lateral organization of Ras leading to contradicting results compared to the aforementioned *in vivo* studies.

There have been valid concerns that dimerization shown by FRET measurements is associated with high laser intensities[30] or high protein concentrations. However, our measurements show that neither of these are the case for the used experimental setup. While high laser intensities are exerted by confocal microscopes, we used time correlated single photon counting (TCSPC) with low laser intensity or EPR which does not involve a laser. The concern regarding the protein concentration was eliminated since we obtained dimerization for one measurement (N-Ras WT S106–S106) and no dimerization for another (E49Q D154N N-Ras variant S106–S106) while using the same protein concentration and identical experimental setups. Thus, there is strong evidence that lipidated membrane-bound full-length Ras forms dimers.

The lack of a detectable FRET signal for the E49Q D154N N-Ras variant indicates that this interaction site is the only one present, as at least a somewhat visible FRET signal would then be expected. This implies that full-length N-Ras does not form oligomers at POPC membranes, as an additional interaction site, different from the dimer interaction site identified here, would be necessary to form oligomers in wt N-Ras.

Our results indicate a decisive role of the lipid anchor in dimerization with and without membrane. We obtained comparable FRET efficiencies of full-length lipidated N-Ras solely in solution (S106–S106: 60% and T124–T124: 10%) and membrane bound (S106–S106: 79% and T124–T124: 15%). However, the same FRET measurements in solution using N-Ras 1–181 without the lipid anchor showed no signal, indicating that the Ras G domain lacks the intrinsic propensity to form dimers in solution. The N-Ras anchor is very hydrophobic (Fig. S10†), indicating that the hydrophobic effects are driving forces for anchor dimerization. These findings are in line with previous studies on the self-association of the G domain in solution observed *via* analysis of the time-domain fluorescence anisotropy and NMR chemical shift perturbations.[34] Overall, our data clearly indicate that the N-Ras lipid anchor is essential for the dimer formation in solution. We hypothesize that clustering of the lipid anchor is the first step towards dimerization. Clustering of the lipid anchor brings the G domains closer together and thus increases the local concentration of Ras proteins, which leads to the formation of one single otherwise comparably low affinity G domain interface. The lipid anchor substantially differs between the Ras isoforms leading to isoform specific lipid interactions.[48,49] Thus isoform dependent clustering at specific membrane compartments depending on the membrane lipid composition is observed.

Gasper and Wittinghofer suggested as an argument against dimerization that different Ras crystals show different crystal packings.[3] The C-terminal hypervariable region (HVR) including the lipid anchor is truncated in crystal structures due to their high flexibility. The remaining G domain has the potential to sample and form a huge variety of different dimer interfaces, due to the high protein concentrations during crystallization. This variety of dimer structural models is in line with the high variety of dimer conformations found by protein–protein docking algorithms (Table S1†). Both crystallography and docking studies miss the native conformational space restrictions as clustering of the lipid anchor and the space occupied by the membrane itself allows only limited possible G-domain dimer conformations for full length Ras. Therefore, crystal structures and protein–protein docking results lack the capacity to provide a single prominent structure, which we observe here for full length N-Ras. We note that our proposed dimer model is also a prominent motive within the crystal packing of Ras crystal structures. Thus, the lipid anchor steers the protein into an exclusive dimer structure at the membrane.

Knowledge of the precise amino acid interaction network of the dimer interface provides novel target sites for anti-cancer drugs that prevent Ras dimerization, which plays a crucial role in signal transduction *in vivo*.[40] Our study shows that for N-Ras only those dimer models exhibiting an interface involving helices α4 and α5 (dimer category I) are in accordance with all four experimental distances. Dimer category II disagrees with both FRET and EPR distances obtained for position T124 and category III disagrees with the experimentally observed nucleotide–nucleotide distance. In addition, Fig. 6 shows that the binding sites for the three Ras interaction partners Raf, RasGAP and SOS are all accessible for dimer category I structural models. NMR distances obtained for K-Ras also show that helices α4 and α5 are involved in dimerization.[36] The isoform independent motive of helices α4 and α5 dimerization interface is supported by a study showing the impact of disrupting this interface with a small synthetic protein affecting the signaling of both H-Ras and K-Ras.[22] The importance of dimerization for *in vivo* signaling is emphasized by the study showing that the disruption of the oncogenic K-RasG12D dimer abolishes *in vivo* tumor growth.[25] Taking together our results and the previously mentioned reports, we propose that the formation of the dimer interface by helices α4 and α5 is a universally valid motive for all Ras isoforms.

Biomolecular simulations revealed one representative equilibrated lipidated membrane-bound full-length N-Ras-GDP dimer model (Fig. 6) that is in accordance with all experimental distances (Table S7†). The identified key residues (Fig. 4) forming the salt bridge D154/R161 are conserved among all Ras isoforms. This salt bridge was also identified as a key contact in our previously published simulations on N-Ras.[21] The second most prominent contact residue E49 is also conserved and its interaction partner H131 is exchanged to Q131 in H- and K-Ras, still retaining the ability to form a hydrogen bond with E49. All these contact residues are positioned within a flat area of the Ras surface (Fig. S8†), which supports the proposed dimer interface. For N-Ras we confirmed the importance of D154 and E49 for dimerization as E49Q D154N mutations prevented dimerization (Fig. 5). Some but not all of the observed K-Ras4B NMR shifts[36] are in agreement with our N-Ras models refined through biomolecular simulations (Tables S4 and S5†). These deviations indicate a difference between N-Ras and K-Ras4B. Furthermore, models **I.3** and **I.4** for K-Ras4B do not exhibit the

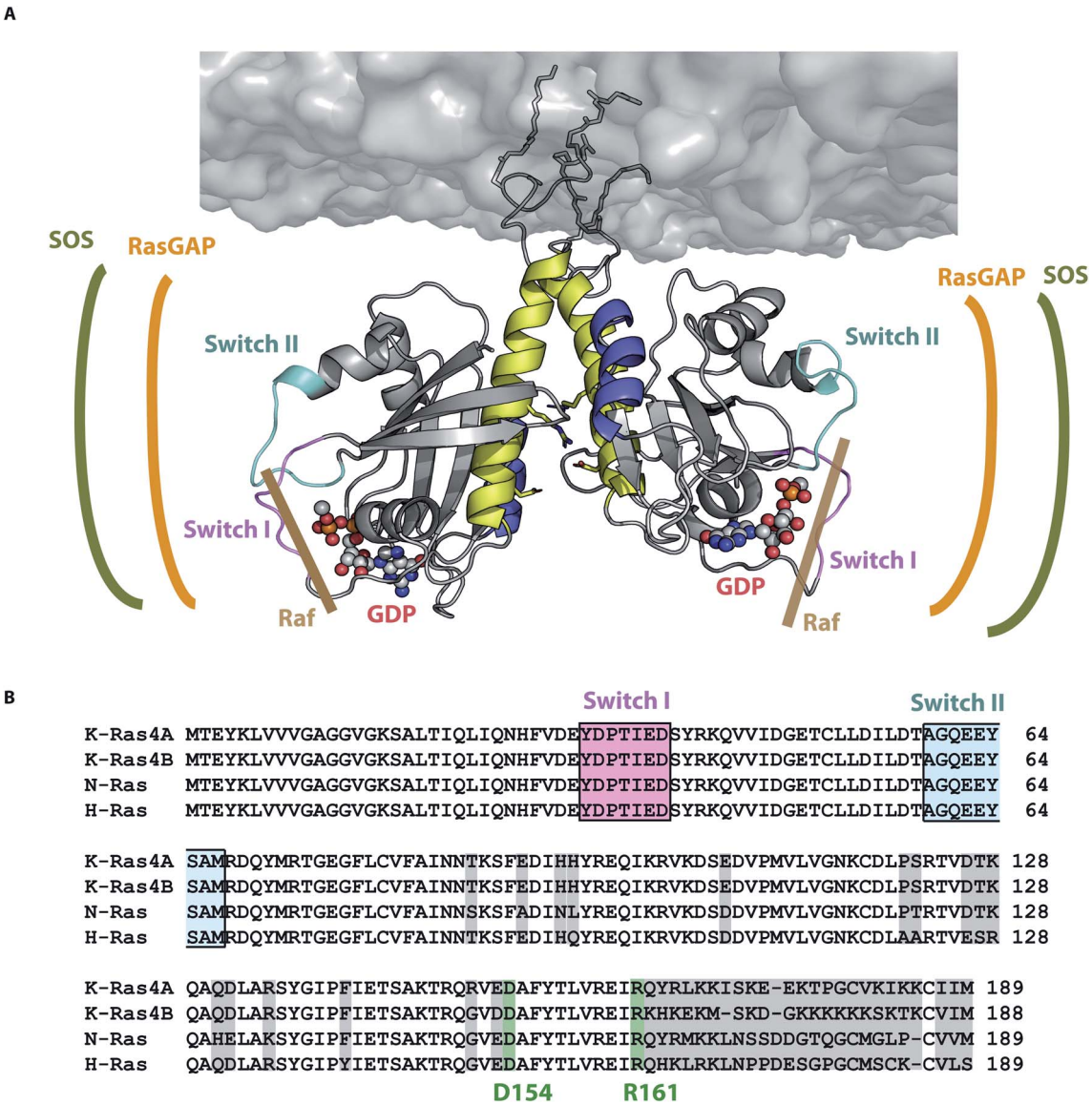


Fig. 6 N-Ras dimer structural model and its interaction sites. (A) N-Ras dimer structural model in accordance with all four experimentally observed distances. The dimer interface is formed by helices α4 (blue) and α5 (yellow). The binding sites of SOS (green), Ras-GAP (orange) and Raf (brown) are accessible for the respective Ras interaction partners. The nucleotide binding site and the switch I (pink) and II (cyan) are not involved in the dimer interface as they are on the opposite sides of the dimer interface. (B) Alignment of all Ras isoforms with non-conserved amino acids highlighted in light gray. The key contact residues D154/R161 (green) stabilizing the Ras dimer (Fig. 4 and 5) are conserved among all Ras isoforms.

D154/R161 key contact. Packer *et al.*[27] showed the importance of the D154/R161 interaction within the formation of the K-Ras4B–Raf-RBD dimer. Further experimental proof regarding the presence of the D154/R161 interaction in K-Ras4B was provided by Ambrogio *et al.*[25] They show the importance of the D154/R161 contact in K-Ras4B. Each of the two single mutants D154Q and R161E of oncogenic K-Ras4BG12D abolished *in vivo* tumor growth, implying that this is due to the impaired ability to form dimers. Thus, mutations in the dimer interface have the potential to eliminate the effect of oncogenic mutants at positions G12, G13, or Q61. The contact swapping mutant D154Q R161E showed tumor growth, though not as high as the wild type, possibly due to a weaker contact between Gln and Glu as opposed to the contact between Glu and Arg, though still allowing dimer formation. There might be slight difference in the detailed dimer interaction pattern between the Ras isoforms that still need further investigation. As shown by Spencer-Smith and colleagues, charge reversal mutation of D154 or R161 and R135 exhibited no effect on oncogenic H-RasG12V signaling, indicating the stabilization of its dimer interface through other residues for this isoform.[22] We anticipate that N-Ras and K-Ras both dimerize through helices α4 and α5 with D154/R161 as the key contact; however, further research is required to unravel the detailed H-Ras dimer interaction pattern.

In summary, we developed a novel strategy to incorporate unnatural amino acids into Ras, allowing two orthogonal site-specific modifications of the same protein (Fig. 2); one to attach a lipid anchor and a second one for fluorophores or spin labels

for distance measurements. Exploiting the gained flexibility of individual site-specific labeling we obtained three novel experimental distance information about N-Ras dimers. The S106–S106 distance of 43.3 ± 2.3 Å and T124–T124 distance of 72.0 ± 3.5 Å were obtained through FRET measurements and another T124–T124 distance of 59.6 ± 4.4 Å was obtained by EPR spectroscopy. All measurements indicate conclusively that lipidated full length N-Ras dimerizes at POPC membranes. We show that among 178 structural dimer models predicted by different protein–protein docking algorithms only those including helices α4 and α5 in the dimer interface are in accordance with the here obtained FRET and EPR data as well as previous FRET distances.[21] Further refinement of the dimer interface through biomolecular simulations revealed that the salt bridge between D154/R161 together with the interactions of E49 with H131 are the key N-Ras dimerization contacts (Fig. 4). Our computationally predicted interface was experimentally validated as FRET measurements showed that the N-Ras E49Q D154N variant prevented dimerization (Fig. 5).

Taking together our results for N-Ras, the sequence similarities between the isoforms, and the described literature for H-Ras and K-Ras we propose that all Ras isoforms dimerize at the membrane through helices α4 and α5 (Fig. 6). Nevertheless, there might be isoform specific differences in the exact orientation of the monomers. These atomic resolution structural insights into the Ras dimer interface provide novel target sites to develop anti-cancer drugs inhibiting Ras signaling by preventing its dimerization.

## Materials and methods

### Experimental methods

Biochemical details of lipid anchor synthesis, sample preparation of lipidated N-Ras with incorporated unnatural amino acids, coupling of fluorophores, and sample composition for FRET and EPR measurements are described in ESI Note 3.† We have chosen hydrophilic dyes that have a very low membrane interaction factor[50] to avoid artificial interactions.

The TCSPC histograms were evaluated, and the FRET efficiencies were calculated as described in ESI Note 4.† The results are also displayed in Table S2.† In the presence of the fluorescence acceptor, the amplitude weighted and averaged fluorophore's lifetimes decreased from 1.87 ns to 1.28 ns in measurements with membrane-bound N-Ras (GDP) S106-Atto 532 and from 2.66 ns to 2.53 ns in measurements with membrane-bound N-Ras (GDP) T124-Atto 532. As detailed in ESI Note 4,† we have to consider that dimers are randomly formed between donor labeled Ras (D), acceptor labeled Ras (A) and unlabeled Ras. Presuming a dimer and considering the fraction of DA dimers these values lead to FRET efficiencies of ∼79% (S106–S106) and ∼15% (T124–T124).

We have performed the same experiment using proteins without the lipid anchor, but in the presence of POPC liposomes, and did not observe any FRET signals. This shows that the G-domain without the anchor does not form stable dimers. Measurements on the lipidated protein without POPC liposomes resulted in slightly lower FRET efficiencies as described above. Here, the amplitude weighted and averaged fluorophore's lifetime decreased from 1.86 ns to 1.41 ns in measurements with Ras S106-Atto 532 and from 3.56 ns to 3.44 ns in measurements with Ras T124-Atto 532 leading to FRET efficiencies of ∼60% for S106–S106 and ∼10% for T124–T124. This suggests that lipidated Ras proteins in solution interact with each other *via* the lipid anchor.

Experimental details of the EPR measurements are given in ESI Note 7.†

### Computational methods

The protein–protein docking approach is described in ESI Note 2.† The protocol to calculate distance distributions for the predicted models employing the PyMOL plugin for MTSSL Wizard[51] is described in ESI Note 5.†

The dimer structures in accordance with the experimental data were prepared for the simulation by attachment of the membrane anchor, a side chain protonation based on a local p$K_a$ calculation and solvated using the Vedani algorithm using MAXIMOBY (CHEOPS, Germany). The membrane anchors were then embedded into a POPC membrane consisting of 512 lipids. The remaining simulation box was filled with water and a physiological salt concentration of 154 mmol $l^{-1}$ and the simulations were run with Gromacs 2019.[52] The structure preparation and the used protocol including all parameters for simulation runs are described in ESI Note 6.† Simulation results were visualized using VMD 1.9.4 (ref. 53) and PyMOL 2.2. Simulation trajectories were analyzed using the analysis tools of Gromacs 2019,[52] VMD 1.9.4, and QwikMD.[54] Contact patterns were identified using the PyContact[46] and the MAXIMOBY (CHEOPS, Germany) contact matrix algorithm. Details about the input structures and the analysis of the biomolecular simulations are provided in ESI Note 6 and Table S6.†

## Author contributions

TR, KG, and CK designed the research; TR, CT, MS, and JK performed research; CT performed FRET measurements and labeling experiments supervised by CK. TR and MS performed MD simulations. MS performed protein docking, and MTSSL Wizard calculations supervised by TR. JG assisted with the MTSSL Wizard analysis. JS synthesized the lipid anchor. JK performed EPR experiments and related MD simulations. ML assisted with protein expression. TR, CT, MS, JG, JK, and CK analyzed data; TR, CT, MS, KG, and CK wrote the paper with edits from all co-authors. KG and CK obtained funding.

## Funding

This work was supported by Deutsche Forschungsgemeinschaft (DFG, German Research Foundation) Individual Research Grant GE 599/20-1 to KG and KO 3813/1-1 to CK. Further support was provided by the Ministry for Culture and Science (MKW) of North Rhine-Westphalia (Germany) through PRODI to KG and the Protein Research Unit Ruhr within Europe (PURE) funded by the Ministry of Innovation, Science and Research (MIWF) of North-Rhine Westphalia (Germany) to KG.

## Conflicts of interest

There are no conflicts to declare.

## Acknowledgements

We thank Herbert Waldmann and Sascha Gentz for their support with synthesizing the lipid anchor. We thank Iris Bourdos for her support in the creation of N-Ras mutants and expression tests. We thank Léon Beyer and Konstantin Gavriljuk for MALDI measurements and Gregor Hagelueken for technical support with the MTSSL Wizard. We thank Udo Höweler for fruitful discussion of the biomolecular simulation and docking data as well as support with the contact analysis. The plasmids encoding $tRNA^{Pyl}/PylRS^{WT/AF}$ were obtained through an MTA with Prof. Dr Edward Lemke (Johannes Gutenberg University, Biocentre & IMB, Mainz).

## References

1 A. K. Mishra and D. G. Lambright, Invited review: small GTPases and their GAPs, *Biopolymers*, 2016, **105**(8), 431–448.
2 K. Scheffzek, M. R. Ahmadian, W. Kabsch, L. Wiesmüller, A. Lautwein, F. Schmitz, *et al.*, The Ras-RasGAP complex: structural basis for GTPase activation and its loss in oncogenic Ras mutants, *Science*, 1997, **277**(5324), 333–338.
3 R. Gasper and F. Wittinghofer, The Ras switch in structural and historical perspective, *Biol. Chem.*, 2019, **401**(1), 143–163.
4 R. Thapar, J. G. Williams and S. L. Campbell, NMR characterization of full-length farnesylated and non-farnesylated H-Ras and its implications for Raf activation, *J. Mol. Biol.*, 2004, **343**(5), 1391–1408.
5 C. Kötting, J. Güldenhaupt and K. Gerwert, Time-resolved FTIR spectroscopy for monitoring protein dynamics exemplified by functional studies of Ras protein bound to a lipid bilayer, *Chem. Phys.*, 2012, **396**, 72–83, available from: http://www.sciencedirect.com/science/article/pii/S0301010411003636.
6 A. R. Calixto, C. Moreira, A. Pabis, C. Kötting, K. Gerwert, T. Rudack, *et al.*, GTP Hydrolysis Without an Active Site Base: A Unifying Mechanism for Ras and Related GTPases, *J. Am. Chem. Soc.*, 2019, **141**(27), 10684–10701.
7 A. D. Cox and C. J. Der, Ras history: the saga continues, *Small GTPases*, 2010, **1**(1), 2–27.
8 S. Lu, H. Jang, S. Muratcioglu, A. Gursoy, O. Keskin, R. Nussinov, *et al.*, Ras Conformational Ensembles, Allostery, and Signaling, *Chem. Rev.*, 2016, **116**(11), 6607–6665.
9 I. A. Prior and J. F. Hancock, Ras trafficking, localization and compartmentalized signalling, *Semin. Cell Dev. Biol.*, 2012, **23**(2), 145–153.
10 D. K. Simanshu, D. V. Nissley and F. McCormick, RAS Proteins and Their Regulators in Human Disease, *Cell*, 2017, **170**(1), 17–33, available from: https://pubmed.ncbi.nlm.nih.gov/28666118/.
11 K. A. Maegley, S. J. Admiraal and D. Herschlag, Ras-catalyzed hydrolysis of GTP: a new perspective from model studies, *Proc. Natl. Acad. Sci. U. S. A.*, 1996, **93**(16), 8160–8166.
12 M. R. Ahmadian, P. Stege, K. Scheffzek and A. Wittinghofer, Confirmation of the arginine-finger hypothesis for the GAP-stimulated GTP-hydrolysis reaction of Ras, *Nat. Struct. Mol. Biol.*, 1997, **4**(9), 686–689.
13 K. Gerwert, D. Mann and C. Kötting, Common mechanisms of catalysis in small and heterotrimeric GTPases and their respective GAPs, *Biol. Chem.*, 2017, **398**(5–6), 523–533.
14 S. Lu, D. Ni, C. Wang, X. He, H. Lin, Z. Wang, *et al.*, Deactivation Pathway of Ras GTPase Underlies Conformational Substates as Targets for Drug Design, *ACS Catal.*, 2019, **9**(8), 7188–7196.
15 B. Mörchen, O. Shkura, R. Stoll and I. Helfrich, Targeting the "undruggable" RAS - new strategies - new hope?, *Cancer Drug Resist.*, 2019, **2**, 813–826.
16 A. R. Moore, S. C. Rosenberg, F. McCormick and S. Malek, RAS-targeted therapies: is the undruggable drugged?, *Nat. Rev. Drug Discovery*, 2020, **19**(8), 533–552, available from: https://pubmed.ncbi.nlm.nih.gov/32528145/.
17 J. Canon, K. Rex, A. Y. Saiki, C. Mohr, K. Cooke, D. Bagal, *et al.*, The clinical KRAS(G12C) inhibitor AMG 510 drives anti-tumour immunity, *Nature*, 2019, **575**(7781), 217–223.
18 L. Goebel, M. P. Müller, R. S. Goody and D. Rauh, KRasG12C inhibitors in clinical trials: a short historical perspective, *RSC Med. Chem.*, 2020, **11**(7), 760–770.
19 I. A. Prior, P. D. Lewis and C. Mattos, A comprehensive survey of Ras mutations in cancer, *Cancer Res.*, 2012, **72**(10), 2457–2467.
20 K. Inouye, S. Mizutani, H. Koide and Y. Kaziro, Formation of the Ras dimer is essential for Raf-1 activation, *J. Biol. Chem.*, 2000, **275**(6), 3737–3740.
21 J. Güldenhaupt, T. Rudack, P. Bachler, D. Mann, G. Triola, H. Waldmann, *et al.*, N-Ras forms dimers at POPC membranes, *Biophys. J.*, 2012, **103**(7), 1585–1593.
22 R. Spencer-Smith, A. Koide, Y. Zhou, R. R. Eguchi, F. Sha, P. Gajwani, *et al.*, Inhibition of RAS function through targeting an allosteric regulatory site, *Nat. Chem. Biol.*, 2017, **13**(1), 62–68.
23 X. Nan, T. M. Tamgüney, E. A. Collisson, L.-J. Lin, C. Pitt, J. Galeas, *et al.*, Ras-GTP dimers activate the Mitogen-Activated Protein Kinase (MAPK) pathway, *Proc. Natl. Acad. Sci. U. S. A.*, 2015, **112**(26), 7996–8001.
24 M. Chen, A. Peters, T. Huang and X. Nan, Ras Dimer Formation as a New Signaling Mechanism and Potential Cancer Therapeutic Target, *Mini-Rev. Med. Chem.*, 2016, **16**(5), 391–403.
25 C. Ambrogio, J. Köhler, Z.-W. Zhou, H. Wang, R. Paranal, J. Li, *et al.*, KRAS Dimerization Impacts MEK Inhibitor Sensitivity and Oncogenic Activity of Mutant KRAS, *Cell*, 2018, **172**(4), 857–868.
26 S. Muratcioglu, T. S. Chavan, B. C. Freed, H. Jang, L. Khavrutskii, R. N. Freed, *et al.*, GTP-Dependent K-Ras Dimerization, *Structure*, 2015, **23**(7), 1325–1335.
27 M. R. Packer, J. A. Parker, J. K. Chung, Z. Li, Y. K. Lee, T. Cookis, *et al.*, Raf promotes dimerization of the Ras G-

domain with increased allosteric connections, *Proc. Natl. Acad. Sci. U. S. A.*, 2021, **118**(10), e2015648118.
28 J. M. Rhett, I. Khan and J. P. O'Bryan, Biology, pathology, and therapeutic targeting of RAS, *Adv. Cancer Res.*, 2020, **148**, 69–146.
29 E. A. Kovrigina, A. R. Galiakhmetov and E. L. Kovrigin, The Ras G Domain Lacks the Intrinsic Propensity to Form Dimers, *Biophys. J.*, 2015, **109**(5), 1000–1008, available from: https://pubmed.ncbi.nlm.nih.gov/26331257/.
30 J. K. Chung, Y. K. Lee, J.-P. Denson, W. K. Gillette, S. Alvarez, A. G. Stephen, *et al.*, K-Ras4B Remains Monomeric on Membranes over a Wide Range of Surface Densities and Lipid Compositions, *Biophys. J.*, 2018, **114**(1), 137–145.
31 J. K. Chung, Y. K. Lee, H. Y. M. Lam and J. T. Groves, Covalent Ras Dimerization on Membrane Surfaces through Photosensitized Oxidation, *J. Am. Chem. Soc.*, 2016, **138**(6), 1800–1803.
32 S. J. Plowman, C. Muncke, R. G. Parton and J. F. Hancock, H-ras, K-ras, and inner plasma membrane raft proteins operate in nanoclusters with differential dependence on the actin cytoskeleton, *Proc. Natl. Acad. Sci. U. S. A.*, 2005, **102**(43), 15500–15505.
33 I. A. Prior, C. Muncke, R. G. Parton and J. F. Hancock, Direct visualization of Ras proteins in spatially distinct cell surface microdomains, *J. Cell Biol.*, 2003, **160**(2), 165–170.
34 E. Barklis, A. G. Stephen, A. O. Staubus, R. L. Barklis and A. Alfadhli, Organization of Farnesylated, Carboxymethylated KRAS4B on Membranes, *J. Mol. Biol.*, 2019, **431**(19), 3706–3717.
35 P. Prakash, A. Sayyed-Ahmad, K.-J. Cho, D. M. Dolino, W. Chen, H. Li, *et al.*, Computational and biochemical characterization of two partially overlapping interfaces and multiple weak-affinity K-Ras dimers, *Sci. Rep.*, 2017, **7**(1), 40109, available from: https://www.nature.com/articles/srep40109.
36 K.-Y. Lee, Z. Fang, M. Enomoto, G. Gasmi-Seabrook, L. Zheng, S. Koide, *et al.*, Two Distinct Structures of Membrane-Associated Homodimers of GTP- and GDP-Bound KRAS4B Revealed by Paramagnetic Relaxation Enhancement, *Angew. Chem., Int. Ed.*, 2020, **59**(27), 11037–11045.
37 T. Tian, A. Harding, K. Inder, S. Plowman, R. G. Parton and J. F. Hancock, Plasma membrane nanoswitches generate high-fidelity Ras signal transduction, *Nat. Cell Biol.*, 2007, **9**(8), 905–914, available from: https://pubmed.ncbi.nlm.nih.gov/17618274/.
38 T. Tian, S. J. Plowman, R. G. Parton, Y. Kloog and J. F. Hancock, Mathematical modeling of K-Ras nanocluster formation on the plasma membrane, *Biophys. J.*, 2010, **99**(2), 534–543.
39 Y. Zhou and J. F. Hancock, Ras nanoclusters: versatile lipid-based signaling platforms, *Biochim. Biophys. Acta*, 2015, **1853**(4), 841–849.
40 M. Zuberi, I. Khan and J. P. O'Bryan, Inhibition of RAS: proven and potential vulnerabilities, *Biochem. Soc. Trans.*, 2020, **48**(5), 1831–1841.
41 A. Baspinar, E. Cukuroglu, R. Nussinov, O. Keskin and A. Gursoy, PRISM: a web server and repository for prediction of protein-protein interactions and modeling their 3D complexes, *Nucleic Acids Res.*, 2014, **42**(web server issue), W285–W289.
42 B. G. Pierce, K. Wiehe, H. Hwang, B.-H. Kim, T. Vreven and Z. Weng, ZDOCK server: interactive docking prediction of protein-protein complexes and symmetric multimers, *Bioinformatics*, 2014, **30**(12), 1771–1773.
43 D. Schneidman-Duhovny, Y. Inbar, R. Nussinov and H. J. Wolfson, PatchDock and SymmDock: servers for rigid and symmetric docking, *Nucleic Acids Res.*, 2005, **33**(web server issue), W363–W367.
44 D. Schneidman-Duhovny, Y. Inbar, R. Nussinov and H. J. Wolfson, Geometry-based flexible and symmetric protein docking, *Proteins*, 2005, **60**(2), 224–231.
45 T. Plass, S. Milles, C. Koehler, C. Schultz and E. A. Lemke, Genetically encoded copper-free click chemistry, *Angew. Chem., Int. Ed.*, 2011, **50**(17), 3878–3881.
46 M. Scheurer, P. Rodenkirch, M. Siggel, R. C. Bernardi, K. Schulten, E. Tajkhorshid, *et al.*, PyContact: Rapid, Customizable, and Visual Analysis of Noncovalent Interactions in MD Simulations, *Biophys. J.*, 2018, **114**(3), 577–583.
47 B. M. Kearney, C. W. Johnson, D. M. Roberts, P. Swartz and C. Mattos, DRoP: a water analysis program identifies Ras-GTP-specific pathway of communication between membrane-interacting regions and the active site, *J. Mol. Biol.*, 2014, **426**(3), 611–629.
48 L. Brunsveld, H. Waldmann and D. Huster, Membrane binding of lipidated Ras peptides and proteins–the structural point of view, *Biochim. Biophys. Acta*, 2009, **1788**(1), 273–288.
49 Z.-L. Li and M. Buck, Computational Modeling Reveals that Signaling Lipids Modulate the Orientation of K-Ras4A at the Membrane Reflecting Protein Topology, *Structure*, 2017, **25**(4), 679–689.
50 L. D. Hughes, R. J. Rawle and S. G. Boxer, Choose your label wisely: water-soluble fluorophores often interact with lipid bilayers, *PLoS One*, 2014, **9**(2), e87649.
51 G. Hagelueken, R. Ward, J. H. Naismith and O. Schiemann, MtsslWizard: In Silico Spin-Labeling and Generation of Distance Distributions in PyMOL, *Appl. Magn. Reson.*, 2012, **42**(3), 377–391.
52 M. J. Abraham, T. Murtola, R. Schulz, S. Páll, J. C. Smith, B. Hess, *et al.*, GROMACS: high performance molecular simulations through multi-level parallelism from laptops to supercomputers, *SoftwareX*, 2015, **1–2**, 19–25, available from: http://www.sciencedirect.com/science/article/pii/S2352711015000059.
53 W. Humphrey, A. Dalke and K. Schulten, VMD: visual molecular dynamics, *J. Mol. Graphics*, 1996, **14**(1), 33–38.
54 J. V. Ribeiro, R. C. Bernardi, T. Rudack, J. E. Stone, J. C. Phillips, P. L. Freddolino, *et al.*, QwikMD - Integrative Molecular Dynamics Toolkit for Novices and Experts, *Sci. Rep.*, 2016, **6**(1), 26536, available from: https://www.nature.com/articles/srep26536.

# Supplementary Information for
The Ras Dimer Structure

Till Rudack[1,2,*,#], Christian Teuber[1,2,*], Marvin Scherlo[1,2], Jörn Güldenhaupt[1,2], Jonas Schartner[2], Mathias Lübben[1,2], Johann Klare[3], Klaus Gerwert[1,2,#], Carsten Kötting[1,2,#]

[1] Biospectroscopy, Center for Protein Diagnostics, Ruhr University Bochum, 44801 Bochum, Germany
[2] Department of Biophysics, Ruhr University Bochum, 44801 Bochum, Germany
[3] Department of Physics, Osnabrück University, 49074 Osnabrück, Germany

* These authors contributed equally to this work

[#] Corresponding author

Till.Rudack@ruhr-uni-bochum.de
Klaus.Gerwert@ruhr-uni-bochum.de
Carsten.Koetting@ruhr-uni-bochum.de

# Table of Contents

## Supporting Note 1: Ras dimer structural models available in the literature

The literature reports various different contradictory dimer structural models.[1–4] We categorize these models into three main categories based on their dimer interaction sides. The models in category I undergo helix α4 and α5 dimerization, the ones in category II undergo helix α3 and α4 dimerization, while the ones in category III undergo β-sheet dimerization. These categories are further subdivided with respect to their detailed dimer interactions in Fig. S1. Structure I.1 is the protein-protein crystal contact interface that is most prominent among all available Ras X-ray structures.[1] However, several other different protein-protein contact interfaces occur in the deposited X-ray structures. Using biomolecular simulations for N-Ras and a combination of biomolecular simulations and protein docking (RosettaDock[5]) for K-Ras4B, the model I.2 for N-Ras-GDP[1] and two models for K-Ras4B-GTP[4] were obtained, respectively. One of the two K-Ras4B-GTP models has the same contact side as model I.2, and the other one is referred to as model II.1.[4] Model I.3[2] is the first model deposited under the protein data bank (PDB) ID 6W4F, which was obtained by utilizing high ambiguity driven protein−protein docking (HADDOCK) with NMR derived distance restraints of K-Ras4B-GDP attached to a nanodisc.[2] Using the same methods, the authors also published a K-Ras4B-GTP-ɣ-S structure (PDB-ID: 6W4E) referred to as model I.4. Models II.2 (K-Ras4B-GppNHp) and III.1 (K-Ras4B-GTP-ɣ-S)[3] were generated by the protein interactions by structural matching (PRISM) algorithm.[6]

## Supporting Note 2: Protein-Protein Docking

We constructed seven representative Ras monomer G-domains (residue 1 to 172) as input structures for the protein-protein docking servers. One representative model for each isoform (H-Ras, K-Ras4B and N-Ras) of the active conformation with a bound GTP analogon and the inactive conformation with GDP bound (two GDP bound models for H-Ras). As an initial starting point, the monomeric Ras structures from the protein data bank shown in Table S11 were used. Missing atoms and residues were completed using Modeller 9.21.[7] To achieve consistency and minimize the effect of crystallization artifacts due to different C-terminal truncation positions we modeled the C-terminal part helical until residue 172. The assumption that helix α5 ends approximately at residue 172 is in agreement with FTIR measurements [8] and NMR studies.[9, 10]
The resulting structures were sent to the PRISM[6,11], ZDOCK[12] and Symmdock[13,14] docking servers. Table S1 summarizes the resulting 178 dimer structural models, which are categorized based on their interaction sides into 9 main categories. While three of these interaction sides were already identified in the published models, six new interaction sides were detected (IV-IX). The dimer models are categorized as follows: I (contact between the surfaces formed by helices α4 and α5), II (contact between the surfaces formed by helices α3 and α4), III (contact between the surfaces formed by the β-sheets), IV (contact between helices α3 and α4 of one monomer with the β-sheet of the other monomer), V (contact between the helices α4 and α5 of one monomer with the β-sheet of the other monomer), VI (contact between the surfaces formed by helices α5 and the α-sheet), VII (contact between the surfaces formed by helices α4), VIII (contact between the surfaces formed by the helices α2 and α5), IX (involvement of the switch regions of at least one monomer in the dimer interface). Due to the huge variety of predicted dimer models a satisfactory validation of a distinct structural model is impossible without further experimental data. The main categories are further divided into 64 subcategories to distinguish detailed differences in the interaction pattern.

## Supporting Note 3: Preparation of lipidated N-Ras with site specific fluorescence label

### Lipid Anchor Synthesis for N-Ras

The organic synthesis of the lipid anchor Maleimidocaproyl-Gly-Cys(Hexadecyl)-Met-Gly-Leu-Pro-Cys(Farnesyl)-OMethyl was done based on Bader et al.[15] Synthesis of Fmoc-Cys(Farnesyl)-OH (Fig. S10A): In a 100 mL flask 690.61 mg L-cysteine (5.7 mmol) was dissolved in methanol under an argon atmosphere (11 mL) and cooled in an ice bath to 0 °C. The solution was stirred and 7 N ammonia in methanol (15 mL) were added slowly. Farnesyl bromide (1545.6 µL, 5.7 mmol) was added and the mixture was stirred for 3 h at 0 °C and 1 h at room temperature. Subsequently, the solvent was evaporated under reduced pressure. The remaining white solid was transferred into a 50 mL falcon tube and washed with n-pentane. The pentane suspension was centrifuged for 10 min (4500 rpm) and the supernatant was disposed. This procedure was repeated three times to get rid of unbound farnesyl bromide. The residue was placed in a round bottom flask and dichloromethane was added (50 mL). The resulting suspension was cooled to 0 °C and 880 µL triethylamine (6.28 mmol), 2.12 g Fmoc N-hydroxysuccinimide ester (6.28mmol) were added. The reaction mixture was stirred over night at room temperature. The suspension was filtrated to get rid of free Fmoc and the solvent was evaporated under reduced pressure. Purification was done by column chromatography using a gradient of 0-4% methanol in dichloromethane (DCM). Identification of the fractions was done by thin layer chromatography (Rf(product)=0.55, Rf(Fmoc)=0.9, 10% methanol in DCM). The product was a slightly yellow oil (yield 3.1 g, 98%), which was characterized by 1H-NMR.

Synthesis of Fmoc-Cys(Hexadecyl)-OH (Fig. S10B): 5 g of Fmoc-Cys(Trityl)-OH were dissolved in DCM (125 mL) in a round-bottom flask filled with argon. To the stirred solution 5 mL of trifluoroacetic acid and 3.75 mL of triethylsilane were added and allowed to react for 4 h at room temperature. Toluene was added (30 mL) and the crude product was coevaporated three times. Afterward, the crude product was transferred into a falcon tube and n-pentane was added. The tube was placed into a sonicator to mix the solution. By centrifugation the product (Fmoc-Cys-OH) was separated and the process was repeated three times.

To get rid of the oxygen, DCM was purged with argon for 30 min in a sonicator. The obtained 2.9 g of Fmoc-Cys-OH were dissolved in DCM (30 mL) and 7.8 mL hexadecane / 698 mg azobisisobutyronitrile (AIBN) were added. The mixture was refluxed at 85 °C for 3 h. Subsequently, the mixture cooled to room temperature and the solvent was removed with a rotating evaporator. The final product was purified using flash chromatography (silica gel) with a gradient of 0-4% methanol in DCM. The fractions containing the product were determined with TLC. The synthesis yielded in 3.4 g (72%) and the product was characterized by $^{1}$H-NMR.

Activation and Loading of 2-Chlortritylchloride Resin: The 2-chlortritylchloride resin (800 mg, loading 0.77 mmol/g) was activated by adding 1.5 equivalent of thionyl chloride in 10 mL DCM. The mixture was stirred for 1 h at room temperature. Afterward, the resin was washed three times with DCM to get rid of the thionyl chloride. The resin and the Fmoc-Cys-OH were dried in vacuum overnight. Subsequently, the resin was dissolved in 7 mL DCM and mixed for 30 min under inert gas. After the addition of 1 g Fmoc-Cys-OH and 630 uL N,N-Diisopropylethylamine in 5 mL DCM to the activated resin the mixture was shaken for 3 h. The synthesis was done in a 0.25 mM scale with 320 mg of total resin. The loaded resin was divided into two equal parts. One part was immediately stored at -20°C under argon and the other one was used for the coupling in the solid phase peptide synthesis (SPPS).

Solid Phase Peptide Synthesis and Purification: The peptide sequence (Maleimidocaproyl-Gly-Cys(Hexadecyl)-Met-Gly-Leu-Pro-Cys(Farnesyl)-OMethyl) was synthesized with an automated solid-phase peptide synthesizer. For the SPPS 160 mg resin were employed. The cleavage of the peptide from the resin was done in a syringe. The resin was washed four times with DCM (20 mL). Subsequently, the resin was mixed with 1% trifluoroacetic acid (TFA) and 2% triethylsilane (TIS) in DCM for 30 min. This procedure was repeated three times to ensure a complete separation. After washing with DCM, the solvent was removed in rotating evaporator and three times coevaporated with toluene (10 mL). The yield of the crude peptide was 125 mg (95%). The crude peptide was purified using a preparative HPLC with a diphenyl-column (Vydac, Columbia, USA) and an acetonitrile gradient (50%→100%, 15 min, 0.08% TFA). After purification 93 mg (74%) of the desired peptide with lipid anchor were obtained.

Methylation of the Lipid Anchor (Fig. S11C): The last synthesis step was the methylation of the Cys(Far). Under an argon atmosphere 15 mg of the anchor were dissolved in toluene/methanol (9:1) and 0.9 equivalents of trimethylsilyldiazomethane ($TMSCHN_2$) were added. The mixture was stirred for 30 min and the solvent was evaporated.

The product was dissolved in dichloromethane and purified on a silica column with dichloromethane/methanol (97:3) as solvent. The fractions were characterized with ESI-MS. The product fractions were pooled and concentrated. The yield was 9.5 mg (63%). The product was characterized with ESI-MS 1316 g/mol $[M+H]^+$ and 1338 g/mol $[M+Na]^+$. The ESI-Spectrum of the final product is presented in Fig. S11D. The complete structure of the synthesized peptide Maleimidocaproyl-Gly-Cys(Hexadecyl)-Met-Gly-Leu-Pro-Cys(Farnesyl)-OMethyl is shown in Fig. S11E.

**Finding suitable labeling sites**

In order to find suitable labeling sites for the fluorophores or the spin-label, we performed expression experiments in *E.coli*. Therefore, 50 ml *E.coli* cultures were incubated and mixed with the unnatural amino acid as described below. Afterwards, the cells were disrupted and the homogenate, the supernatant as well as the pellet was tested for N-Ras (1-181) content via Western-Blot analysis with an antibody against the N-Ras C-terminus. Fig. S1 shows that N-Ras K88TAG, S106TAG and T124TAG exhibit more N-Ras in the supernatant as N-Ras V109TAG, D126TAG and P121TAG. In order to label opposing sites from N-Ras, we have finally chosen S106 and T124 as labelling sites (Fig. 2D).

**Preparation of semisynthetic lipidated N-Ras protein with unnatural amino acids**

We used a human N-Ras gene (amino acids 1-181) cloned in a pBAD-Vector in such a way that the complementary amino acid regions to H-Ras have been replaced by the human H-Ras codon in order to maximize the protein yield. The N-Ras protein was expressed in *E.coli* BL21 AI cells from Thermo Fisher Scientific (Waltham, MA, USA) with site specifically incorporated unnatural amino acids (UAAs) by the amber suppression strategy . Therefore, two plasmids were used: 1) pBAD_N-Ras1-181_S106TAG/T124TAG _±_C118S/E49Q_S106TAG_C118S_D154N for N-Ras and 2) a plasmid encoding $tRNA^{Pyl}/PylRS^{WT/AF}$ obtained from the Lemke group[16] for the incorporation of the unnatural amino acid N-Propargyl-L-Lysine (PrK; $PylRS^{WT}$) or Cyclooctyne-Lysine (SCO; $PylRS^{AF}$) from SiChem GmbH (Bremen, Germany).[16, 17] The C118S mutation was introduced to prevent the lipid anchor from binding to this position. The serine was chosen as a substitution for cysteine to keep potential side effects as small as possible. The cells were transfected with these two plasmids and a 50 ml LB-medium culture with 20 µg/ml Chloramphenicol (Cm), 50 µg/ml Ampicillin (Amp) was incubated at 37 °C overnight. The next day, a 4 Liter TB-medium culture with 20 µg/ml Cm, 50 µg/ml Amp was inoculated with a starting

$OD_{600}$ = 0.05. The culture was incubated at 37 °C until an $OD_{600}$ = 0.2 – 0.4 was reached. The unnatural amino acid with a concentration of 100 mM in 0.2 M NaOH, 15% (v/v) DMSO, diluted 1:4 with 1 M HEPES was added to the cells for a 1 mM final concentration of unnatural amino acid in the culture. The overnight protein expression at 30 °C was induced with 0.02% (w/v) arabinose (Sigma-Aldrich, St. Louis, MO, USA) at an $OD_{600}$ = 0.6 – 0.8. The cells were harvested via centrifugation at 5000 g and resuspended in buffer (30 mM Tris (pH 7.5), 5 mM $MgCl_2$, 5 mM DTT, and 20 µM GDP). The cells were disrupted through microfluidization and N-Ras was isolated by anion exchange chromatography and size exclusion chromatography. The coupling of the lipid anchor at position C181 via a maleimide-group was modified based on a previously mentioned protocol.[18]

Coupling of N-Ras with the Lipid Anchor: The lipid anchor was used in a large excess (6 mg, 4.47 µmol) and was dissolved in 80 µL methanol. Subsequently, 7 mg of N-Ras (0.35 µmol) were added in a buffer containing 5% 3-[(3-Cholamidopropyl)dimethylammonio]-1-propanesulfonate (CHAPS) and 4% Triton X-100 (50 mM Tris, pH 7.4, 100 mM NaCl, 2 mM $MgCl_2$). The mixture was stirred at 4 °C for 16 h. The purification was done by gelfiltration using a buffer with 0.4 % Triton X-100. Afterwards the buffer was exchanged to a detergent free buffer (50 mM Hepes pH 7,4, 50 mM NaCl, 2 mM MgCl2, 20 µM GDP). To completely remove residual detergent, a Pierce Detergent Removal Spin Column (Thermo Fisher, Rockford, IL, USA) was applied. The yield was usually around 25%. The lipidated proteins were analyzed by MALDI or SDS-PAGE (Fig. S12).

To check whether the lipid anchor (MW = 1316 Da) is coupled to the protein, we analyzed the unmodified and the modified protein fraction using MALDI mass spectrometry or SDS-PAGE. The latter was performed if the samples could not be ionized, as it was the case with N-Ras T124PrK C118S and N-Ras E49Q S106PrK C118S D154N. Fig. S12A shows the MALDI mass spectrometry results for N-Ras WT and the mutant N-Ras S106PrK before and after lipidation. The mass differences of 1324 Da (N-Ras WT) and 1314 Da (N-Ras S106PrK) show, that the lipid coupling was successful. Fig. S12B shows the SDS-PAGE results for N-Ras T124PrK C118S and N-Ras E49Q S106PrK C118S D154N before and after lipid coupling. It is observed that the protein fractions “+ lipid anchor” have a larger mass in comparison to the unmodified protein “- lipid anchor”. Thus SDS page is used to determine the lipid coupling efficiency.

**POPC liposome preparation**

POPC was dissolved in chloroform at a concentration of 15 mg/ml. The $CHCl_3$ was evaporated using a nitrogen stream followed by incubation in vacuum (20 mbar) for 1 h. The lipid was then resuspended with buffer (50 mM Hepes (pH 7.5), 50 mM NaCl, 2 mM $MgCl_2$, and 20 µM GDP) to a final concentration of 50 mM. The POPC suspension was extruded (20 times, 400 nm filter). The size of the generated liposomes was checked by dynamic light scattering.

**Coupling of fluorophores**

For the time correlated single photon counting (TCSPC) experiments, the FRET-pair Atto 532 azide (donor)/Atto 655 azide (acceptor) from ATTO-TEC GmbH (Siegen, Germany) was site specifically coupled to the positions 106 and 124 of the N-Ras protein, respectively. For this purpose we used the copper (I) catalyzed azide-alkyne cycloaddition leading to 1,4-disubstituted 1,2,3-triazoles.[19] The final concentrations used are summarized in Table S9.

First $CuSO_4$ (final concentration: 0.1 mM) was mixed with the ligand Tris(3-hydroxypropyltriazolylmethyl)amine (THPTA) from Lumiprobe GmbH (Hannover, Germany) (final concentration: 0.5 mM). Next, the copper (II) ions were reduced to copper (I) with sodium ascorbate (final concentration: 2.5 mM), the solution has to appear colorless. Further, benzoic acid (final concentration: 20 µM)[20] as well as the protein with the unnatural amino acid PrK (final concentration: 24 µM) and the fluorophore (final concentration: 1 mM) were added. Buffer (50 mM

Hepes (pH 7.5), 50 mM NaCl, 2 mM $MgCl_2$, and 20 µM GDP) was added to the solution to a final volume of 100 µl. The unreacted fluorophore molecules were removed after incubation (31 °C, 2 h) using 4-5 Zeba™ Spin Desalting Columns (0.5 ml, 7 kDa cutoff) from Thermo Fisher Scientific until no more dyes were present in the throughflow. The labeling efficiencies were determined by the ratio of the fluorophore and protein concentration. The coupling efficiencies are also summarized in Table S10.

**Coupling of the spin label Azido-Proxyl**

Purified and lipidated N-Ras T124-SCO was incubated overnight (30 °C, 20 h, shaking) in buffer containing 50 mM HEPES (pH 8.0), 2 mM $MgCl_2$, and 0.5 mM GDP with 5 mM azido-proxyl (from a 200 mM stock solution in DMSO, 2.5/100 v/v). Unbound spin labels were removed using Zeba desalting columns (2 ml, 7 kDa cutoff, 2 runs). Finally, the protein solutions were concentrated in Amicon Ultra-4 centrifugal devices (3 kDa cutoff) to reach a final protein concentration of 50 µM. The labelling efficiency was determined to be approximately 10%.

**Sample composition for FRET and EPR measurements**

In the FRET experiments with lipidated N-Ras, the following sample composition (70 µl volume) was used: 100 nM donor protein, 335 nM acceptor protein, 100 µM POPC (400 nm liposomes), and 2.5 mM DTT in buffer (50 mM Hepes (pH 7.5), 50 mM NaCl, 2 mM $MgCl_2$, and 20 µM GDP. The data were recorded after 3 h incubation at 25 °C. All measurements with lipidated protein and POPC liposomes were reproduced on a second sample and each sample was measured four times. For measurements without POPC liposomes one sample was measured four times. For the measurement of non-lipidated samples, 100 nM donor protein, 240 nM acceptor protein, 100 µM POPC (400 nm liposomes), and 2.5 mM DTT were used. These samples were measured four times as well. Prior to EPR measurements, POPC liposomes were incubated with spin labeled Ras in a protein-lipid ratio of 1:100 for 15 min at RT.

## Supporting Note 4: Experimental set up and analysis of FRET measurements

**TCSPC measurements and analysis**

The fluorophore's lifetimes were measured using a TCSPC setup from PicoQuant (Berlin, Germany). The data were acquired with a pulsed laser-diode, emitting at 510 nm (LDH-D-C-series) driven by a PDL 800-D laser driver, a photomultiplier detector module (PMA 182-N-M) equipped with a holder for proper filters, and a Pico Harp 300 Photon-Counting System. To avoid pile-up effects, the laser intensity was adjusted so the detected photon count rate did not exceed 1% of the excitation rate (10 MHz). Photon events were stored in histograms bins with a width of 4 ps. The recording time for each sample was 40 min and the integration time for each histogram was 600 s, resulting in 4 histograms for each sample. The FRET efficiency was determined by measuring the donor's lifetime with ($\tau_{DA}$) and without ($\tau_D$) the presence of the acceptor. In this way, fluorescence data were obtained for N-Ras S106-Atto 532/Atto 655, N-Ras T124-Atto 532/Atto 655 C118S, and N-Ras E49Q S106-Atto 532/Atto 655 C118S D154N. Data were analyzed using the FluoFit Pro software from PicoQuant (Berlin, Germany). The histograms were iteratively reconvoluted by using the instrument response function (IRF) with equation 1.

$$I(t) = \int_{-\infty}^{t} IRF\,(t') \sum_{i=1}^{n} A_i \cdot e^{\frac{t-t'}{\tau_i}} dt' \qquad (1)$$

Where n is the required number of exponential functions, t is the time (ns), $A_i$ is the amplitude of the respective exponential term, and $\tau_i$ is the corresponding lifetime. The data of the measurements were evaluated with 3 functions, except the data of the measurement with the fluorophores coupled to T124 of lipidated N-Ras without POPC where 2 functions were used. The resulting lifetimes were amplitude weighted using equation 2.

$$\tau_{a.w.=}\frac{A_1\cdot\tau_1+A_2\cdot\tau_2+\cdots+A_n\cdot\tau_n}{A_1+A_2+\cdots+A_n} \qquad (2)$$

The FRET efficiency E was calculated using the amplitude-weighted lifetimes according to equation 3.

$$E = 1-\frac{\tau_{DA}}{\tau_D}=\frac{R_0^6}{R_0^6+r^6}\rightarrow r=(\frac{R_0^6\cdot(1-E)}{E})^{\frac{1}{6}} \qquad (3)$$

**Determination of the corrected FRET efficiencies**

Our sample consists of three types of Ras molecules, with D = donor label, A = acceptor label, and X = unlabeled protein. Unlabeled protein is always present since the labeling efficiencies were not 100%. Thus, the detected lifetime $\tau_{DA}$ consists of signals derived from Ras dimers with and without acceptor. Therefore, a corrected FRET efficiency ($E_{corr}$) must be used. This is the FRET efficiency that would be measured in the case of 100 % dimers with one donor and one acceptor label as assumed in formula 1. $E_{corr}$ is determined as described in the supplementary information.

**Calculation of the Försterradius $R_0$**

$R_0$ is determined to be:

$$R_0 = 0{,}211\cdot(J\kappa^2\Phi_{FD}n^{-4})^{\frac{1}{6}} \qquad (4)$$

For the calculation of $R_0$ the spectral overlap integral J(λ) ($nm^4\cdot M^{-1}\cdot cm^{-1}$) between the donor's emission and the acceptor's absorbance spectrum is needed and is defined as:

$$J(\lambda)=\frac{\int_{-\infty}^{\infty}F_D(\lambda)\cdot\varepsilon_A(\lambda)\cdot\lambda^4\,d\lambda}{\int_{-\infty}^{\infty}F_D(\lambda)\,d\lambda} \qquad (5)$$

Therefore, the emission spectrum of Atto 532 (donor) and the absorption spectrum of Atto 655 (acceptor) were recorded between 520 and 700 nm. The Lambert-Beer's-Law was used to transfer the acceptor-absorption spectrum to an extinction-coefficient-spectrum. J (λ) was determined to be:

$$J(\lambda)=\frac{\int_{520}^{700}F_D(\lambda)\cdot\varepsilon_A(\lambda)\cdot\lambda^4\,d\lambda}{\int_{520}^{700}F_D(\lambda)\,d\lambda}=\frac{1.8647\cdot10^{19}}{1.1632\cdot10^{4}}$$

$$=1.6031\cdot10^{15}$$

$$[J]=[M^{-1}\cdot cm^{-1}\cdot nm^4] \qquad (6)$$

$\kappa^2$ is the dipole orientation factor of the fluorophores and amounts to 2/3 of free rotating fluorophores as we expect in our experiments. The quantum yield $\Phi$ is 0.9 for Atto 532 as stated by the manufacturer and n is expected to be 1.4. With this, $R_0$ is calculated as followed:

$$R_0 = 0.211 \cdot (J\kappa^2 \Phi_{FD} n^{-4})^{\frac{1}{6}} = 53.6 \text{ Å} \quad (7)$$

Using the Förster radius, the FRET-efficiencies were transferred into distances according to equation 4. The averages of the measurements with the related standard deviations were calculated. The standard deviation of the nucleotide-nucleotide distance (46 ± 6 Å) of the previously mentioned measurements [1] was adapted to our error calculation and resulted in 46.3 ± 1.4 Å.

**Calculation of the corrected FRET efficiency**

In order to calculate the corrected FRET efficiency $E_{corr}$ that is connected to the distance of interest, we have to consider our sample composition. An example is given in Table S12. Dimers are randomly formed between donor labeled Ras (D), acceptor labeled Ras (A) and unlabeled Ras (X) in the sample. The probability of each dimer composition is calculated in the column "Probability" of Table S12 based on the fractions of each form. Only the fluorescence of the DA and AD dimers can be influenced by FRET. The dimers without a donor label will not give rise to any fluorescence signal. The dimers XD, DX and DD (weighted twice) will give rise to a fluorescence signal that is not influenced by FRET, because of the lack of an acceptor. The measured experimental fluorescence lifetime $\tau_{exp}$ is therefore a weighted average value of the lifetimes without ($\tau_D$) and with ($\tau_{DA}$) acceptor, each multiplied with the respective fraction:

$$\tau_{exp} = \text{fraction without acceptor} \cdot \tau_D + \text{fraction with acceptor} \cdot \tau_{DA} \quad (8)$$

For the calculation, the ratio of donor labeled protein in complex with an acceptor with all donor labeled proteins has to be used. As an example for a sample with D = 100 nM, A = 335 nM, X = 403 nM is shown below. Here, 40 % (0.096 out of 0.238) of the donor labelled protein is in a dimer with an acceptor labelled protein. This means for the lifetime $\tau_{DA}$:

$$\tau_{DA\,exp} = 0.6 \cdot \tau_D + 0.4 \cdot \tau_{DA}$$

$$\tau_{DA} = 2.5 \cdot \tau_{DA\,exp} - 1.5 \cdot \tau_D \quad (9)$$

The corrected FRET efficiency $E_{corr}$ that is used for the distance calculation is calculated as follows:

$$E_{corr} = 1 - \frac{2.5 \cdot \tau_{DA\,exp} - 1.5 \cdot \tau_D}{\tau_D} = \left(1 - \frac{\tau_{DA\,exp}}{\tau_D}\right) \cdot 2.5 \quad (10)$$

We calculate the fluorophore distances based on the determined FRET efficiencies according to

$$E = \frac{1}{1 + \left(\frac{r}{R_0}\right)^6} \quad (4)$$

where E is the FRET efficiency, r is the distance between the donor and acceptor fluorophore. The Förster radius $R_0$ = 53.6 Å was calculated as described in materials and methods. The calculation leads to r = 43.3 ± 2.3 Å for lipidated N-Ras on POPC liposomes with fluorophores at position 106 and to r = 72 ± 3.5 Å for lipidated N-Ras on POPC liposomes with fluorophores at position 124. The distance between the nucleotides (46.3 ± 1.4 Å) was obtained from the literature [9] and subjected to the error calculation used in this manuscript.

## Supporting Note 5: Calculation of distance distributions using the PyMOL MtsslWizard

The dimer conformations (Table S3) were evaluated based on the agreement with FRET and EPR experiments. The distance distributions for the three FRET pairs S106-Atto532/S106-Atto655, T124-Atto532/T124-Atto655, MANT-Ribose/TNP-Ribose and for the EPR label pair T124-Proxyl/T124-Proxyl of a representative structure of each the 64 identified conformation and their subcategories were calculated using the PyMOL plugin MtsslWizard [21]. The fluorophores Atto 532, Atto 655, Mant-GDP, and TNP-GDP were integrated in the software by following manufacturer's instructions. The EPR label proxyl was already available in the software. The "vdW restraints" setting was set to "loose" and the parameters have been set to try to find 200 rotamers. First, the fluorophore Atto532 was superimposed to the backbone of residues S106 of monomer A and Atto655 to S106 of monomer B. Then, the mtsslWizard plugin generated conformational ensembles and calculated the corresponding distance distributions between the fluorophores as shown exemplarily in Fig. S5. A gaussian fit of the distance distribution gives the mean values and standard deviations of the FRET distance. The same protocol was carried out for T124A/T124B and for T124A-Proxyl/T124B-Proxyl. For the nucleotides, the FRET-pair Mant-/TNP-Ribose was superimposed on the ribose group of the nucleotide. In Table S3 all mean distances and standard deviations are summarized, compared, and evaluated with respect to the agreement with the experimental values.

## Supporting Note 6: Biomolecular simulations

### Workflow and run parameters

In the following the general workflow and the parameters used for all biomolecular simulations performed in this publication with exception of the SCO-proxyl simulations are described. Dimer structures were prepared for simulation using the MOBY/MAXIMOBY program package (CHEOPS Molecular Modeling, Altenberge, Germany). The protein was protonated based on pK(a) calculation. Experimentally resolved protein internal water molecules were deleted and then water molecules of the first solvation shell were added using the Vedani algorithm, which is based on the directionality of hydrogen bonds. Energetically unfavorable side chain and back bone conformations were visualized and interactively optimized with MOBY. Next, the dimer structure was placed with the anchors attached to a POPC bilayer analog as previously described [1]. A cubic simulation box with periodic boundary conditions filled with TIP4P water and a physiological salt concentration of 154 mmol/l, using sodium cations and chlorine anions was generated. The ion ratio was adjusted to ensure the neutral charge of the simulation system.

Classical molecular mechanic simulations were performed with GROMACS 2019[22] using the optimized-potentials-for-liquid-simulations all-atom (OPLS-AA) force field. The parameters for GTP and GDP were the same as the ones presented by Rudack et al.[23] The parameters for the

palmitoyl and farnesyl anchor of Ras were the same as the ones used by Güldenhaupt et al.[1] For the POPC bilayer previously reported parameters from Ulmschneider et al.[24] were used.
Electronic interactions were determined by the Fast Particle-Mesh Ewald method using a grid spacing of 0.12 nm, fourth order spine interpolation and a cut-off value of 1.0 nm. For van der Waals interactions, a cut-off value of 1.0 nm was employed. All bonds were constrained to their equilibrium length using the LINCS algorithm.
First, the system energy was minimized using the steepest descent algorithm, constraining the protein and the Vedani water molecules to minimize the bulk water molecules and the membrane lipids. Subsequently, a conjugated gradient minimization was performed while constraining only the protein backbone, to allow for further optimization of the side chains and the Vedani water molecules. The system was heated up over a course of 1.6 ns with a linear gradient from 150 K to 310 K while restraining the protein. Next, an NVT equilibration run (number of atoms n, the volume V, and the temperature T are constant and the pressure is free) with restrained protein atoms was performed followed by an NPT equilibration run (number of atoms n, the pressure p, and the temperature T are constant and the volume is free) with the protein backbone restrained. Pressure and temperature were kept at constant values of 1 standard atmosphere and 310 K, respectively, using a Berendsen barostat with a coupling constant of 1.0 ps and a modified Berendsen thermostat (V-rescale) with a coupling constant of 0.1 ps. The final production run was carried out using time intervals of 2 fs.

**Input structure preparation**
We aligned the initial N-Ras-GDP monomer to all selected conformations to transform them all to N-Ras-GDP dimers for further computational refinement. We picked N-Ras-GDP as we performed all experiments in this publication with N-Ras-GDP. Next, we connected the HVR and the anchor to the dimers to attach them to a POPC membrane. Therefore, the region from residue 173 to 186, which is not resolved in any x-ray structures due to its flexibility, was taken from an equilibrated simulation structure from Güldenhaupt et al.[1] and connected to the above obtained G-domains of the dimer structure. Finally, all systems are simulated following the workflow and parameters given in biomolecular simulations sections of material and methods.

**Analysis**
The simulations were analyzed as follows. The RMSD calculation was performed with Gromacs 2019 for the Cα atoms of the residue 1-172 with a time step of 5 ps. Contact analysis was done within the MOBY/MAXIMOBY program package. Every simulation was divided in 1000 frames and analyzed regarding hydrogen bonds/salt bridges and van der Waals contacts. The analysis of hydrogen bonds/salt bridges is based on distance as well as geometrical conditions. The resulting contact matrix displays a binary result for every frame (contact or no contact). For every ten frames, a representative frame was written so that the final contact matrix contained 100 frames. The intermolecular contacts between the monomers are shown in Fig. S7.
The calculation of the representative structure started with the same 1000 frame contact matrix with two additional components: A secondary structure analysis for every residue based on the psi and phi angles and an assignment of side chain chi angles in categories of 60° increments. The frame with the least difference to all other frames was taken as the representative structure.
For every representative structure the distance distribution for the three FRET pairs S106-Atto532/S106-Atto655, T124-Atto532/T124-Atto655, MANT-Ribose/TNP-Ribose and for the EPR label pair T124-Proxyl/T124-Proxyl was calculated as described in supporting note 6.

Conformation I.5 displays an equilibrated RMSD after 400 ns and shows a stable one-sided salt bridge between D154/R161 (Fig. S7). This contact is also present and stable in all other

simulations except I.1 and I.6. Simulations I.7 and I.8 exhibit a two-sided D154/R161 contact. Several other intermolecular contacts are observed (Fig. S7). Analysis of these shows a stabilizing effect of the E49-H131 contact, while others fluctuate between simulations and do not show a consistent pattern (Table S6).
The overall unstable binding pattern of I.6 correlates with its RMSD, which does not equilibrate in the given time. I.7 displays a stable RMSD after approximately 500 ns, while I.8 is stable after 250 ns (Fig. S7). The simulations I.9 and I.10 equilibrate within the first 50 ns (Fig. S7) and their representative structures fulfill the experimental criteria for the FRET and EPR distance distributions (Table S7). Conformation I.11 does not equilibrate in the given simulation time, while I.12 stabilizes after 300 ns (Fig. S7).

## Supporting Note 7: Experimental set up and analysis of EPR measurements

**EPR spectroscopy**
DEER (also known as PELDOR) experiments were performed at Q-band frequencies (34 GHz) with a Bruker Elexsys 580 spectrometer equipped with a Q-band bridge and a 150 W Q-band travelling wave tube (TWT) amplifier (Applied Systems Engineering, Fort Worth, TX, USA), using a Bruker Flexline resonator ER 5106QT-2. The 3 mm outer diameter EPR quartz capillaries were loaded with 50 µl of proteoliposome suspension containing 25% glycerol. The temperature was stabilized at 50 K using a continuous flow helium cryostat CF935 (Oxford Instruments, Abingdon, UK) regulated by temperature controller ITC 503S (Oxford Instruments). All measurements were performed using the four-pulse DEER sequence[25, 26]:

$\pi/2\ (\nu_{obs})$ - $\tau_1$ - $\pi\ (\nu_{obs})$ - $t'$ - $\pi\ (\nu_{pump})$ - $(\tau_1 + \tau_2 - t')$ - $\pi\ (\nu_{obs})$ - $\tau_2$ - echo

A two-step phase cycling, (+)x and (-)x, was performed on $\pi/2$ ($\nu_{obs}$). Time t' was varied, while $\tau_1$ and $\tau_2$ were kept constant. The dipolar evolution time was given by $t = t' - \tau_1$. Data were analyzed only for $t > 0$. The resonator Q was set to approximately 1500 (as determined by the spectrometer software). The pump frequency $\nu_{pump}$ was set 30 MHz higher than the resonator dip center, coinciding with the maximum of the EPR spectrum. The observer frequency $\nu_{obs}$ was 20 MHz lower than the dip center, yielding a total frequency offset of -50 MHz. The observer pulse lengths were 16 ns for $\pi/2$ and 32 ns for $\pi$ pulses and the pump pulse length was 16 ns. Proton modulation was averaged by adding traces at 8 different $\tau_1$ values, starting at $\tau_{1,0}$ = 536 ns and incrementally adding 8 ns ($\Delta\tau_1$ = 8 ns). Data points were collected in 8-ns time intervals. The total measurement time was approximately 72 h. Data analysis was performed with the software package DeerAnalysis[27], using a model-based fit assuming a single Gaussian distribution of distances.

**Biomolecular simulations to analyze the conformational space sampled by SCO-Proxyl**
Biomolecular simulations were used to analyze the conformational space sampled by the SCO-Proxyl spin label side chain at positions 124 of the dimer models. The simulations were carried out in YASARA structure, utilizing the Amber03 force field[28] and Particle Mesh Ewald summation for long range electrostatic interactions with a cutoff at 8 Å. The time step for the calculation of intramolecular forces was 0.5 fs (simulation sub-step). The intermolecular forces have been calculated every 2 simulation sub-steps. The simulation temperature was 298.0 K. Temperature control was carried out by rescaling atom velocities. Pressure control was achieved by keeping the solvent ($H_2O$) density at 0.997 g/ml and rescaling the simulation cell along all three axes.

During the 30 ns long simulations the protein backbone was kept fixed. Simulation snapshots were acquired in steps of 25 ps and analyzed in terms of inter spin distances (nitroxide-nitroxide). For preparation of the ‘rotamer clouds’ spin label side chain structures were acquired in steps of 250 ps.

## Supplementary Figures

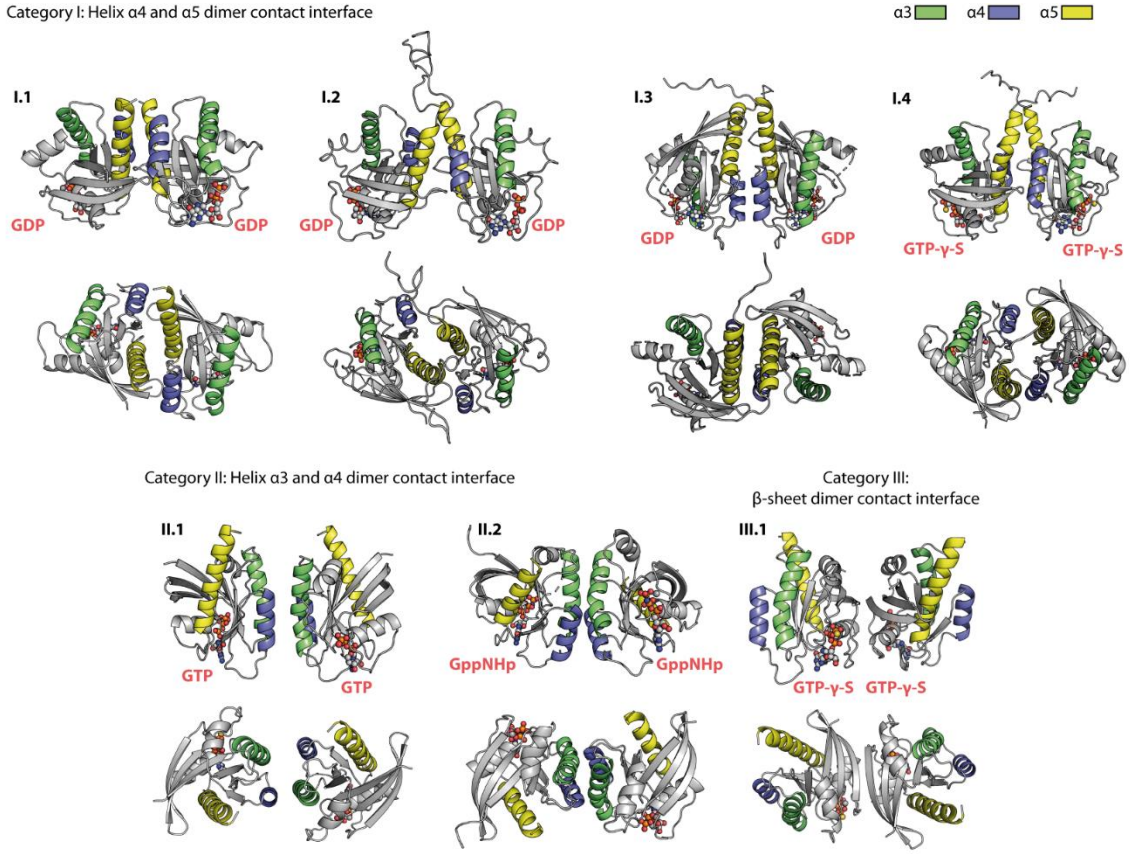


**Fig. S1. Diversity of previously proposed different Ras dimer structural models.** To order the huge variety of the published dimer structural models we divided them into three substantially different main categories based on the relative orientation of the monomers. These categories are further subdivided based on the detailed dimer interaction interface. The key helices are represented by different colors (helix α3: green, helix α 4: blue, helix α5: yellow) and the nucleotides are displayed in spherical shape. The category I dimer interface is formed by contacts of helices α 4 and α 5. Model I.1 is the most common interface found in the crystal packing of Ras X-ray structures of all isoforms.[1] Model I.2 is the full-length membrane attached N-Ras-GDP dimer structure resulting after refinement of model I.1 through biomolecular simulations.[1] Model I.2 is very similar to a model for K-Ras-GTP obtained by protein docking combined with biomolecular simulations.[4] Model I.3 (protein data bank ID 6W4F) was obtained using the high ambiguity driven protein−protein docking (HADDOCK) protein docking software with distance restraints from NMR.[2] Using the same methods, the authors also published a K-Ras4B-GTP-ɣ-S structure (PDB-ID: 6W4E) referred to as model I.4. The category II dimer interface is formed by contacts of helices α3 and α4. Model II.1 is a structure obtained through simulations performed by Prakash et al[4]. Model II.2 is the "α-Homodimer" obtained from the PRISM protein-protein docking server[6] by Muratcioglu et al[3]. Model III.1 is the "β-Homodimer"[3] also obtained in the same study through PRISM.

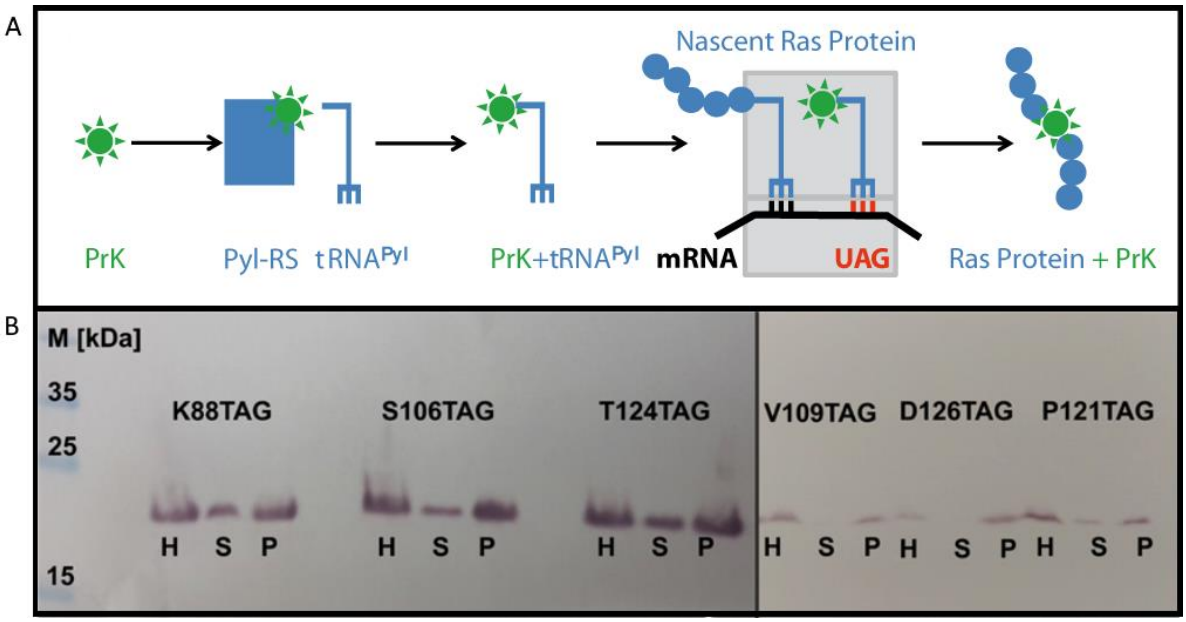


**Fig. S2: Experimental strategy to incorporate unnatural amino acids into Ras.** For site specificity of the second modification, we developed the strategy shown in **A** to incorporate a biorthogonal alkyne moiety as part of the unnatural amino acids (uaa) N-propargyl-L-lysine (PrK) and Cyclooctyne-Lysine (ScO) into N-Ras. **B** shows Western Blot results that were obtained after the incorporation of the unnatural amino acid at different sites of N-Ras. A clear band in the supernatant represents a good possibility to obtain N-Ras with unnatural amino acid at respective site. Only the mutants K88TAG, S106TAG and T124TAG show a clear band in the supernatant. H = Homogenate, S = Supernatant, P = Pellet. The position T124 was chosen for the attachment of the fluorophore, as it displayed the highest yield. Due to the proximity of K88 to T124 we chose S106 as the second label site, resulting in a better distribution of the fluorophores across the protein.

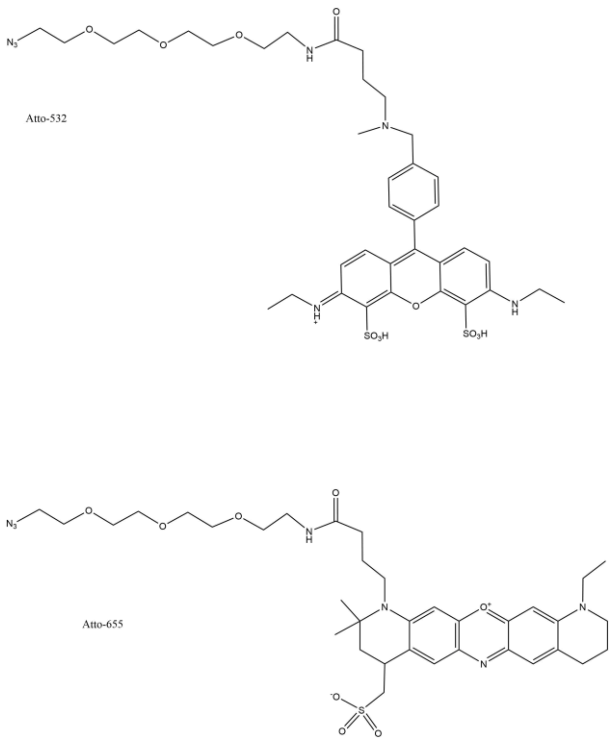


**Fig. S3: Chemical drawings of the FRET labels Atto-532 and Atto-655 used for FRET experiments.**

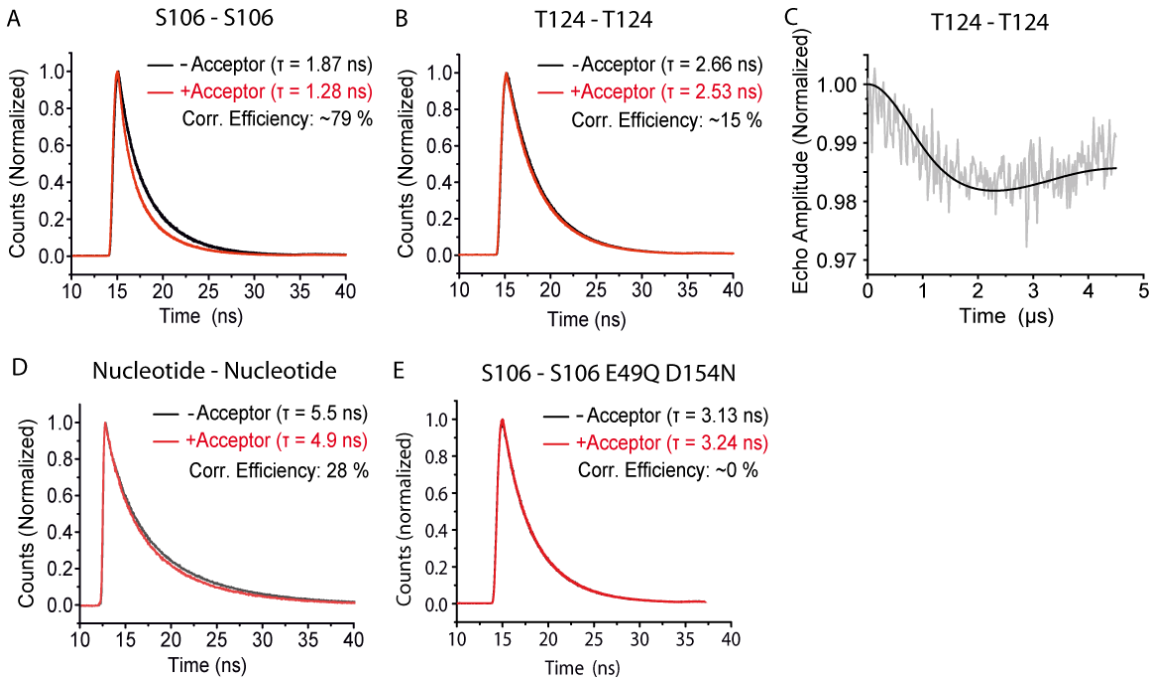


**Fig. S4: Experimental FRET and EPR measurements.** The time-correlated single photon counting (TCSPC) histograms of membrane-bound N-Ras-GDP S106-Atto532 (**A**) and T124-Atto532 C118S (**B**) with (red) and without (black) the acceptors N-Ras-GDP S106-Atto655 or T124-Atto655 C118S are shown. **C** shows the normalized experimental EPR (DEER) data for membrane-bound N-Ras-GDP T124-Proxyl. **D** displays the TCSPC histogram of membrane-bound N-Ras with the fluorescent nucleotide MANT-GDP in presence (red) and in absence of the acceptor N-Ras (TNP-GDP; black), which was published previously by Güldenhaupt et al.[1] **E** shows the TCSPC histogram of membrane bound N-Ras-GDP S106-Atto532 with (red) and without (black) the acceptors N-Ras-GDP S106-Atto655 of the E49Q D154N double mutant. The presence of the acceptor leads to a decrease in the lifetimes of the donors due to FRET. Histograms were normalized.

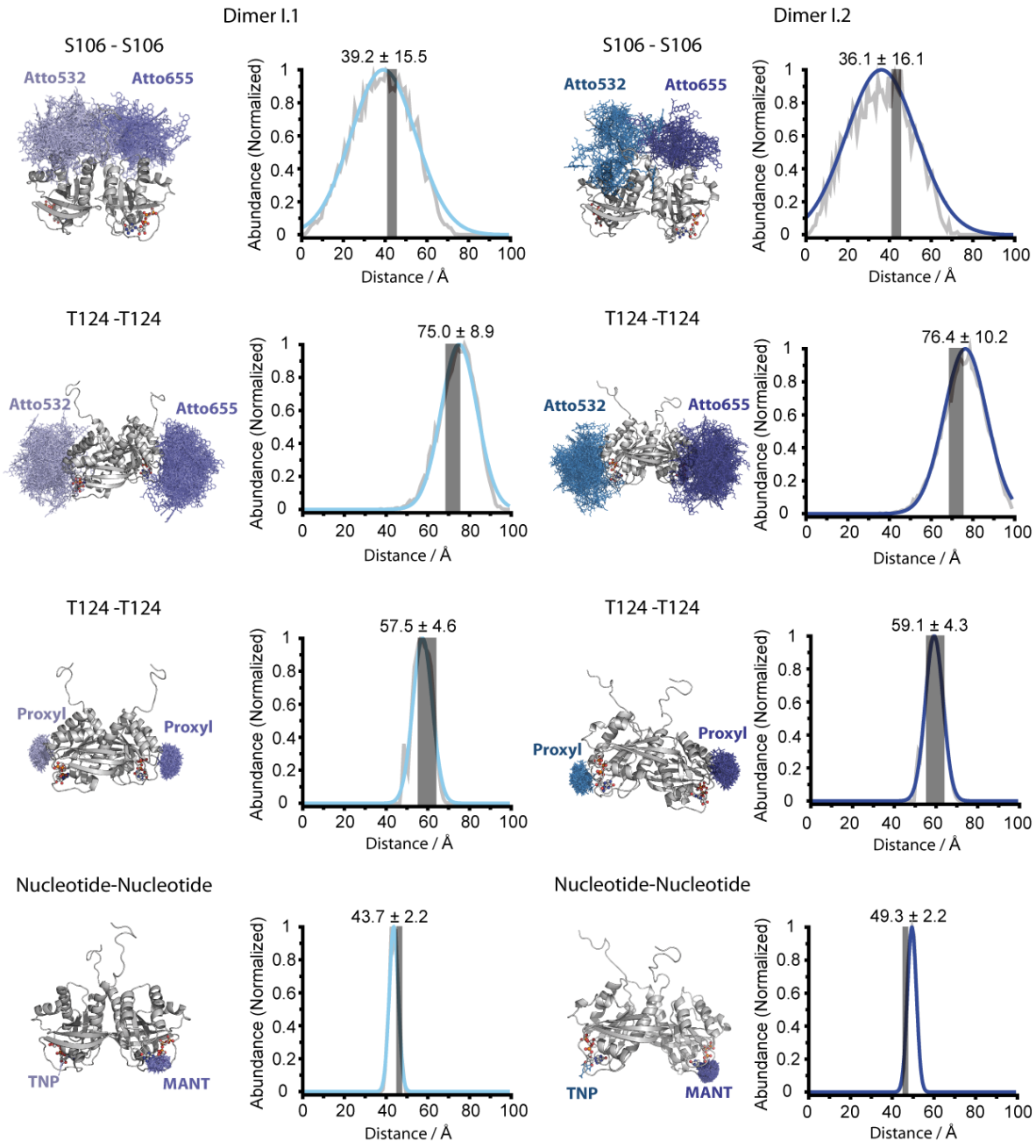
Dimer I.1
Dimer I.2
S106 - S106
Atto532
Atto655
39.2 ± 15.5
36.1 ± 16.1
T124 -T124
75.0 ± 8.9
76.4 ± 10.2
Proxyl
57.5 ± 4.6
59.1 ± 4.3
Nucleotide-Nucleotide
TNP
MANT
43.7 ± 2.2
49.3 ± 2.2
Abundance (Normalized)
Distance / Å

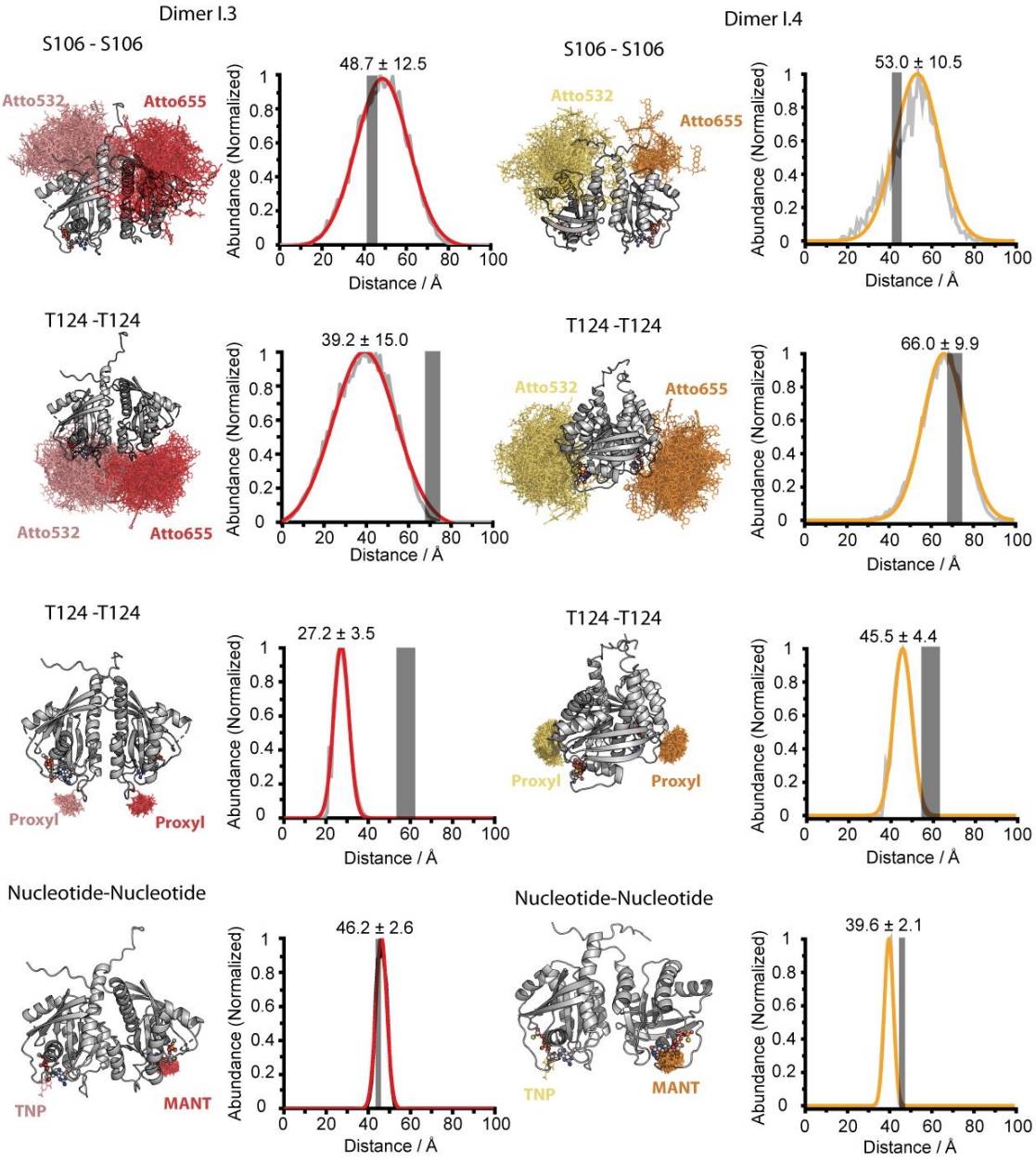
Dimer I.3
S106 - S106
Atto532
Atto655
48.7 ± 12.5
Abundance (Normalized)
Distance / Å
Dimer I.4
S106 - S106
Atto532
Atto655
53.0 ± 10.5
Abundance (Normalized)
Distance / Å
T124 -T124
Atto532
Atto655
39.2 ± 15.0
Abundance (Normalized)
Distance / Å
T124 -T124
Atto532
Atto655
66.0 ± 9.9
Abundance (Normalized)
Distance / Å
T124 -T124
Proxyl
Proxyl
27.2 ± 3.5
Abundance (Normalized)
Distance / Å
T124 -T124
Proxyl
Proxyl
45.5 ± 4.4
Abundance (Normalized)
Distance / Å
Nucleotide-Nucleotide
TNP
MANT
46.2 ± 2.6
Abundance (Normalized)
Distance / Å
Nucleotide-Nucleotide
TNP
MANT
39.6 ± 2.1
Abundance (Normalized)
Distance / Å

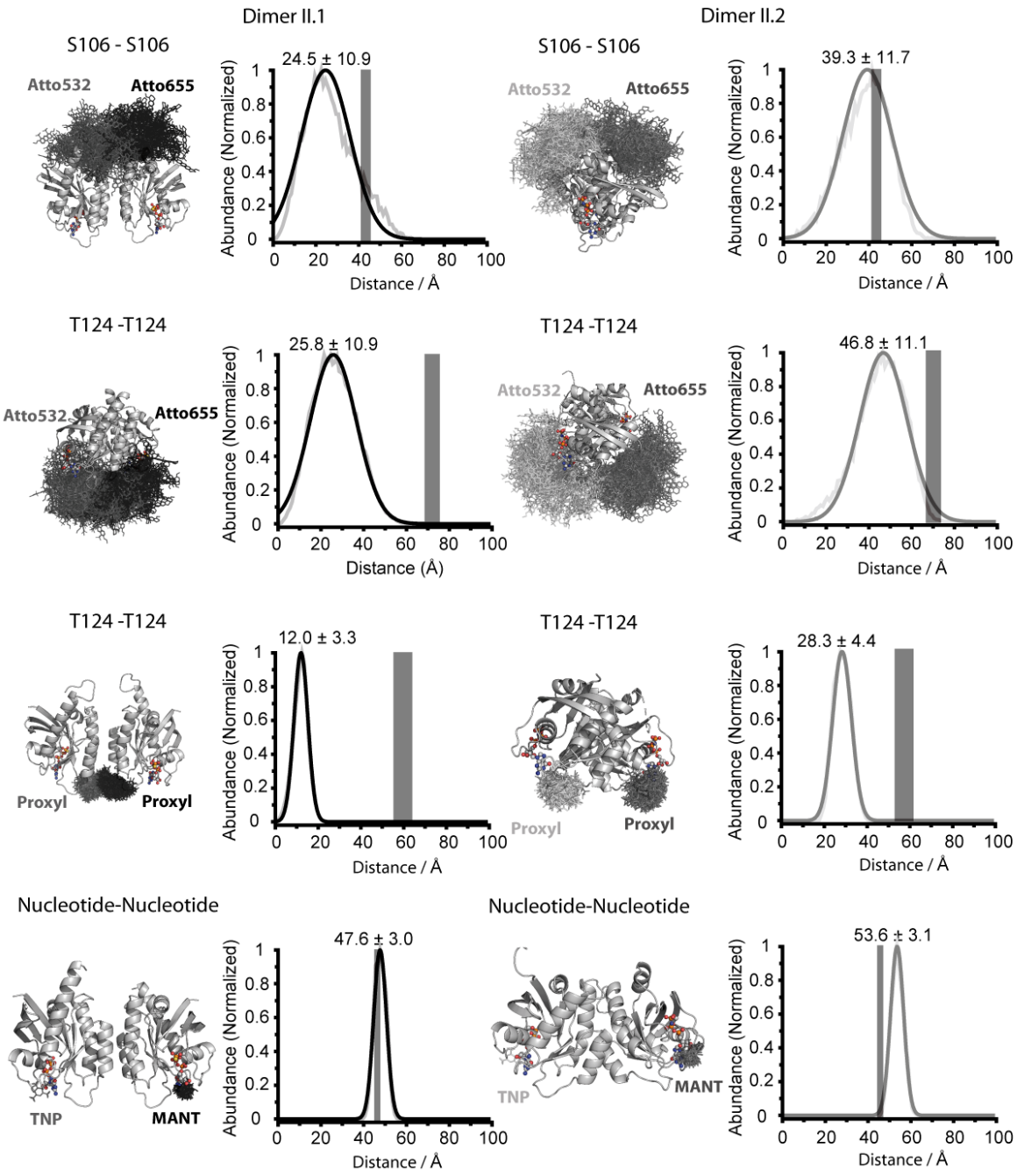
Dimer II.1
Dimer II.2
S106 - S106
Atto532
Atto655
24.5 ± 10.9
39.3 ± 11.7
T124 -T124
25.8 ± 10.9
46.8 ± 11.1
Proxyl
12.0 ± 3.3
28.3 ± 4.4
Nucleotide-Nucleotide
TNP
MANT
47.6 ± 3.0
53.6 ± 3.1
Abundance (Normalized)
Distance / Å
Distance (Å)

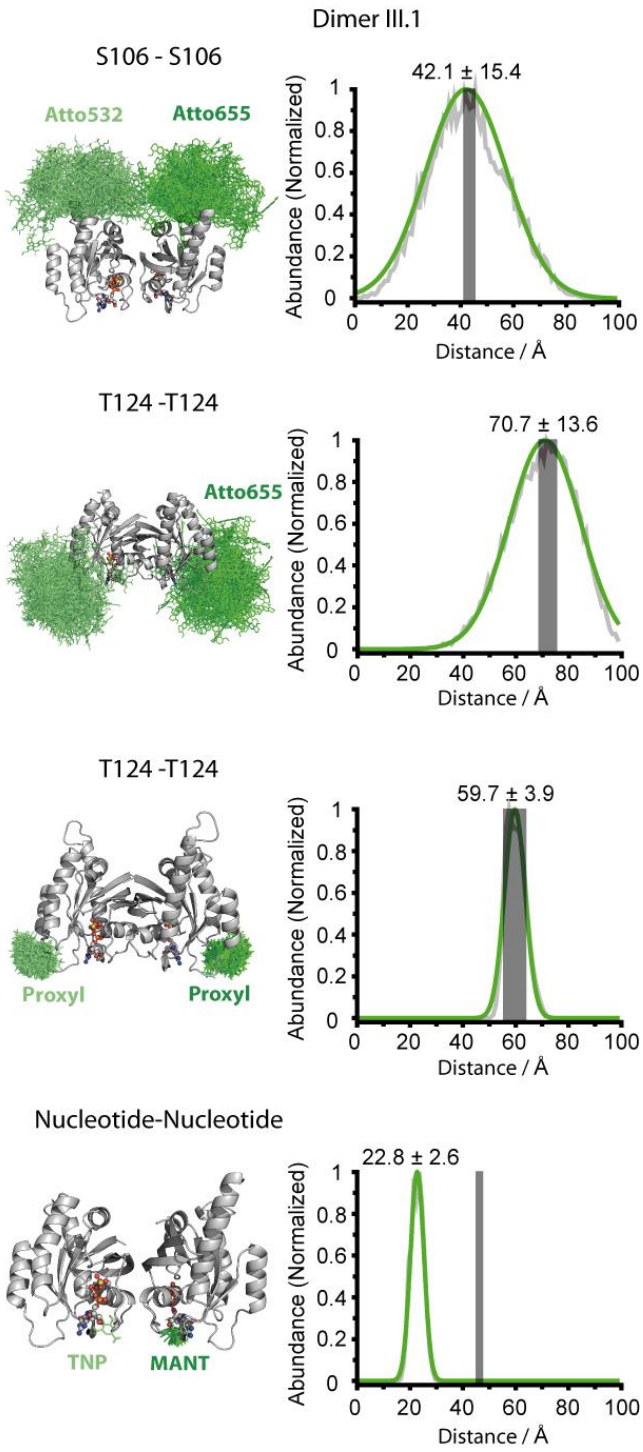


**Fig. S5: Calculated distance distributions between protein-bound fluorophores of published possible dimer structural models.** The FRET-pair Atto532/Atto655 was superimposed on the backbone of residues S106 and T124, the FRET-pair Mant-/TNP-Ribose on the ribose group of the nucleotide GDP. The EPR spin label proxyl was superimposed on the backbone of T124. The tool mtsslWizard[21] generated conformational ensembles and calculated the corresponding distance distributions between them for S106-S106, T124-T124 and nucleotide-nucleotide. A gaussian fit of the data gives the mean values of the distributions.

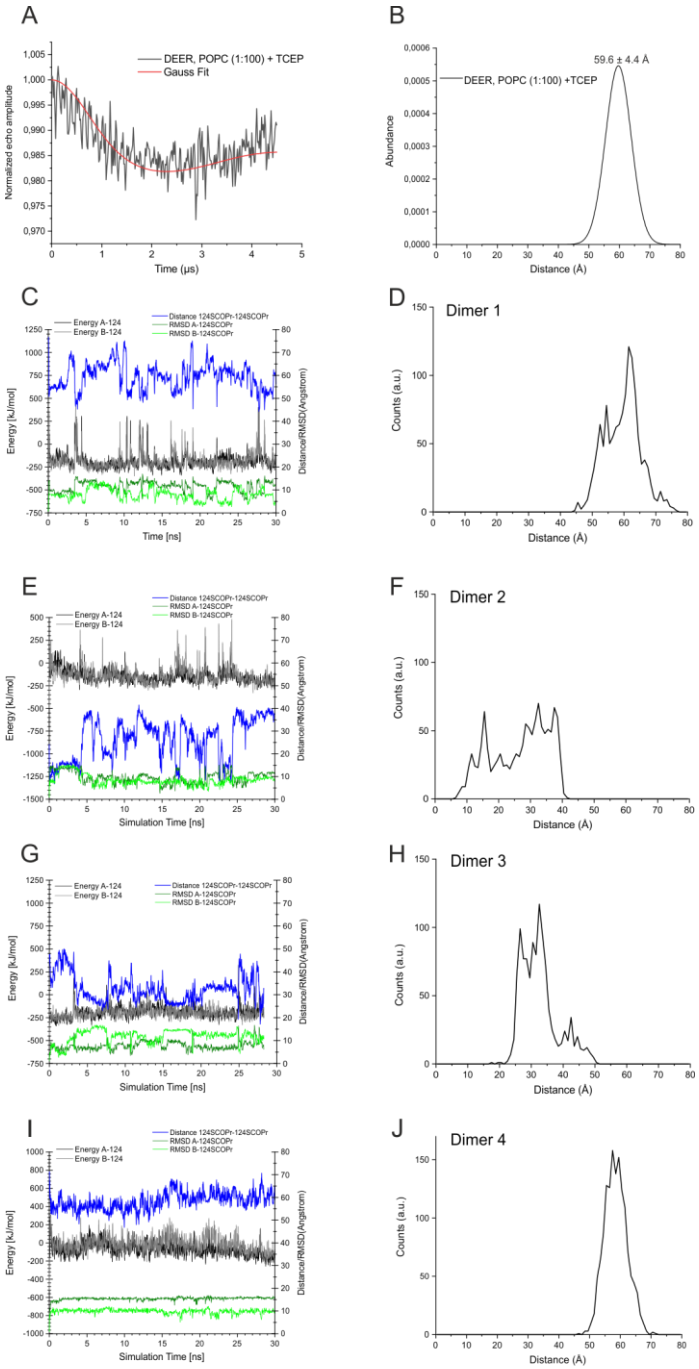


**Fig. S6: Experimental EPR data and theoretical distance distributions obtained by MD simulations. A** shows the experimental DEER data that were described by a Gauss Fit (red line). **B** displays the resulting distance distribution with a main peak at 59.7 ± 2.5 Å. **C**, **E**, **G** and **I** show the analysis of the MD simulations, that were performed in order to get theoretical distance distributions between two EPR spin labels (Proxyl) attached to one of the four dimer structure models at position 124. **D**, **F**, **H** and **J** display the theoretical distance distributions that were obtained by MD simulations. Only dimer structure models 1 and 4 are in line with the experimental EPR result.

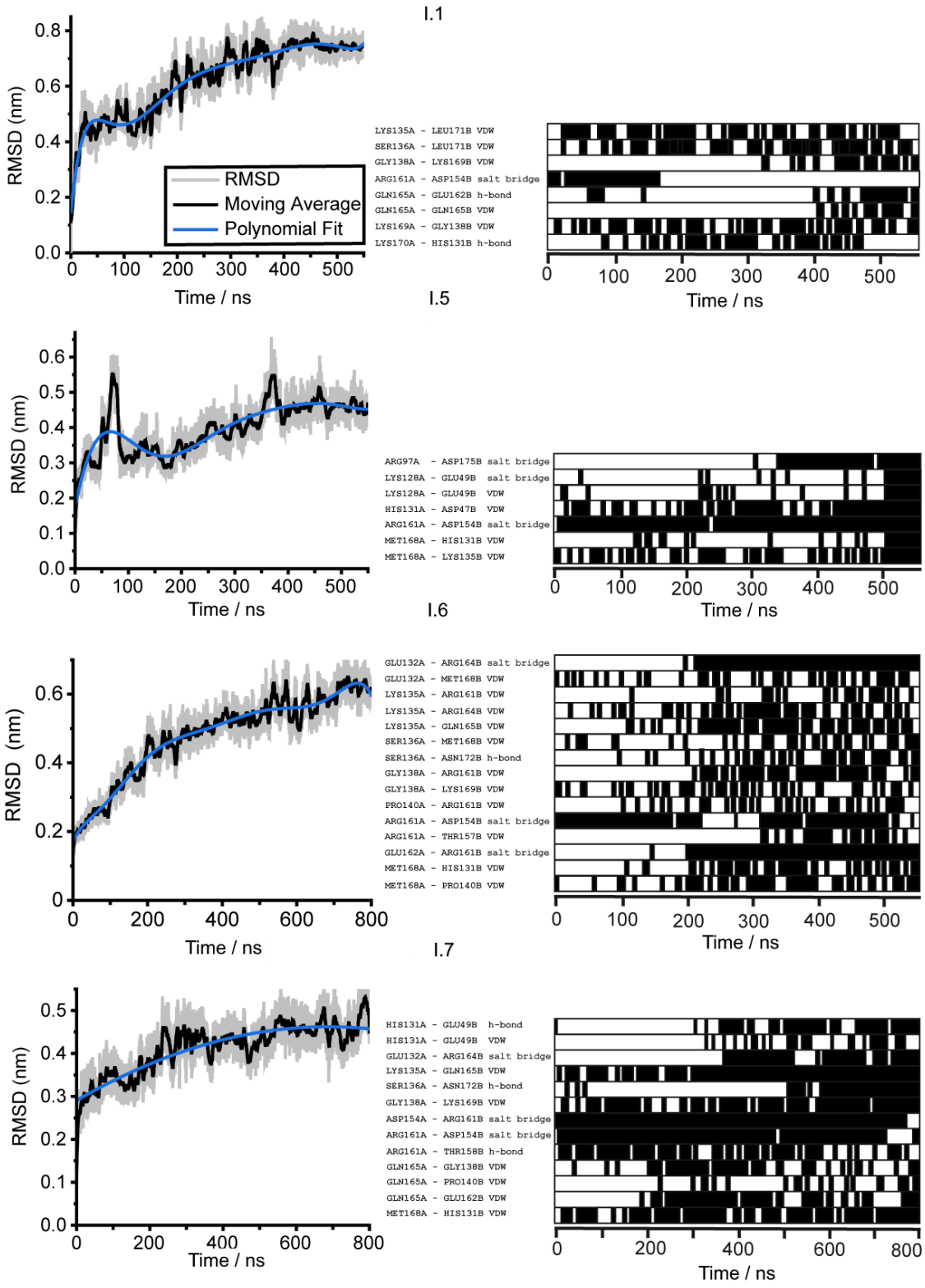
I.1
RMSD (nm)
Time / ns
RMSD
Moving Average
Polynomial Fit
LYS135A - LEU171B VDW
SER136A - LEU171B VDW
GLY138A - LYS169B VDW
ARG161A - ASP154B salt bridge
GLN165A - GLU162B h-bond
GLN165A - GLN165B VDW
LYS169A - GLY138B VDW
LYS170A - HIS131B h-bond
I.5
ARG97A - ASP175B salt bridge
LYS128A - GLU49B salt bridge
LYS128A - GLU49B VDW
HIS131A - ASP47B VDW
ARG161A - ASP154B salt bridge
MET168A - HIS131B VDW
MET168A - LYS135B VDW
I.6
GLU132A - ARG164B salt bridge
GLU132A - MET168B VDW
LYS135A - ARG161B VDW
LYS135A - ARG164B VDW
LYS135A - GLN165B VDW
SER136A - MET168B VDW
SER136A - ASN172B h-bond
GLY138A - ARG161B VDW
GLY138A - LYS169B VDW
PRO140A - ARG161B VDW
ARG161A - ASP154B salt bridge
ARG161A - THR157B VDW
GLU162A - ARG161B salt bridge
MET168A - HIS131B VDW
MET168A - PRO140B VDW
I.7
HIS131A - GLU49B h-bond
HIS131A - GLU49B VDW
GLU132A - ARG164B salt bridge
LYS135A - GLN165B VDW
SER136A - ASN172B h-bond
GLY138A - LYS169B VDW
ASP154A - ARG161B salt bridge
ARG161A - ASP154B salt bridge
ARG161A - THR158B h-bond
GLN165A - GLY138B VDW
GLN165A - PRO140B VDW
GLN165A - GLU162B VDW
MET168A - HIS131B VDW

I.8

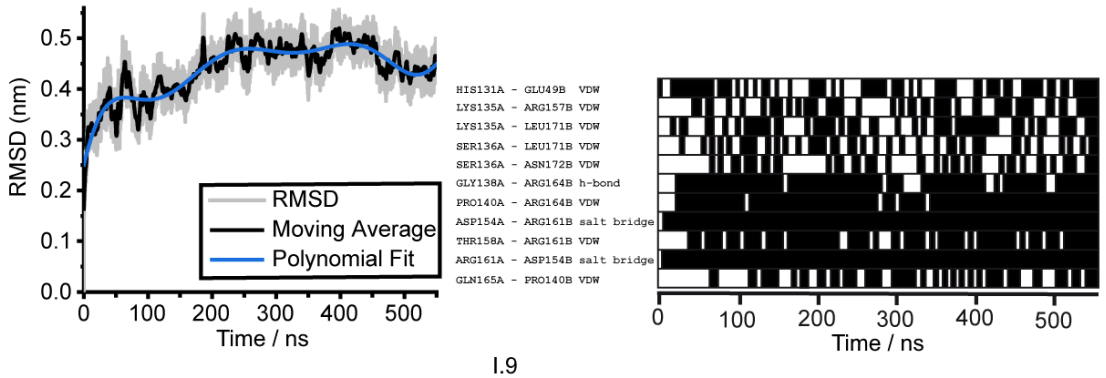
RMSD (nm)
Time / ns
RMSD
Moving Average
Polynomial Fit
HIS131A - GLU49B VDW
LYS135A - ARG157B VDW
LYS135A - LEU171B VDW
SER136A - LEU171B VDW
SER136A - ASN172B VDW
GLY138A - ARG164B h-bond
PRO140A - ARG164B VDW
ASP154A - ARG161B salt bridge
THR158A - ARG161B VDW
ARG161A - ASP154B salt bridge
GLN165A - PRO140B VDW

I.9

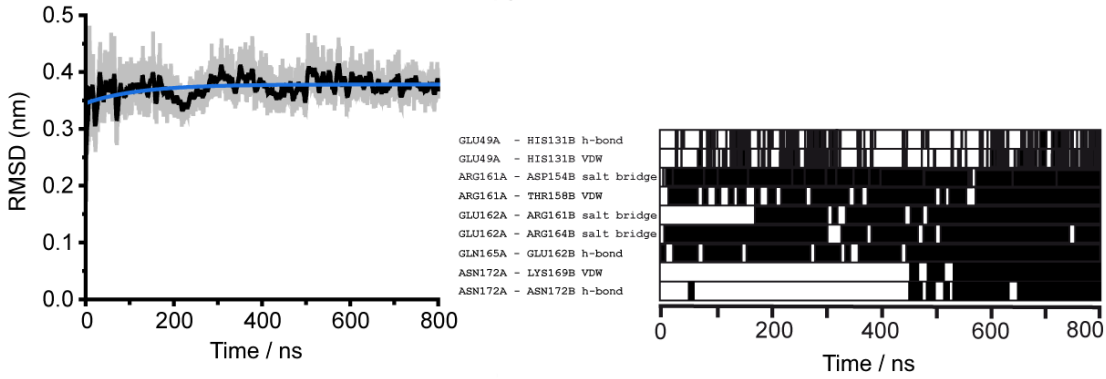
RMSD (nm)
Time / ns
GLU49A - HIS131B h-bond
GLU49A - HIS131B VDW
ARG161A - ASP154B salt bridge
ARG161A - THR158B VDW
GLU162A - ARG161B salt bridge
GLU162A - ARG164B salt bridge
GLN165A - GLU162B h-bond
ASN172A - LYS169B VDW
ASN172A - ASN172B h-bond

I.10

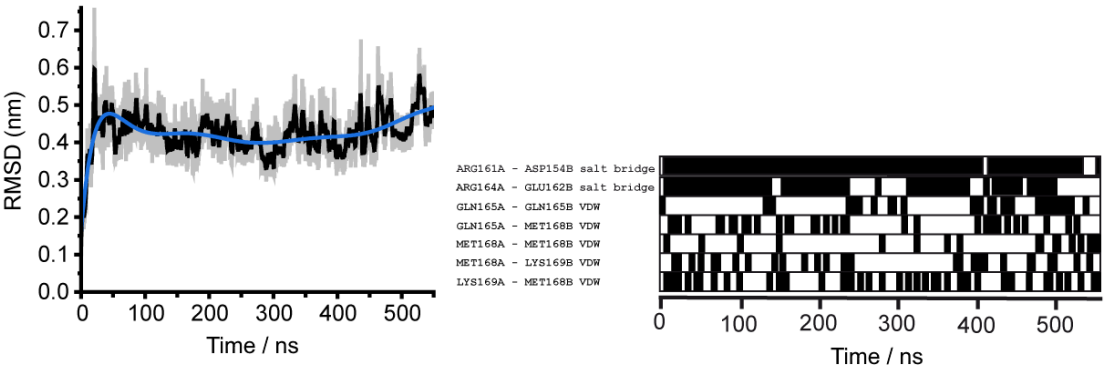
RMSD (nm)
Time / ns
ARG161A - ASP154B salt bridge
ARG164A - GLU162B salt bridge
GLN165A - GLN165B VDW
GLN165A - MET168B VDW
MET168A - MET168B VDW
MET168A - LYS169B VDW
LYS169A - MET168B VDW

I.11

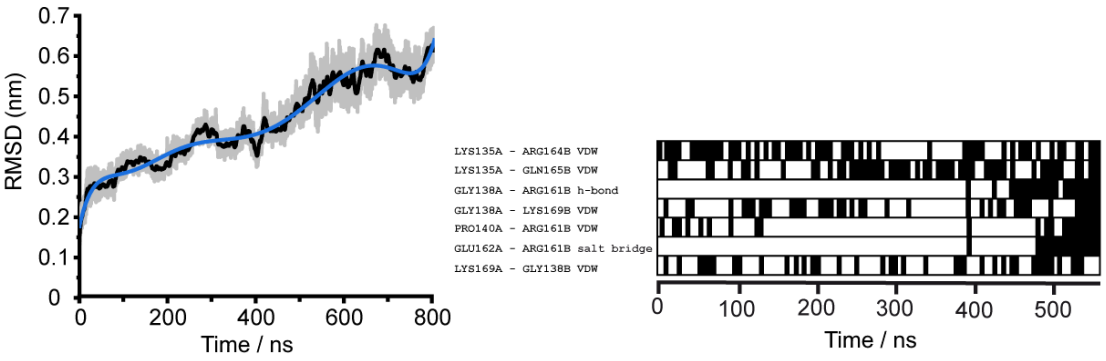
RMSD (nm)
Time / ns
LYS135A - ARG164B VDW
LYS135A - GLN165B VDW
GLY138A - ARG161B h-bond
GLY138A - LYS169B VDW
PRO140A - ARG161B VDW
GLU162A - ARG161B salt bridge
LYS169A - GLY138B VDW

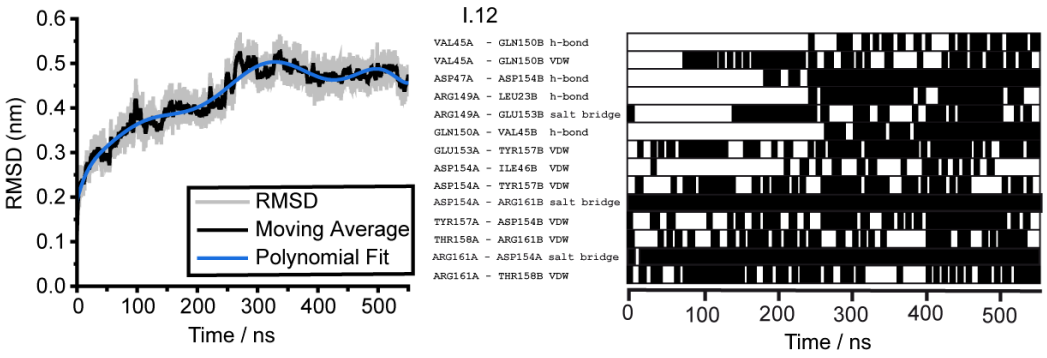


**Fig. S7: RMSD and intermolecular contact interface for the Ras dimer simulations (see Table S3-S5).** On the left, the RMSD of the Cα atoms for the Ras residues 1-172 is shown (gray). A moving average (black) displays the short-term and a polynomial fit (blue) the long-term trend of the RMSD. Shown on the right, is the dynamic contact interface between the two Ras monomers. A black bar represents an existing contact.

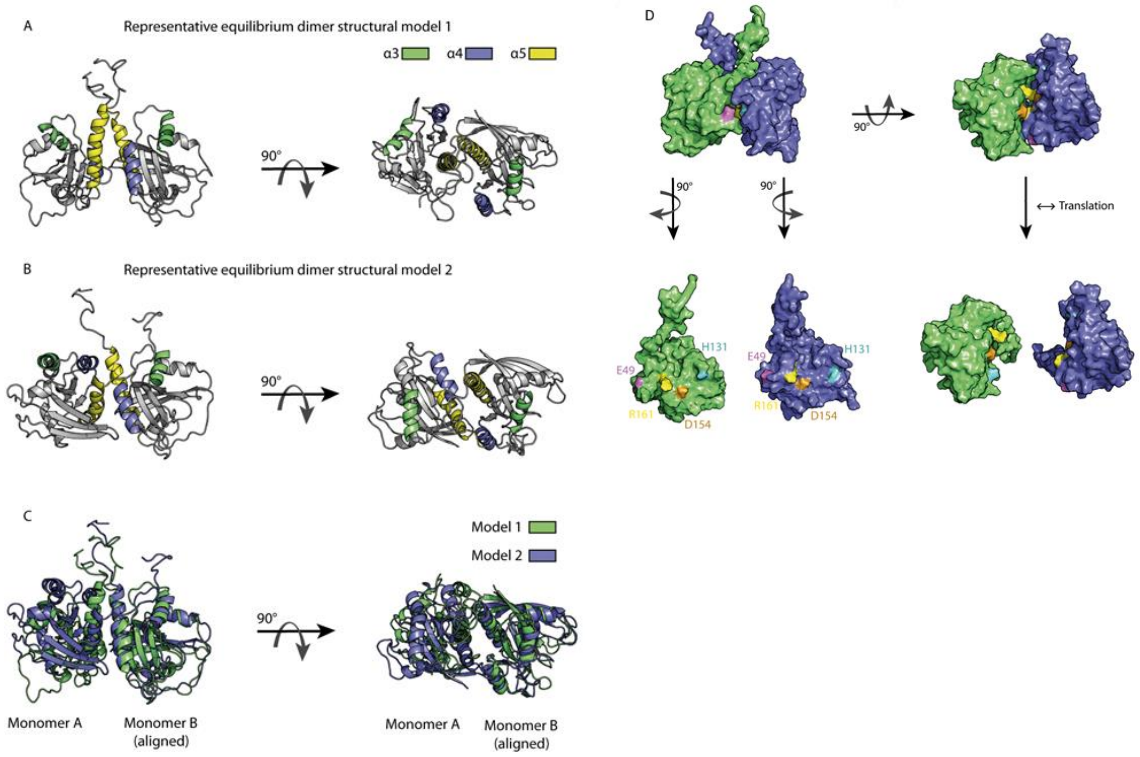


**Fig. S8: Representative equilibrium dimer structural models of the lipidated N-Ras dimer simulations. A** shows the representative structural model 1 of simulations I.9 and I.10 (see Table S3, S7 and S8), which is in accordance with all experimental values. **B** displays the representative structural model 2 of the other seven simulations (see Table S3, S7 and S8). The helices α3- α5 in **A** and **B** are color coded: Helix α3 (green), helix α4 (blue), helix α5 (yellow). In **C** Monomer B of the representative structural models is aligned to clarify their differences. Model 1 is shown in green, while model 2 is shown in blue. Shown in **D** is the surface of the representative dimer structural model 1. The identified central key interface amino acids R161 (yellow), D154 (orange), E49 (purple) and H131 (cyan) are highlighted. The top left shows the side view of the Ras dimer and the top right the bottom view (rotated by 90 degrees). In the lower left the dimer is folded apart to show the central positions of the key contacts. The bottom right illustrates that the contact surface of the dimer is flat.

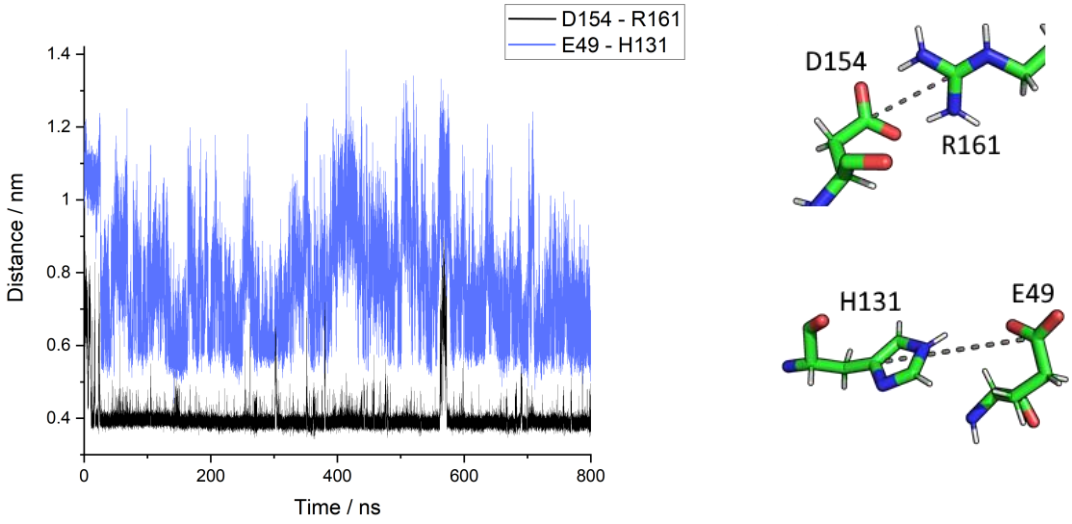


**Fig. S9: Distance plot for the most important contact residues of simulation I.9.** The distances were measured between CG and CZ for D154-R161, as well as CD and CG for E49-H131 to calculate the distance independent of the side chain rotation. The D154-R161 contact is extremely stable, while the E49-H131 contact is fluctuating due to competing interactions.

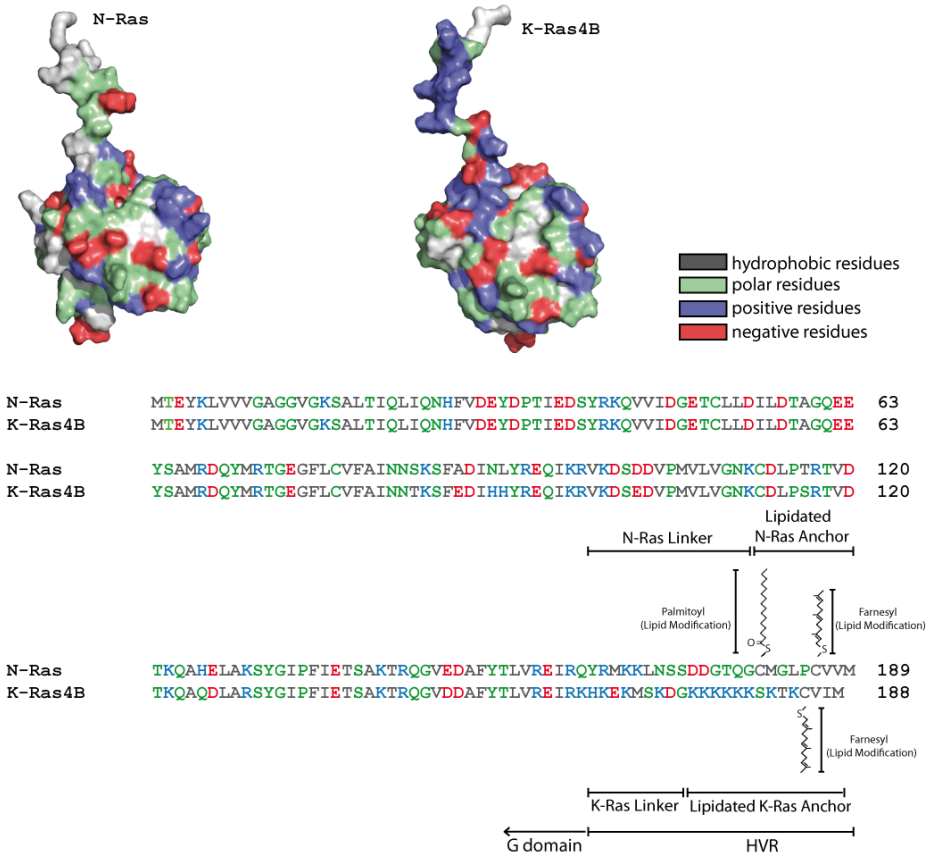


**Fig. S10: Comparison of the surface localisation of hydrophobic, polar and charged residues between N-Ras and K-Ras4B.** Shown is the surface formed by helices α4 and α5, as well as a sequence alignment with color coded residues (hydrophobic residues: gray, polar residues: green, positively charged residues: blue, negatively charged residues: red).

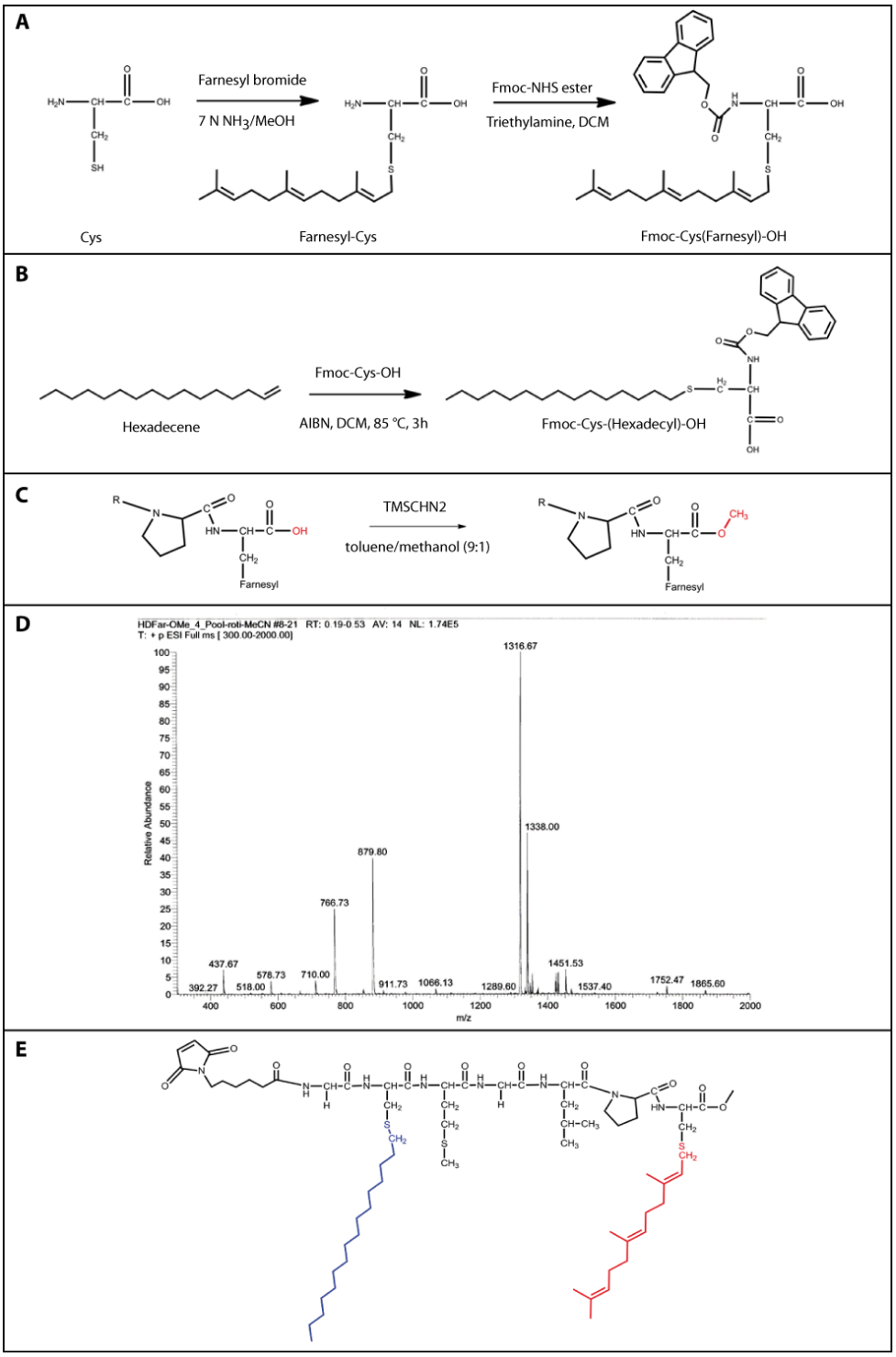


**Figure S11: Lipid anchor synthesis for N-Ras.** In **A** the coupling of cysteine with farnesyl bromide, which results in Fmoc-Cys(Farnesyl)-OH is shown. The radical reaction of hexadecane with Fmoc-Cys-OH, yielding Fmoc-Cys(Hexadecyl)-OH is shown in **B**. The last synthesis step was the methylation of the terminal carboxylic acid of the cysteine with trimethylsilyldiazomethane, which is displayed in **C**. The ESI-MS spectrum of the final product is shown in **D**. The complete structure of the synthesized peptide Maleimidocaproyl-Gly-Cys(Hexadecyl)-Met-Gly-Leu-Pro-Cys(Farnesyl)-OMethyl is shown in **E**. The Hexadecyl-moiety is labeled in blue and the Farnesyl-anchor in red.

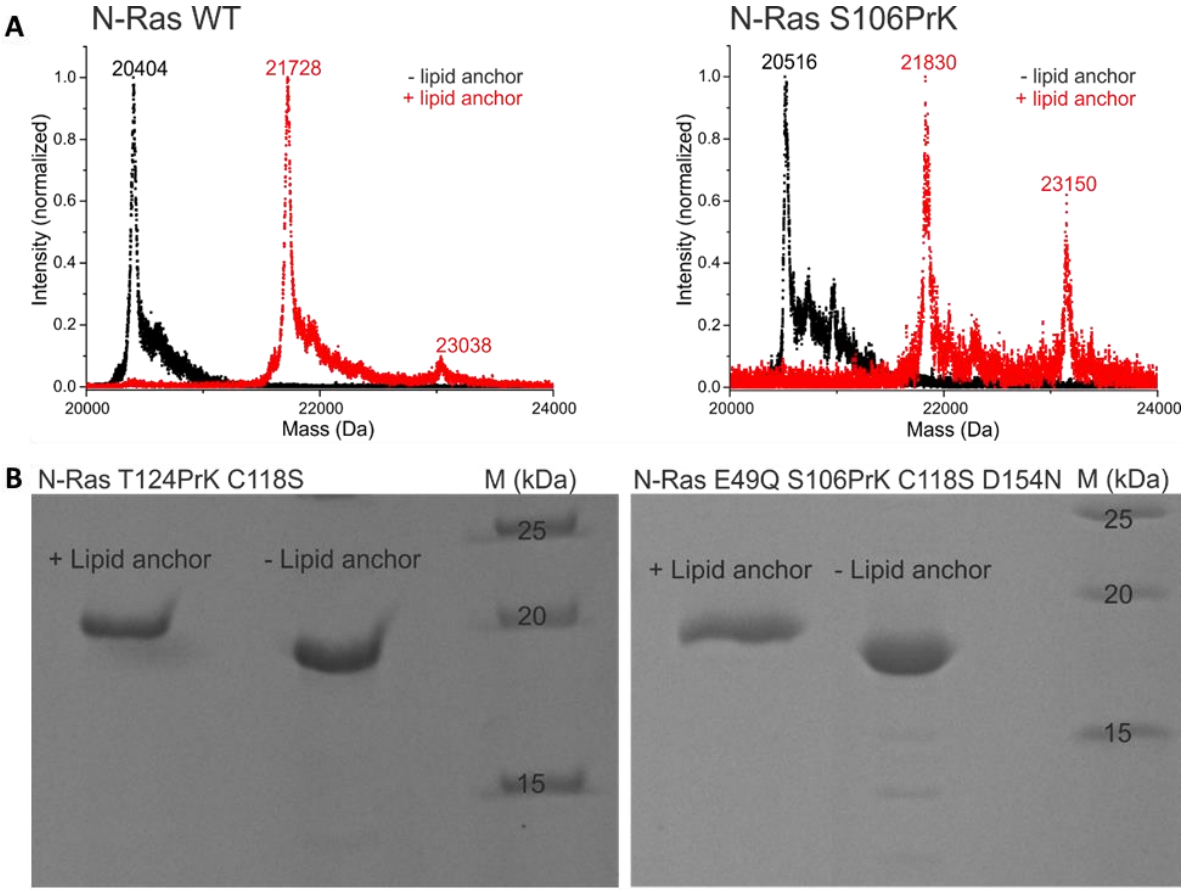


**Fig. S12: N-Ras lipidation**. In **A** the MADLI-MS results measured before and after N-Ras lipidation are shown. The lipid anchor exhibits a molecular mass of 1316 Da. For the wildtype, a mass difference of 1324 Da was observed after lipid coupling. For the N-Ras mutant S106PrK, a mass difference of 1314 Da was measured after lipid coupling. In **B** the SDS-PAGE gels for N-Ras T124PrK C118S and N-Ras E49Q S106PrK C118S D154N before and after lipid coupling are shown. A mass difference is observable due to the lipidation.

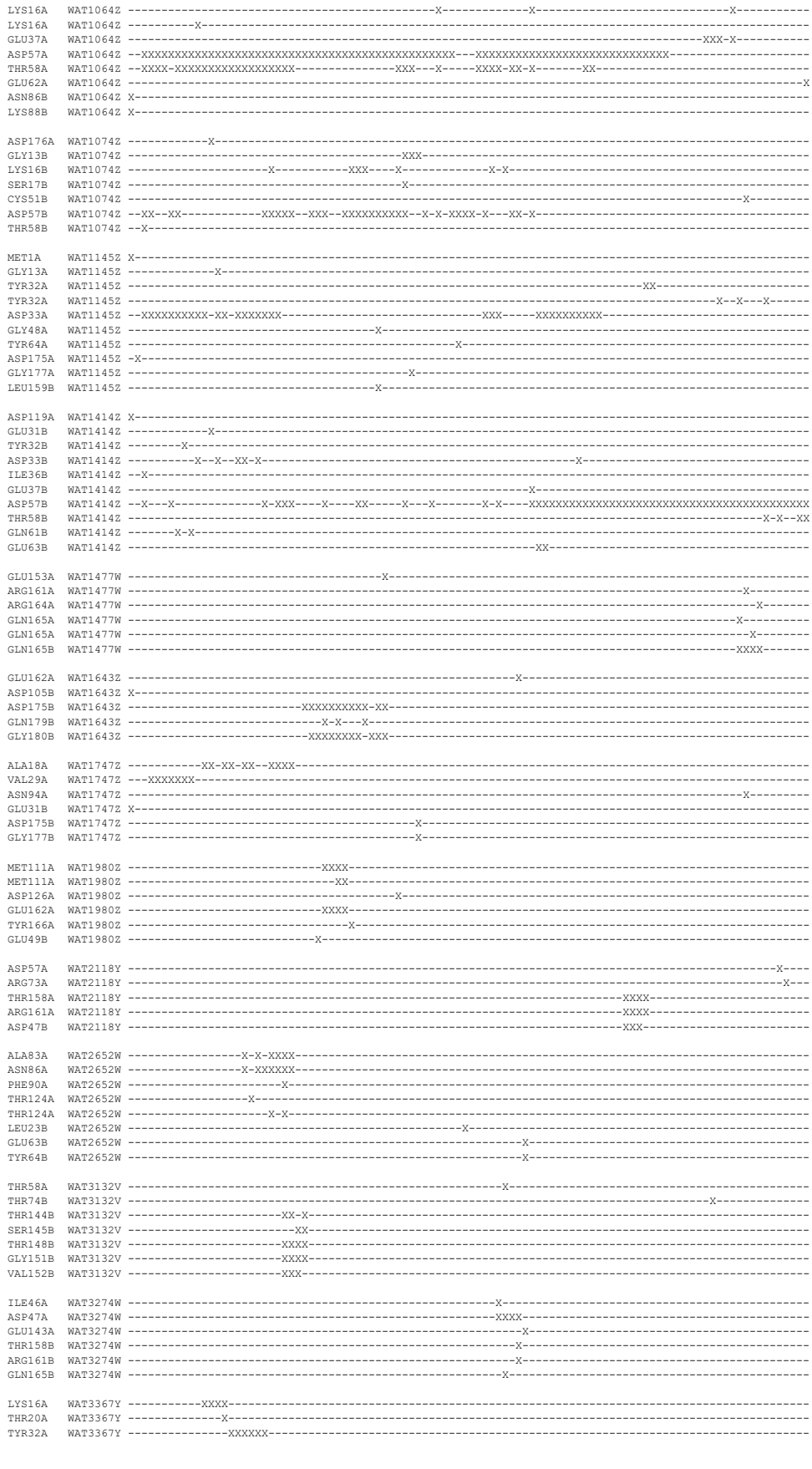
LYS16A WAT1064Z
LYS16A WAT1064Z
GLU37A WAT1064Z
ASP57A WAT1064Z
THR58A WAT1064Z
GLU62A WAT1064Z
ASN86B WAT1064Z
LYS88B WAT1064Z
ASP176A WAT1074Z
GLY13B WAT1074Z
LYS16B WAT1074Z
SER17B WAT1074Z
CYS51B WAT1074Z
ASP57B WAT1074Z
THR58B WAT1074Z
MET1A WAT1145Z
GLY13A WAT1145Z
TYR32A WAT1145Z
TYR32A WAT1145Z
ASP33A WAT1145Z
GLY48A WAT1145Z
TYR64A WAT1145Z
ASP175A WAT1145Z
GLY177A WAT1145Z
LEU159B WAT1145Z
ASP119A WAT1414Z
GLU31B WAT1414Z
TYR32B WAT1414Z
ASP33B WAT1414Z
ILE36B WAT1414Z
GLU37B WAT1414Z
ASP57B WAT1414Z
THR58B WAT1414Z
GLN61B WAT1414Z
GLU63B WAT1414Z
GLU153A WAT1477W
ARG161A WAT1477W
ARG164A WAT1477W
GLN165A WAT1477W
GLN165A WAT1477W
GLN165B WAT1477W
GLU162A WAT1643Z
ASP105B WAT1643Z
ASP175B WAT1643Z
GLN179B WAT1643Z
GLY180B WAT1643Z
ALA18A WAT1747Z
VAL29A WAT1747Z
ASN94A WAT1747Z
GLU31B WAT1747Z
ASP175B WAT1747Z
GLY177B WAT1747Z
MET111A WAT1980Z
MET111A WAT1980Z
ASP126A WAT1980Z
GLU162A WAT1980Z
TYR166A WAT1980Z
GLU49B WAT1980Z
ASP57A WAT2118Y
ARG73A WAT2118Y
THR158A WAT2118Y
ARG161A WAT2118Y
ASP47B WAT2118Y
ALA83A WAT2652W
ASN86A WAT2652W
PHE90A WAT2652W
THR124A WAT2652W
THR124A WAT2652W
LEU23B WAT2652W
GLU63B WAT2652W
TYR64B WAT2652W
THR58A WAT3132V
THR74B WAT3132V
THR144B WAT3132V
SER145B WAT3132V
THR148B WAT3132V
GLY151B WAT3132V
VAL152B WAT3132V
ILE46A WAT3274W
ASP47A WAT3274W
GLU143A WAT3274W
THR158B WAT3274W
ARG161B WAT3274W
GLN165B WAT3274W
LYS16A WAT3367Y
THR20A WAT3367Y
TYR32A WAT3367Y

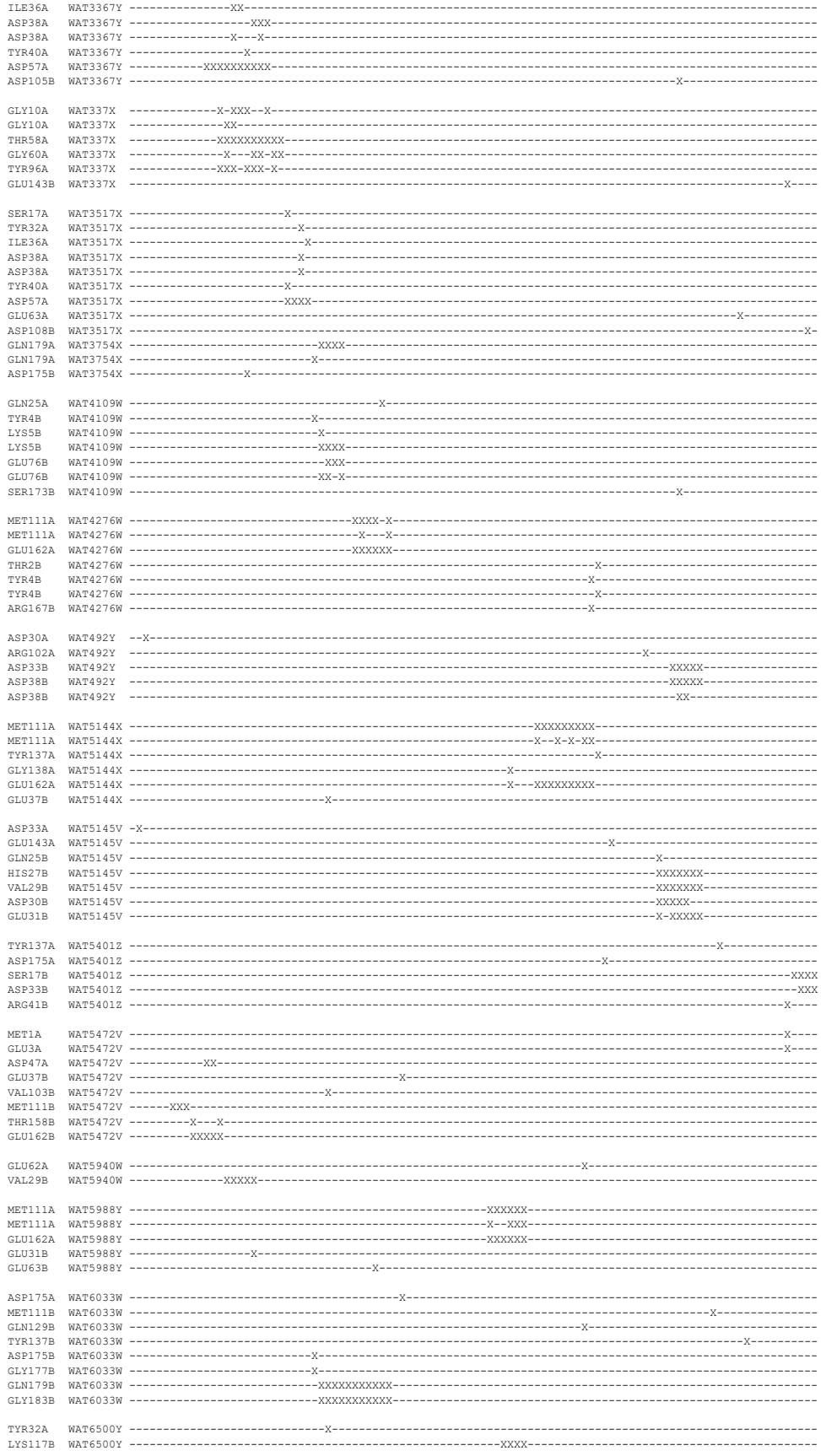
ILE36A WAT3367Y
ASP38A WAT3367Y
ASP38A WAT3367Y
TYR40A WAT3367Y
ASP57A WAT3367Y
ASP105B WAT3367Y
GLY10A WAT337X
GLY10A WAT337X
THR58A WAT337X
GLY60A WAT337X
TYR96A WAT337X
GLU143B WAT337X
SER17A WAT3517X
TYR32A WAT3517X
ILE36A WAT3517X
ASP38A WAT3517X
ASP38A WAT3517X
TYR40A WAT3517X
ASP57A WAT3517X
GLU63A WAT3517X
ASP108B WAT3517X
GLN179A WAT3754X
GLN179A WAT3754X
ASP175B WAT3754X
GLN25A WAT4109W
TYR4B WAT4109W
LYS5B WAT4109W
LYS5B WAT4109W
GLU76B WAT4109W
GLU76B WAT4109W
SER173B WAT4109W
MET111A WAT4276W
MET111A WAT4276W
GLU162A WAT4276W
THR2B WAT4276W
TYR4B WAT4276W
TYR4B WAT4276W
ARG167B WAT4276W
ASP30A WAT492Y
ARG102A WAT492Y
ASP33B WAT492Y
ASP38B WAT492Y
ASP38B WAT492Y
MET111A WAT5144X
MET111A WAT5144X
TYR137A WAT5144X
GLY138A WAT5144X
GLU162A WAT5144X
GLU37B WAT5144X
ASP33A WAT5145V
GLU143A WAT5145V
GLN25B WAT5145V
HIS27B WAT5145V
VAL29B WAT5145V
ASP30B WAT5145V
GLU31B WAT5145V
TYR137A WAT5401Z
ASP175A WAT5401Z
SER17B WAT5401Z
ASP33B WAT5401Z
ARG41B WAT5401Z
MET1A WAT5472V
GLU3A WAT5472V
ASP47A WAT5472V
GLU37B WAT5472V
VAL103B WAT5472V
MET111B WAT5472V
THR158B WAT5472V
GLU162B WAT5472V
GLU62A WAT5940W
VAL29B WAT5940W
MET111A WAT5988Y
MET111A WAT5988Y
GLU162A WAT5988Y
GLU31B WAT5988Y
GLU63B WAT5988Y
ASP175A WAT6033W
MET111B WAT6033W
GLN129B WAT6033W
TYR137B WAT6033W
ASP175B WAT6033W
GLY177B WAT6033W
GLN179B WAT6033W
GLY183B WAT6033W
TYR32A WAT6500Y
LYS117B WAT6500Y

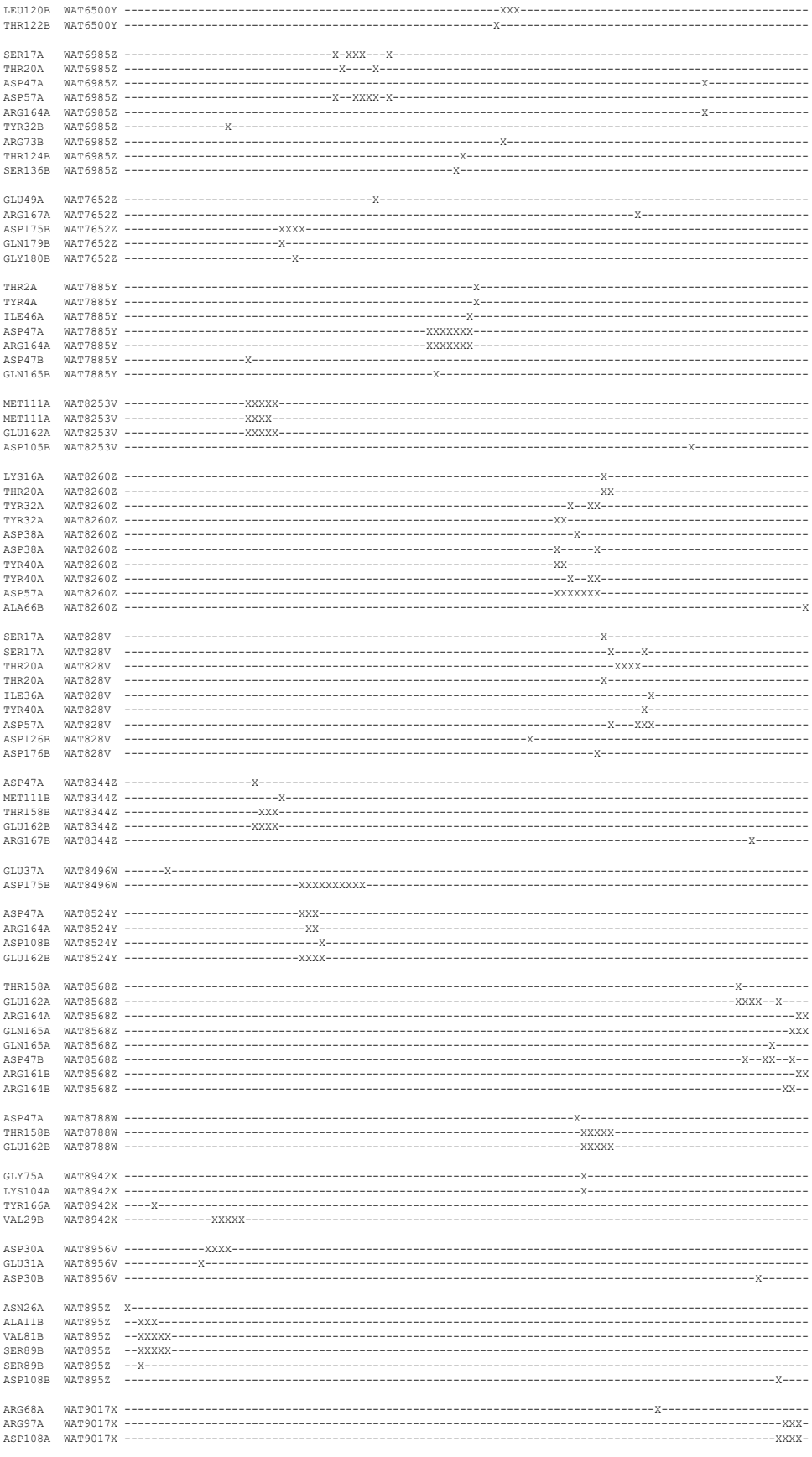
LEU120B WAT6500Y
THR122B WAT6500Y
SER17A WAT6985Z
THR20A WAT6985Z
ASP47A WAT6985Z
ASP57A WAT6985Z
ARG164A WAT6985Z
TYR32B WAT6985Z
ARG73B WAT6985Z
THR124B WAT6985Z
SER136B WAT6985Z
GLU49A WAT7652Z
ARG167A WAT7652Z
ASP175B WAT7652Z
GLN179B WAT7652Z
GLY180B WAT7652Z
THR2A WAT7885Y
TYR4A WAT7885Y
ILE46A WAT7885Y
ASP47A WAT7885Y
ARG164A WAT7885Y
ASP47B WAT7885Y
GLN165B WAT7885Y
MET111A WAT8253V
MET111A WAT8253V
GLU162A WAT8253V
ASP105B WAT8253V
LYS16A WAT8260Z
THR20A WAT8260Z
TYR32A WAT8260Z
TYR32A WAT8260Z
ASP38A WAT8260Z
ASP38A WAT8260Z
TYR40A WAT8260Z
TYR40A WAT8260Z
ASP57A WAT8260Z
ALA66B WAT8260Z
SER17A WAT828V
SER17A WAT828V
THR20A WAT828V
THR20A WAT828V
ILE36A WAT828V
TYR40A WAT828V
ASP57A WAT828V
ASP126B WAT828V
ASP176B WAT828V
ASP47A WAT8344Z
MET111B WAT8344Z
THR158B WAT8344Z
GLU162B WAT8344Z
ARG167B WAT8344Z
GLU37A WAT8496W
ASP175B WAT8496W
ASP47A WAT8524Y
ARG164A WAT8524Y
ASP108B WAT8524Y
GLU162B WAT8524Y
THR158A WAT8568Z
GLU162A WAT8568Z
ARG164A WAT8568Z
GLN165A WAT8568Z
GLN165A WAT8568Z
ASP47B WAT8568Z
ARG161B WAT8568Z
ARG164B WAT8568Z
ASP47A WAT8788W
THR158B WAT8788W
GLU162B WAT8788W
GLY75A WAT8942X
LYS104A WAT8942X
TYR166A WAT8942X
VAL29B WAT8942X
ASP30A WAT8956V
GLU31A WAT8956V
ASP30B WAT8956V
ASN26A WAT895Z
ALA11B WAT895Z
VAL81B WAT895Z
SER89B WAT895Z
SER89B WAT895Z
ASP108B WAT895Z
ARG68A WAT9017X
ARG97A WAT9017X
ASP108A WAT9017X

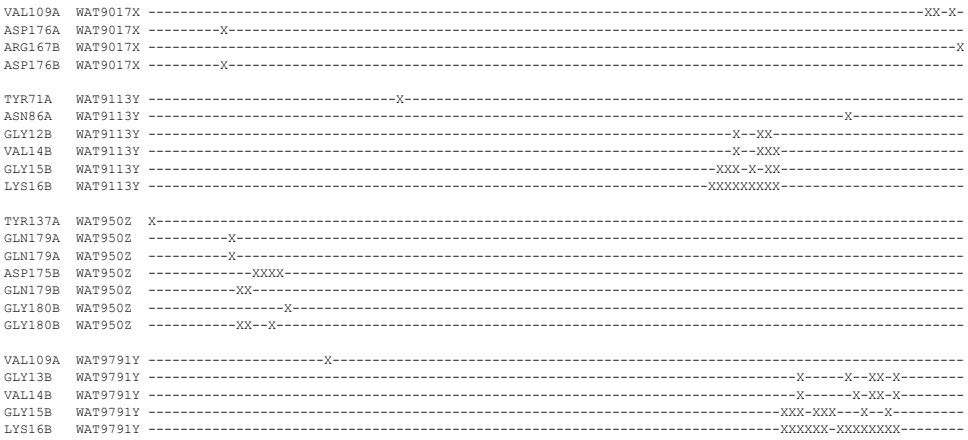


**Fig. S13: Water-Protein contact analysis for simulation I.9.** Water molecules forming a hydrogen bond to one of the two Ras proteins at any time of the simulation trajectory I.9 are shown. Every block displays the analysis for one water molecule. The first and second columns specify the residues in contact. An X represents an existing contact in this simulation frame. A simultaneous contact to both chains means that the water molecule is directly bridging the dimer interface.

## Supplementary Tables

**Table S1: Categorization of the dimer structural model obtained by protein-protein docking.**

| Category | Number | Interface |
|---|---|---|
| I | 12 | α4/α5 - α4/α5 |
| II | 6 | α3/α4 – α3/α4 |
| III | 121 | β-sheet – β-sheet |
| IV | 3 | α3/α4 - β-sheet |
| V | 3 | α4/α5 - β-sheet |
| VI | 2 | α5 - β-sheet |
| VII | 1 | α4 – α4 |
| VIII | 2 | α2/α5 – α2/α5 |
| IX | 28 | Involvement of nucleotide Binding pocket |
| Total | 178 | |

**Table S2: FRET and EPR results.** The table shows the obtained donor's lifetimes with and without the acceptor, the calculated and corrected FRET efficiencies as well as the distances between the fluorophores coupled to lipidated Ras on POPC liposomes or in solution. Displayed are mean values, the standard deviation is displayed only for the final distance. Also shown is the result of the EPR measurements and the FRET GDP-GDP distance published by Güldenhaupt et al.[1]

| Label | Membrane (POPC) | Lifetime without acceptor / ns | Lifetime with acceptor / ns | Corr. Efficiency | Distance (Å) |
|---|---|---|---|---|---|
| 106-Atto532-106-Atto655 | yes | 1.87 | 1.28 | ~ 79 % | 43.3 ± 2.3 |
| 124-Atto532-124-Atto655 | yes | 2.66 | 2.53 | ~ 15 % | 72.0 ± 3.5 |
| 124-Proxyl-124-Proxyl | yes | | | | 59.0 ± 2.5 |
| GDP-MANT-GDP-TNP | yes | 5.5 | 4.9 | ~ 28 % | 46.3 ± 1.4 |
| 106-Atto532-106-Atto655 | no | 1.86 | 1.41 | ~ 60 % | 49.7 ± 0.8 |
| 124-Atto532-124-Atto655 | no | 3.56 | 3.44 | ~ 10 % | 77.0 ± 0.5 |
| 106-Atto532-106-Atto655 E49Q D154N | yes | 3.13 | 3.24 | ~ 0 % | |

**Table S3: Validation of Ras dimer structural models by comparing theoretical distances with experimental values.** Given as reference are the three experimental distances, obtained by FRET experiments for the FRET fluorophore pairs S106-Atto532/S106-Atto655, T124-Atto532/T124-Atto655, GDP-MANT/GDP-TNP and the EPR label pair T124-Proxyl/T124-Proxyl taken from Fig. 3. Summarized are the mean values and the standard deviation of the gauss fit of the calculated distance distribution of the four aforementioned label for all obtained dimer structural models from protein-protein docking server (see Supporting Note 2) using the mtsslWizard[21] in PyMol as shown in Fig. S3 and described in Supporting Note 6. The agreement with the experiment is color coded in the following manner; green: the calculated mean distance is within the standard deviation of the experimental value; yellow: the calculated standard deviation is within the experimental standard deviation; red: the calculated values are not in accordance with the experiment. Based on these results, the dimer conformations I.5 to I.12 where chosen for further refinement through MD simulations. The categories are defined in the following manner based on their interaction sides, whereby categories I-III are found in the literature: **I** (contact between the surfaces formed by helices α4 and α5, **II** (contact between the surfaces formed by helices α3 and α4), **III** (contact between the surfaces formed by the beta sheets), **IV** (contact between helices α3 and α4 of one monomer with the beta sheet of the other monomer), **V** (contact between the helices α4 and α5 of one monomer with the beta sheet of the other monomer), **VI** (contact between the surfaces formed by helix α5 and the beta sheet), **VII** (contact between the surfaces formed by helices α4), **VIII** (contact between the surfaces formed by the helices α2 and α5), IX (involvement of the switch regions of at least one monomer in the dimer interface).

| Conformation | Number of Structures | Distance / Å | | | |
|---|---|---|---|---|---|
| | | S106-S106 | T124-T124 | T124-T124 Proxyl | Nucleotide - Nucleotide |
| Experimental | | 43,3 ± 2.3 | 72,0 ± 3.5 | 59.7 ± 2.5 | 46,3 ± 1,4 |
| I.1 | ref.[9] | 39,2 ± 15,5 | 75,0 ± 8,6 | 57.5 ± 4.6 | 43,7 ± 2,2 |
| I.2 | ref.[9] | 36.1 ± 16.9 | 76.4 ± 10.2 | 59.1 ± 4.3 | 49.3 ± 2.2 |
| I.3 | ref.[12] | 48.7 ± 12.5 | 39.2 ± 15.0 | 27.2 ± 3.5 | 46.2 ± 2.6 |
| I.4 | ref.[12] | 53.0 ± 10.5 | 66.0 ± 9.9 | 45.5 ± 4.4 | 39.6 ± 2.1 |
| I.5 | 1 | 28.4 ± 13.4 | 72.4 ± 10.1 | 56.2 ± 4.3 | 44.2 ± 2.5 |
| I.6 | 1 | 31.8 ± 14.6 | 76.36 ± 8.9 | 56.6 ± 4.4 | 44.99 ± 2.2 |
| I.7 | 1 | 35.8 ± 15.0 | 77.1 ± 9.1 | 57.4 ± 4.3 | 43.1 ± 1.8 |
| I.8 | 1 | 31.1 ± 13.1 | 73.0 ± 9.2 | 54.8 ± 4.3 | 45.1 ± 2.0 |
| I.9 | 1 | 32.3 ± 13.0 | 71.4 ± 10.7 | 54.1 ± 4.1 | 42.9 ± 2.6 |
| I.10 | 1 | 27.1 ± 12.6 | 72.7 ± 10.8 | 54.7 ± 4.2 | 46.0 ± 2.5 |
| I.11 | 1 | 26.9 ± 12.9 | 74.8 ± 10.1 | 55.8 ± 4.5 | 48.63 ± 2.4 |
| I.12 | 1 | 45.1 ± 15.4 | 75.2 ± 9.1 | 56.1 ± 4.0 | 38.7 ± 2.5 |
| I.13 | 1 | 26.5 ± 12.9 | 78.7 ± 8.8 | 58.8 ± 4.4 | 49.9 ± 2.4 |
| I.14 | 1 | 23.6 ± 11.5 | 76.9 ± 9.8 | 58.1 ± 4.4 | 50.8 ± 2.4 |
| I.15 | 1 | 64.7 ± 12.6 | 57.3 ± 11.6 | 40.4 ± 3.7 | 30.8 ± 2.3 |
| I.16 | 1 | 67.9 ± 12.9 | 59.1 ± 10.1 | 41.2 ± 3.6 | 35.5 ± 2.5 |
| | | | | | |
| II.1 | ref.[13] | 24.5 ± 10.9 | 25.8 ± 10.9 | 12.0 ± 3.3 | 47.6 ± 3.0 |
| II.2 | ref.[14] | 39.3 ± 11.7 | 46.8 ± 11.1 | 28.3 ± 4.4 | 53.6 ± 3.1 |
| II.3 | 5 | 20.8 ± 10.3 | 24.9 ± 12.0 | 13.9 ± 3.8 | 46.6 ± 3.0 |
| II.4 | 1 | 36.4 ± 12.1 | 47.7 ± 12.4 | 30.6 ± 4.7 | 54.4 ± 3.1 |
| | | | | | |
| III.1 | ref.[14] | 42.1 ± 15.4 | 70.7 ± 13.6 | 59.7 ± 3.9 | 22.8 ± 2.6 |
| III.2 | 29 | 54.4 ± 16.5 | 67.1 ± 14.9 | 55.1 ± 3.7 | 21.2 ± 2.6 |
| III.3 | 18 | 70.9 ± 13.2 | 62.2 ± 14.5 | 52.5 ± 3.9 | 17.2 ± 2.9 |

| | | | | | |
|---|---|---|---|---|---|
| III.4 | 18 | 68.4 ± 14.0 | 62.2 ± 14.9 | 52.0 ± 3.7 | 17.1 ± 2.9 |
| III.5 | 3 | 62.8 ± 15.2 | 80.9 ± 12.2 | 65.9 ± 3.7 | 34.7 ± 2.6 |
| III.6 | 2 | 66.3 ± 15.0 | 75.0 ± 11.7 | 60.5 ± 3.5 | 26.1 ± 3.0 |
| III.7 | 4 | 54.3 ± 16.0 | 63.7 ± 13.9 | 53.4 ± 3.7 | 20.0 ± 2.7 |
| III.8 | 6 | 76.8 ± 14.2 | 77.4 ± 11.2 | 62.0 ± 3.7 | 32.5 ± 2.3 |
| III.9 | 1 | 65.1 ± 13.3 | 60.3 ± 16.3 | 54.9 ± 3.4 | 20.1 ± 2.7 |
| III.10 | 2 | 70.1 ± 14.8 | 73.6 ± 11.5 | 58.1 ± 3.9 | 22.0 ± 2.7 |
| III.11 | 1 | 67.8 ± 16.2 | 69.5 ± 13.0 | 55.0 ± 4.0 | 25.1 ± 1.9 |
| III.12 | 2 | 50.8 ± 14.6 | 71.2 ± 13.7 | 57.5 ± 3.3 | 21.0 ± 3.0 |
| III.13 | 2 | 73.0 ± 11.7 | 82.6 ± 10.4 | 65.9 ± 3.6 | 31.5 ± 3.1 |
| III.14 | 3 | 57.1 ± 15.3 | 75.4 ± 11.6 | 58.9 ± 3.7 | 23.3 ± 3.0 |
| III.15 | 1 | 51.9 ± 18.5 | 72.9 ± 11.2 | 56.8 ± 3.5 | 22.9 ± 2.6 |
| III.16 | 1 | 49.7 ± 11.9 | 78.2 ± 12.8 | 63.7 ± 3.2 | 30.0 ± 3.5 |
| III.17 | 1 | 60.6 ± 15.9 | 62.0 ± 13.9 | 53.0 ± 3.5 | 19.5 ± 2.5 |
| III.18 | 2 | 58.8 ± 14.4 | 78.5 ± 10.4 | 61.5 ± 3.6 | 26.1 ± 2.7 |
| III.19 | 2 | 77.6 ± 12.2 | 78.8 ± 11.6 | 62.2 ± 3.4 | 31.8 ± 2.5 |
| III.20 | 1 | 66.2 ± 11.8 | 75.0 ± 12.4 | 61.8 ± 3.2 | 34.4 ± 2.6 |
| III.21 | 3 | 50.0 ± 16.3 | 97.3 | 80.0 ± 3.8 | 56.8 ± 2.5 |
| III.22 | 8 | 66.6 ± 9.2 | 70.4 ± 11.2 | 51.3 ± 4.1 | 45.6 ± 3.3 |
| III.23 | 1 | 49.8 ± 11.2 | 83.2 ± 13.2 | 67.1 ± 3.4 | 33.0 ± 3.2 |
| III.24 | 1 | 31.8 ± 14.3 | 86.2 ± 9.9 | 69.3 ± 4.2 | 64.0 ± 2.5 |
| III.25 | 2 | 19.5 ± 9.4 | 71.9 ± 10.5 | 53.2 ± 4.5 | 52.2 ± 2.1 |
| III.26 | 1 | 61.5 ± 14.0 | 52.0 ± 13.8 | 39.3 ± 4.0 | 31.1 ± 2.3 |
| III.27 | 1 | 77.8 ± 12.1 | 55.8 ± 15.3 | 46.3 ± 3.7 | 29.6 ± 2.1 |
| III.28 | 1 | 76.7 ± 10.8 | 77.6 ± 13.0 | 65.8 ± 3.9 | 84.5 ± 11.4 |
| III.29 | 2 | 62.7 ± 11.8 | 66.3 ± 13.8 | 56.7 ± 4.2 | 38.4 ± 2.4 |
| III.30 | 1 | 105.3 ± 14.8 | 57.0 ± 9.7 | 37.3 ± 3.6 | 17.9 ± 3.3 |
| III.31 | 1 | 59.3 ± 13.9 | 55.4 ± 9.9 | 36.3 ± 3.2 | 12.1 ± 2.3 |
| | | | | | |
| IV.1 | 1 | 53.3 ± 9.7 | 69.4 ± 13.5 | 60.0 ± 3.7 | 51.9 ± 3.4 |
| IV.2 | 1 | 53.3 ± 12.9 | 78.1 ± 11.2 | 63.4 ± 3.5 | 39.5 ± 2.7 |
| IV.3 | 1 | 26.8 ± 13.8 | 41.0 ± 16.9 | 40.9 ± 3.5 | 40.4 ± 2.4 |
| | | | | | |
| V.1 | 2 | 55.2 ± 10.9 | 82.8 ± 14.5 | 67.6 ± 3.5 | 34.9 ± 2.9 |
| V.2 | 1 | 25.4 ± 11.7 | 43.4 ± 15.7 | 35.8 ± 3.5 | 40.0 ± 3.3 |
| | | | | | |
| VI.1 | 1 | 32.8 ± 11.6 | 48.2 ± 10.6 | 30.8 ± 4.3 | 43.4 ± 2.6 |
| | | | | | |
| VII.1 | 1 | 81.1 ± 9.2 | 67.9 ± 9.8 | 49.7 ± 4.4 | 38.1 ± 2.3 |
| | | | | | |
| VIII.1 | 2 | 48.9 ± 11.2 | 43.0 ± 14.5 | 35.5 ± 3.3 | 44.9 ± 3.5 |
| | | | | | |
| IX.1 | 1 | 67.5 ± 10.2 | 69.1 ± 10.3 | 51.2 ± 4.2 | 45.5 ± 3.2 |
| IX.2 | 14 | 33.9 ± 12.4 | 88.8 ± 11.2 | 72.1 ± 3.5 | 44.8 ± 2.7 |
| IX.3 | 1 | 59.4 ± 14.1 | 57.2 ± 16.0 | 51.5 ± 3.8 | 25.4 ± 2.1 |

| | | | | | |
|---|---|---|---|---|---|
| IX.4 | 1 | 65.8 ± 10.6 | 89.9 ± 14.3 | 72.2 ± 3.7 | 46.8 ± 2.9 |
| IX.5 | 2 | 77.5 ± 11.7 | 69.7 ± 14.5 | 68.2 ± 3.7 | 84.3 ± 12.4 |
| IX.6 | 1 | 36.3 ± 13.9 | 33.3 ± 14.5 | 29.8 ± 4.2 | 33.8 ± 1.8 |
| IX.7 | 2 | 48.2 ± 13.4 | 29.6 ± 12.3 | 26.7 ± 3.5 | 24.0 ± 2.6 |
| IX.8 | 1 | 73.9 ± 11.9 | 33.7 ± 12.8 | 28.4 ± 3.4 | 25.0 ± 2.5 |
| IX.9 | 1 | 73.8 ± 11.7 | 34.7 ± 12.9 | 29.4 ± 3.4 | 26.2 ± 3.2 |
| IX.10 | 1 | 78.5 ± 11.3 | 44.2 ± 14.2 | 32.4 ± 3.0 | 13.2 ± 2.9 |
| IX.11 | 1 | 77.6 ± 13.4 | 53.6 ± 9.4 | 34.1 ± 3.5 | 10.4 ± 2.7 |
| IX.12 | 2 | 80.8 ± 10.9 | 43.7 ± 15.4 | 34.2 ± 3.5 | 14.5 ± 1.9 |

**Table S4: Comparison of NMR derived distances of a K-Ras4B-GDP dimer from Lee et al[2] with the dimer models shown in Fig. 1.** Lee et al. constructed a K-Ras4B GDP dimer model based on NMR derived distance data (Model I.3 in Fig. 1). We compared all other dimer models shown in Fig. 1, using the same procedure described by Lee et al. Cells marked in green are in accordance with the experimental distances. The distance measurements involving residue 169 were not possible for model II.2, as it is only modelled from residue 1-167.

| Residue | Atom | Residue | Atom | PRE Distance / Å | I.1 | I.2 | I.3 | I.4 | II.1 | II.2 | III.1 |
|---|---|---|---|---|---|---|---|---|---|---|---|
| 118 | SG | 112 | CG1/CG2 | 15.3 ± 3,0 | 19,6 | 23,9 | 18,2 | 17,1 | 32,1 | 30,5 | 38,8 |
| 118 | SG | 113 | CD1/CD2 | 14.9 ± 3,0 | 26,0 | 30,4 | 15,8 | 20,5 | 21,3 | 24,6 | 41,7 |
| 118 | SG | 114 | CG1/CG2 | 17.5 ± 3,0 | 21,3 | 26,1 | 18,7 | 17,1 | 30,6 | 31,2 | 35,8 |
| 118 | SG | 125 | CG1/CG2 | 16.1 ± 3,0 | 31,0 | 34,8 | 16,2 | 22,8 | 20,6 | 23,2 | 42,8 |
| 118 | SG | 133 | CD1/CD2 | 14.6 ± 3,0 | 30,2 | 34,2 | 16,2 | 24,3 | 21,1 | 19,6 | 45,4 |
| 118 | SG | 139 | CD1 | 15.0 ± 3,0 | 28,6 | 31,9 | 18,0 | 23,3 | 30,9 | 28,8 | 48,0 |
| 118 | SG | 142 | CD1 | 14.4 ± 3,0 | 20,2 | 24,7 | 16,8 | 13,8 | 37,3 | 34,7 | 43,6 |
| 118 | SG | 128 | N | 13.1 ± 3,0 | 31,6 | 35,5 | 10,3 | 20,9 | 25,5 | 24,7 | 52,9 |
| 118 | SG | 127 | CG2 | 13.2 ± 3,0 | 28,0 | 34,7 | 10,8 | 17,6 | 29,0 | 28,2 | 50,5 |
| 118 | SG | 142 | CG2 | 14.7 ± 3,0 | 20,4 | 26,0 | 17,3 | 13,1 | 36,8 | 35,8 | 42,4 |
| 169 | CG | 45 | CG1/CG2 | 15.5 ± 3,0 | 27,2 | 23,5 | 12,7 | 29,7 | 45,9 |  | 43,1 |
| 169 | CG | 46 | CD1 | 15.5 ± 3,0 | 24,8 | 21,5 | 13,5 | 27,3 | 44,3 |  | 46,8 |
| 169 | CG | 159 | CD1/CD2 | 16.1 ± 3,0 | 19,0 | 16,2 | 17,0 | 19,8 | 31,0 |  | 40,4 |
| 169 | CG | 160 | CG1/CG2 | 14.5 ± 3,0 | 20,5 | 16,8 | 11,8 | 22,4 | 36,5 |  | 40,9 |
| 169 | CG | 163 | CD1 | 15.5 ± 3,0 | 20,1 | 17,4 | 16,8 | 23,2 | 35,7 |  | 44,2 |
| 169 | CG | 165 | N | 14.8 ± 3,0 | 16,8 | 10,6 | 11,9 | 18,6 | 37,1 |  | 51,4 |
| 169 | CG | 167 | N | 15.3 ± 3,0 | 18,3 | 10,7 | 14,9 | 19,2 | 34,6 |  | 49,6 |
| 169 | CG | 169 | N | 14.8 ± 3,0 | 16,7 | 7,1 | 15,4 | 17,4 | 34,9 |  | 53,6 |
| 169 | CG | 172 | N | 16.1 ± 3,0 | 20,4 | 9,2 | 18,2 | 19,4 | 35,0 |  | 55,0 |

**Table S5: Comparison of NMR derived distances of a K-Ras4B-GTP dimer from Lee et al.[2] with the dimer models shown in Fig. 1.** Lee et al. constructed a K-Ras4B GTP dimer model based on NMR derived distance data (Model I.4 in Fig. 1). We compared all other dimer models shown in Fig. 1, using the same procedure described by Lee et al. Cells marked in green are in accordance with the experimental distances. The distance measurements involving residue 169 were not possible for model II.2, as it is only modeled from residue 1-167.

| Residue | Atom | Residue | Atom | PRE Distance / Å | I.1 | I.2 | I.3 | I.4 | II.1 | II.2 | III.1 |
|---|---|---|---|---|---|---|---|---|---|---|---|
| 118 | SG | 44 | CG1/CG2 | 15,4 ± 3,0 | 12,1 | 16,6 | 29.0 | 18,0 | 44,3 | 43,6 | 30,4 |
| 118 | SG | 45 | CG1/CG2 | 14,4 ± 3,0 | 7,9 | 12,2 | 31.3 | 17,1 | 48,9 | 46,7 | 33,9 |
| 118 | SG | 46 | CD1 | 15,7 ± 3,0 | 13,1 | 18,4 | 29.5 | 18,5 | 47,5 | 45,4 | 38,5 |
| 118 | SG | 142 | CD1 | 13,3 ± 3,0 | 20,2 | 24,7 | 16.8 | 13,9 | 37,3 | 34,7 | 43,6 |
| 118 | SG | 160 | CG1/CG2 | 16,0 ± 3,0 | 14,5 | 18,9 | 25.3 | 18,6 | 40,6 | 38,8 | 35,5 |
| 118 | SG | 127 | CG2 | 15,2 ± 3,0 | 28,0 | 32,4 | 10.8 | 17,6 | 29,0 | 28,2 | 50,5 |
| 118 | SG | 142 | CG2 | 13,8 ± 3,0 | 20,4 | 25,2 | 17.3 | 13,1 | 36,8 | 35,8 | 42,4 |
| 118 | SG | 144 | CG2 | 13,7 ± 3,0 | 21,5 | 27,5 | 20.1 | 15,2 | 36,7 | 37,2 | 39,2 |
| 118 | SG | 148 | CG2 | 14,4 ± 3,0 | 22,7 | 29,6 | 24.7 | 17,1 | 40,9 | 43,2 | 36,6 |
| 169 | CG | 113 | CD1/CD2 | 15,9 ± 3,0 | 16,0 | 17,6 | 24.4 | 15,8 | 28,4 |  | 47,1 |
| 169 | CG | 125 | CG1/CG2 | 16,0 ± 3,0 | 21,3 | 24,4 | 30.9 | 19,9 | 31,0 |  | 50,1 |
| 169 | CG | 133 | CD1/CD2 | 13,5 ± 3,0 | 15,1 | 18,2 | 27.5 | 14,1 | 24,7 |  | 49,1 |
| 169 | CG | 139 | CD1 | 15,2 ± 3,0 | 14,3 | 12,2 | 23.7 | 15,1 | 30,2 |  | 52,2 |
| 169 | CG | 128 | N | 15,9 ± 3,0 | 19,2 | 23,9 | 31.8 | 18,9 | 37,7 |  | 62,2 |
| 169 | CG | 176 | N | 17,1 ± 3,0 | 16,6 | 17,8 | 25.5 | 16,4 | 30,2 |  | 58,6 |
| 169 | CG | 177 | N | 17,5 ± 3,0 | 18,9 | 21,3 | 26.3 | 17,1 | 32,0 |  | 57,0 |
| 169 | CG | 178 | N | 17,2 ± 3,0 | 21,6 | 24,0 | 27.7 | 17,7 | 34,1 |  | 57,6 |
| 169 | CG | 179 | N | 17,2 ± 3,0 | 24,5 | 26,4 | 28..6 | 18,9 | 37,3 |  | 58,1 |

**Table S6: Summary of the MD simulation systems.** Row one gives the dimer conformations according to the numbering in Table S3 that are used to initiate MD simulations to obtain an equilibrated structure. Also given are the numbers of the run with the same conformation but different start velocity distribution (row two), the simulation time in nano seconds (row three), and the composition of the simulation system.

| Conformation | Run | Simulation Time | Total Atoms | Protein Atoms | Membrane Atoms | Water Molecules | $Na^+$ | $Cl^-$ |
|---|---|---|---|---|---|---|---|---|
| I.1 | I | 550 ns | 234868 | 5942 | 26468 | 50502 | 243 | 207 |
| I.5 | I | 550 ns | 234552 | 5942 | 26520 | 50410 | 243 | 207 |
| I.6 | I | 800 ns | 234668 | 5942 | 26468 | 50452 | 243 | 207 |
| I.7 | I | 800 ns | 260244 | 5942 | 26468 | 56846 | 243 | 207 |
| I.8 | I | 550 ns | 234664 | 5942 | 26520 | 50438 | 243 | 207 |
| I.9 | I | 800 ns | 234860 | 5942 | 26468 | 50500 | 243 | 207 |
| I.10 | I | 550 ns | 234664 | 5942 | 26520 | 50438 | 243 | 207 |
| I.11 | I | 550 ns | 232964 | 5942 | 26624 | 49.987 | 243 | 207 |
| I.12 | I | 550 ns | 234916 | 5942 | 26468 | 50514 | 243 | 207 |

**Table S7: Validation of the representative Ras dimer structures from the 9 simulation runs by comparing theoretical distances with experimental values.** Given as reference are the three experimental distances, obtained by FRET experiments for the FRET fluorophore pairs S106-Atto532/S106-Atto655, T124-Atto532/T124-Atto655, GDP-MANT/GDP-TNP and the EPR label pair T124-Proxyl/T124-Proxyl taken from Fig. 3. Summarized are the mean values and their standard deviation of the gauss fit of the calculated distance distribution of the four aforementioned label for all obtained representative structural models from the simulation runs (see Supporting Note 6) using the mtsslWizard[21] as shown in Fig. S3 and described in Supporting Note 5. The agreement with the experiment is color coded in the following manner; green: the calculated mean distance is within the standard deviation of the experimental value; yellow: the calculated standard deviation is within the experimental standard deviation; red: the calculated values are not in accordance with the experiment.

| | **Distance / Å** | | | |
|---|---|---|---|---|
| **Conformation** | **S106-S106** | **T124-T124** | **T124-T124 Proxyl** | **Nucleotide - Nucleotide** |
| Experimental | 43,3 ± 2.3 | 72,0 ± 3.5 | 59.7 ± 2.5 | 46,3 ± 1,4 |
| I.1 | 47.0 ± 11.3 | 81.5 ± 10.7 | 63.8 ± 4.3 | 58.3 ± 2.4 |
| I.5 | 40,1 ± 11,6 | 79,9 ± 10,1 | 63.7 ± 4.5 | 52,5 ± 2,1 |
| I.6 | 42,5 ± 9,9 | 80,5 ± 9,9 | 61.6 ± 4.4 | 56,4 ± 2,4 |
| I.7 | 45,2 ± 14,7 | 82,1 ± 9,3 | 62.7 ± 4.5 | 55,1 ± 2,4 |
| I.8 | 47,4 ± 12,6 | 79,3 ± 9,2 | 60.1 ± 4.2 | 51,0 ± 2,2 |
| I.9 | 41,1 ± 11,5 | 76,5 ± 10,6 | 58.8 ± 4.2 | 43,6 ± 1,9 |
| I.10 | 39,5 ± 9,5 | 78,3 ± 10,1 | 60.3 ± 4.2 | 45,8 ± 1,9 |
| I.11 | 40.4 ± 11.8 | 62.7 ± 11.3 | 46.4 ± 4.0 | 51.2 ± 2.1 |
| I.12 | 45,6 ± 16,2 | 80,7 ± 9,7 | 62.6 ± 4.4 | 37,8 ± 2,0 |

**Table S8: Summary of the N-Ras dimer interface.** Summarized is the contact analysis of nine independent MD simulation runs (see Fig. S5). For every intermolecular contact it is specified in how many simulations it is present, and whether it is a hydrogen bond/salt bridge or van der waals contact. Finally, it is shown in how many simulations the contact is present one sided and in how many it is present two sided. Only contacts that are present in the last third of the simulation are included.

| | | **Number of simulations present at least one sided** | | **Number of simulations present Two sided** | |
|---|---|---|---|---|---|
| **Contact** | | h-bond/salt bridge | Van der waals | h-bond/salt bridge | Van der waals |
| D154 | R161 | 8 | 0 | 3 | 0 |
| E49 | H131 | 2 | 3 | 0 | 0 |
| R161 | E162 | 3 | 0 | 0 | 0 |
| T158 | R161 | 1 | 3 | 0 | 1 |
| S136 | N172 | 2 | 1 | 0 | 0 |
| E162 | Q165 | 2 | 1 | 0 | 0 |
| E132 | R164 | 2 | 0 | 0 | 0 |
| R149 | E153 | 2 | 0 | 0 | 0 |
| E162 | R164 | 2 | 0 | 0 | 0 |
| G138 | K169 | 1 | 4 | 0 | 1 |
| R97 | D175 | 2 | 0 | 0 | 0 |
| H131 | M168 | 0 | 3 | 0 | 0 |
| D154 | Y157 | 0 | 2 | 0 | 1 |
| V45 | Q150 | 1 | 1 | 1 | 0 |
| E49 | K128 | 1 | 1 | 0 | 0 |
| L23 | R149 | 1 | 0 | 0 | 0 |
| D47 | F141 | 1 | 0 | 0 | 0 |
| D47 | D154 | 1 | 0 | 0 | 0 |
| G138 | R164 | 1 | 0 | 0 | 0 |
| G151 | Y157 | 1 | 0 | 0 | 0 |
| H131 | K169 | 1 | 0 | 0 | 0 |
| N172 | N172 | 1 | 0 | 0 | 0 |
| D108 | Q165 | 1 | 0 | 0 | 0 |
| V109 | Q165 | 1 | 0 | 0 | 0 |
| S136 | S173 | 1 | 0 | 0 | 0 |
| G138 | R161 | 1 | 0 | 0 | 0 |
| E132 | R167 | 1 | 0 | 0 | 0 |
| K169 | T178 | 1 | 0 | 0 | 0 |
| N172 | E180 | 1 | 0 | 0 | 0 |
| K135 | Q165 | 0 | 3 | 0 | 0 |
| K135 | L171 | 0 | 3 | 0 | 0 |
| S136 | L171 | 0 | 3 | 0 | 0 |

| | | | | | |
|---|---|---|---|---|---|
| P140 | Q165 | 0 | 2 | 0 | 0 |
| Q165 | Q165 | 0 | 2 | 0 | 0 |
| P140 | R161 | 0 | 1 | 0 | 0 |
| I139 | M168 | 0 | 1 | 0 | 0 |
| Y137 | L171 | 0 | 1 | 0 | 0 |
| G138 | L171 | 0 | 1 | 0 | 0 |
| Y137 | N172 | 0 | 1 | 0 | 0 |
| K135 | R164 | 0 | 1 | 0 | 0 |
| D108 | D175 | 0 | 1 | 0 | 0 |
| D108 | D178 | 0 | 1 | 0 | 0 |
| Y166 | M182 | 0 | 1 | 0 | 0 |
| K135 | R167 | 0 | 1 | 0 | 0 |
| K135 | M168 | 0 | 1 | 0 | 0 |
| K169 | M182 | 0 | 1 | 0 | 0 |
| K170 | M182 | 0 | 1 | 0 | 0 |

**Table S9: Final concentrations for the CuAAC.** The table shows the final concentrations for the click-chemistry in order to attach the fluorophores to the protein.

| Nr. | Substance | Concentration (µM) |
|---|---|---|
| 1 | $CuSO_4$ | 100 |
| 2 | THPTA | 50 |
| 3 | Sodium ascorbate | 2500 |
| 4 | N-Ras S106-PrK / T124-PrK C118S | 24 |
| 5 | Atto532-azid / Atto655-azid | 100 |
| 6 | Benzoic acid | 20 |

**Table S10: Labelling efficiencies.** The table shows the final labelling efficiencies of the click-chemistry with the fluorophores Atto532azide and Atto655azide.

| Protein | Label |
|---|---|
| N-Ras S106-PrK | 40 % Atto532azide |
| | 40 % Atto655azide |
| N-Ras T124-PrK C118S | 56 % Atto532azide |
| | 41 % Atto655azide |
| Lipidated N-Ras S106-PrK | 40 % Atto532azide |
| | 57 % Atto655azide |
| Lipidated N-Ras T124-PrK C118S | 47 % Atto532azide |
| | 41 % Atto655azide |
| Lipidated N-Ras E49Q S106-PrK C118S D154N | 37 % Atto532azide |
| | 59 % Atto655azide |

**Table S11: PDB structures used as a starting point for the construction of dimer models.**

| PDB-ID | Isoform | Nucleotide/Analogon | Residues | Missing Residues | Residues with Missing Atoms |
|---|---|---|---|---|---|
| 1ctq [1] | H-Ras | GppNHp | 1-166 | 167-172 | -- |
| 1q21 [2] | H-Ras | GDP | 1-171 | 172 | -- |
| 4q21 [3] | H-Ras | GDP | 1-168 | 169-172 | -- |
| 5ocg [4] | K-Ras4B | GppNHp | 1-172 | -- | E31, R41 |
| 4l8g [5] | K-Ras4B | GDP | 1-59, 70-167 | 60-69, 168-172 | Q70, Y71, K128 |
| 5uhv [6] | N-Ras | GppNHp | 1-166 | 167-172 | E31, Q61, E62, E63, S65, Q70, Y71, R73, Q99, D126, K128, K135 |
| 3con [7] | N-Ras | GDP | 1-60, 72-167 | 61-71, 168-172 | E3, K5, R41, R73, D108, K128, E143, Q165 |

**Table S12: Composition of the detected TCSPC fluorescence signal**. The table displays the fraction of the detected total fluorescence signal that can undergo FRET.

| Dimer | Probability | Fluorescence | „Fluorescence amount“ | FRET | „FRET amount“ |
|---|---|---|---|---|---|
| DD | 0.014 | 2 | 0.028 | 0 | 0 |
| DA | 0.048 | 1 | 0.048 | 1 | 0.048 |
| AD | 0.048 | 1 | 0.048 | 1 | 0.048 |
| AA | 0.159 | 0 | 0 | 0 | 0 |
| XX | 0.231 | 0 | 0 | 0 | 0 |
| XD | 0.057 | 1 | 0.057 | 0 | 0 |
| DX | 0.057 | 1 | 0.057 | 0 | 0 |
| XA | 0.192 | 0 | 0 | 0 | 0 |
| AX | 0.192 | 0 | 0 | 0 | 0 |
| **Sum** | **1** | | **0.238** | | **0.096** |

## Literature Cited


1. Güldenhaupt J, Rudack T, Bachler P, Mann D, Triola G, Waldmann H et al. N-Ras forms dimers at POPC membranes. Biophys J 2012; 103(7):1585–93.

2. Lee K-Y, Fang Z, Enomoto M, Gasmi-Seabrook G, Le Zheng, Koide S et al. Two Distinct Structures of Membrane-Associated Homodimers of GTP- and GDP-Bound KRAS4B Revealed by Paramagnetic Relaxation Enhancement. Angewandte Chemie (International ed. in English) 2020; 59(27):11037–45.

3. Muratcioglu S, Chavan TS, Freed BC, Jang H, Khavrutskii L, Freed RN et al. GTP-Dependent K-Ras Dimerization. Structure (London, England : 1993) 2015; 23(7):1325–35.

4. Prakash P, Sayyed-Ahmad A, Cho K-J, Dolino DM, Chen W, Li H et al. Computational and biochemical characterization of two partially overlapping interfaces and multiple weak-affinity K-Ras dimers. Sci Rep 2017; 7(1):40109. Available from: URL: https://www.nature.com/articles/srep40109.

5. Lyskov S, Gray JJ. The RosettaDock server for local protein-protein docking. Nucleic acids research 2008; 36(Web Server issue):W233-8.

6. Baspinar A, Cukuroglu E, Nussinov R, Keskin O, Gursoy A. PRISM: a web server and repository for prediction of protein-protein interactions and modeling their 3D complexes. Nucleic acids research 2014; 42(Web Server issue):W285-9.

7. Eswar N, Webb B, Marti-Renom MA, Madhusudhan MS, Eramian D, Shen M-Y et al. Comparative protein structure modeling using Modeller. Curr Protoc Bioinformatics 2006; Chapter 5:Unit-5.6.

8. Güldenhaupt J, Adigüzel Y, Kuhlmann J, Waldmann H, Kötting C, Gerwert K. Secondary structure of lipidated Ras bound to a lipid bilayer. The FEBS journal 2008; 275(23):5910–8.

9. Thapar R, Williams JG, Campbell SL. NMR characterization of full-length farnesylated and non-farnesylated H-Ras and its implications for Raf activation. Journal of molecular biology 2004; 343(5):1391–408.

10. Reuther G, Tan K-T, Köhler J, Nowak C, Pampel A, Arnold K et al. Structural model of the membrane-bound C terminus of lipid-modified human N-ras protein. Angewandte Chemie (International ed. in English) 2006; 45(32):5387–90.

11. Tuncbag N, Gursoy A, Nussinov R, Keskin O. Predicting protein-protein interactions on a proteome scale by matching evolutionary and structural similarities at interfaces using PRISM. Nature protocols 2011; 6(9):1341–54.

12. Pierce BG, Wiehe K, Hwang H, Kim B-H, Vreven T, Weng Z. ZDOCK server: interactive docking prediction of protein-protein complexes and symmetric multimers. Bioinformatics (Oxford, England) 2014; 30(12):1771–3.

13. Schneidman-Duhovny D, Inbar Y, Nussinov R, Wolfson HJ. Geometry-based flexible and symmetric protein docking. Proteins 2005; 60(2):224–31.

14. Schneidman-Duhovny D, Inbar Y, Nussinov R, Wolfson HJ. PatchDock and SymmDock: servers for rigid and symmetric docking. Nucleic acids research 2005; 33(Web Server issue):W363-7.

15. Bader B, Kuhn K, Owen DJ, Waldmann H, Wittinghofer A, Kuhlmann J. Bioorganic synthesis of lipid-modified proteins for the study of signal transduction. Nature 2000; 403(6766):223–6. Available from: URL: https://pubmed.ncbi.nlm.nih.gov/10646611/.

16. Plass T, Milles S, Koehler C, Schultz C, Lemke EA. Genetically encoded copper-free click chemistry. Angewandte Chemie (International ed. in English) 2011; 50(17):3878–81.

17. Nguyen DP, Lusic H, Neumann H, Kapadnis PB, Deiters A, Chin JW. Genetic encoding and labeling of aliphatic azides and alkynes in recombinant proteins via a pyrrolysyl-tRNA Synthetase/tRNA(CUA) pair and click chemistry. Journal of the American Chemical Society 2009; 131(25):8720–1. Available from: URL: https://pubmed.ncbi.nlm.nih.gov/19514718/.

18. Brunsveld L, Kuhlmann J, Alexandrov K, Wittinghofer A, Goody RS, Waldmann H. Lipidated ras and rab peptides and proteins--synthesis, structure, and function. Angewandte Chemie (International ed. in English) 2006; 45(40):6622–46.

19. Rostovtsev VV, Green LG, Fokin VV, Sharpless KB. A Stepwise Huisgen Cycloaddition Process: Copper(I)-Catalyzed Regioselective "Ligation" of Azides and Terminal Alkynes. Angew. Chem. Int. Ed. 2002; 41(14):2596–9.

20. Shao C, Wang X, Xu J, Zhao J, Zhang Q, Hu Y. Carboxylic acid-promoted copper(I)-catalyzed azide-alkyne cycloaddition. The Journal of organic chemistry 2010; 75(20):7002–5.

21. Hagelueken G, Ward R, Naismith JH, Schiemann O. MtsslWizard: In Silico Spin-Labeling and Generation of Distance Distributions in PyMOL. Applied magnetic resonance 2012; 42(3):377–91.

22. Abraham MJ, Murtola T, Schulz R, Páll S, Smith JC, Hess B et al. GROMACS: High performance molecular simulations through multi-level parallelism from laptops to supercomputers. SoftwareX 2015; 1-2:19–25. Available from: URL: http://www.sciencedirect.com/science/article/pii/S2352711015000059.

23. Rudack T, Xia F, Schlitter J, Kötting C, Gerwert K. The role of magnesium for geometry and charge in GTP hydrolysis, revealed by quantum mechanics/molecular mechanics simulations. Biophys J 2012; 103(2):293–302.

24. Ulmschneider JP, Ulmschneider MB. United Atom Lipid Parameters for Combination with the Optimized Potentials for Liquid Simulations All-Atom Force Field. Journal of chemical theory and computation 2009; 5(7):1803–13.

25. Jeschke G, Polyhach Y. Distance measurements on spin-labelled biomacromolecules by pulsed electron paramagnetic resonance. Physical chemistry chemical physics : PCCP 2007; 9(16):1895–910. Available from: URL: https://pubmed.ncbi.nlm.nih.gov/17431518/.

26. Pannier M, Veit S, Godt A, Jeschke G, Spiess HW. Dead-time free measurement of dipole-dipole interactions between electron spins. Journal of magnetic resonance (San Diego, Calif. : 1997) 2000; 142(2):331–40.

27. Jeschke G, Chechik V, Ionita P, Godt A, Zimmermann H, Banham J et al. DeerAnalysis2006—a comprehensive software package for analyzing pulsed ELDOR data. Appl. Magn. Reson. 2006; 30(3-4):473–98.

28. Krieger E, Koraimann G, Vriend G. Increasing the precision of comparative models with YASARA NOVA--a self-parameterizing force field. Proteins 2002; 47(3):393–402. Available from: URL: https://pubmed.ncbi.nlm.nih.gov/11948792/.